UNCERTAINTY ANALYSIS OF A PARTICLE TRACKING ALGORITHM
DEVELOPED FOR SUPER-RESOLUTION PARTICLE IMAGE VELOCIMETRY

A Thesis
Submitted to the College of Graduate Studies and Research
in Partial Fulfillment of the Requirements for the Degree of
Master of Science
in the
Department of Mechanical Engineering
University of Saskatchewan
Saskatoon

by

Sujith Joseph

August 2003

Permission to Use

In presenting this thesis in partial fulfillment of the requirements for a postgraduate degree from the University of Saskatchewan, I agree that the libraries of this University may make it freely available for inspection. I further agree that permission for copying of this thesis in any manner, in whole or in part, for scholarly purposes may be granted by the professor who supervised my thesis work or, in their absence, by the Head of the Department or the Dean of the College in which my thesis work was done. It is understood that any copy or publication or use of this thesis or parts thereof for financial gain shall not be allowed without my written permission. It is also understood that due recognition shall be given to me and to the University of Saskatchewan in any use which may be made of any material in my thesis.

Requests for permission to copy or to make other use of material in this thesis in whole or part should be addressed to:

Head of the Department of Mechanical Engineering
University of Saskatchewan
Saskatoon, Saskatchewan S7N 5A9

i

Abstract

   Particle Image Velocimetry (PIV) is a powerful technique to measure the velocity at many points in a flow simultaneously by performing correlation analysis on images of particles being transported by the flow. These images are acquired by illuminating the flow with two light pulses so that each particle appears once on each image. The spatial resolution is an important parameter of this measuring system since it determines its ability to resolve features of interest in the flow. The super-resolution technique maximises the spatial resolution by augmenting the PIV analysis with a second pass that identifies specific particles and measures the distance between them.

   The accuracy of the procedure depends on both the success with which the proper pairings are identified and the accuracy with which their centre-to-centre distance can be measured. This study presents an analysis of both the systematic uncertainty and random uncertainty associated with this process. The uncertainty is analysed as a function of several key parameters that define the quality of the image. The uncertainty analysis is performed by preparing 4000 member ensembles of simulated images with specific setpoints of each parameter.

   It is shown that the systematic uncertainty is negligible compared to the random uncertainty for all conditions tested. Also, the image contrast and the selection of a threshold for the particle search are the most critical parameters influencing both success rate and uncertainty. It is also shown that high image intensities still yield accurate results. The search radius used by the super-resolution algorithm is shown to be a critical parameter also. By increasing the search radius, the success rate can be increased although this is accompanied by an increase in random uncertainty.

Acknowledgments

Dedication

Dedicated to God, my parents and sister, teachers, and all who have helped.

Lord
guard me from all false knowledge
that exalts itself against you.

Contents

List of Tables

List of Figures

xi

Nomenclature

Roman

a x coordinate of the left edge of the rectangle **R**, page 64

$A(\mathbf{R})$ Area of rectangle **R**, page 64

b x coordinate of the right edge of the rectangle **R**, page 64

b Velocity gradient in y direction, page 55

c y coordinate of the lower edge of the rectangle **R**, page 64

C Confidence level, page 34

d y coordinate of the upper edge of the rectangle **R**, page 64

$\partial u/\partial y$ Gradient of the u velocity in the y direction, page 82

d Velocity gradient in x direction, page 55

d_k Distance from regular grid node to data point, page 53

D_p The diameter of the particle , page 59

$F(x, y)$ Gaussian weighting function, page 53

$f(t, \nu)$ The t probability distribution, page 127

f_k Irregular velocity data point, page 53

$I(r)$ Intensity at radial distance r from particle centre, page 59

I_0 Intensity at the centre of the particle, page 61

$\Gamma(x)$ The Gamma function of x, page 127

μ_D The mean diameter of the particles, page 59

μ_{I_0} The mean central intensity of the particles, page 82

μ_{I_b} The mean intensity of the background, page 82

μ_x Mean of n measurements of X, page 31

ν Number of degrees of freedom of a t distribution, page 127

ψ The stream function, page 134

σ_D Standard deviation of particle diameters, page 59

θ Direction of velocity vector, page 82

θ_m Direction of the measured test particle velocity, page 77

θ_t Direction of the exact test particle velocity, page 74

Abbreviations

AIAA American Institute of Aeronautics and Astronautics, page 36

ANSI American National Standards Institute, page 36

ASME American Society of Mechanical Engineers, page 36

CCD Charge coupled device, page 1

DOE Design of Experiments, page 105

GTTC Ground Testing Technical Committee, page 36

GUM Guide to the expression of uncertainty in measurement, page 37

ISO International Standards Organisation, page 37

PIN Particle identification number, page 44

PIV Particle image velocimetry, page 1

PTA Particle tracking algorithm, page 2

Chapter 1

Introduction

1.1 General

Particle image velocimetry (PIV) is a non-intrusive optical technique for measuring the velocity field in a fluid flow [1], [2]. PIV yields a large number of measurements of velocity on a plane in the flow. In dual-frame, cross-correlation PIV, a seeded flow is illuminated twice with laser light sheets and the images are captured on separate frames by a charge coupled device (CCD) camera. The images are divided into interrogation areas of equal size. Digital image cross-correlation of corresponding interrogation areas on the images is used to obtain the mean velocity of all particles within the interrogation area. The *spatial resolution* of a PIV technique can be defined as the number of velocity vectors that it yields for an interrogation area. Cross-correlation particle image velocimetry yields one velocity vector per interrogation area. It has a spatial resolution of one.

Any PIV technique which increases the spatial resolution above one can be termed *super-resolution particle image velocimetry* (SPIV). One way of implementing SPIV

is as a two stage algorithm. In the first stage, cross-correlation PIV is used to find the mean velocity vector for each interrogation area. In the second stage, a particle tracking algorithm (PTA) uses the mean velocity vector as an initial guess to track individual particles in the interrogation area and measure their velocities.

1.2   Objective

Physical quantities cannot be measured with absolute certainty. Repeated measurements of a variable tend to give values which differ among themselves and from the true value. *Measurement error* is the difference between the measured value and the true value. As the true value is rarely known the measurement error must be estimated. *Measurement uncertainty* is the estimate of error. It is an assessment of the degree to which a measurement is representative of the true value.

The objective of this work is to determine the measurement uncertainty of a particle tracking algorithm developed for super-resolution particle image velocimetry. The measurement uncertainty of the particle tracking algorithm is an assessment of how representative its velocity measurement is of the true velocity. Determining the measurement uncertainty involves the following steps. An ensemble of artificial dual-frame PIV images is generated for a known flow field. Each pair contains a test particle whose location is known *a priori*. The tracking algorithm is used to measure the velocity of the test particle on each pair. The difference between the known velocity of the test particle and its velocity computed by the particle tracking algorithm is calculated. This is the measurement error. Statistical analysis of the

sample of measurement errors obtained from the ensemble of dual-frame PIV images gives the measurement uncertainty.

1.3 Scope

As briefly introduced above, super-resolution PIV is a two-step process that first performs a conventional, correlation-based analysis on corresponding interrogation areas of PIV image pairs and then uses a particle tracking algorithm (PTA) to identify specific particles. This thesis is only concerned with the measurement uncertainty of the particle tracking stage of the super-resolution particle image velocimetry algorithm. Therefore PIV information which is free of uncertainty is used in this thesis. The uncertainty analysis of the particle tracking algorithm to be described later in the thesis requires that simulated images be generated. The velocity field used to generate these simulated images is a simple shear flow. A wide variety of velocity fields are possible, but a simple shear flow allows the influence of velocity magnitude, direction, and velocity gradient to be investigated.

1.4 Organisation of the Thesis

In Chapter 2 background information relevant to the thesis is presented. This includes a description of conventional, correlation-based PIV, a discussion of particle tracking and the super-resolution approach, and a presentation of uncertainty analysis concepts. In Chapter 3 the techniques used to perform the uncertainty analysis are

presented. This includes a description of the algorithm used to generate simulated images, a description of the particle tracking algorithm studied in this thesis, and an explanation of uncertainty analysis. The results of the uncertainty analysis are presented in Chapter 4. The conclusions and recommendations from the study are presented in Chapter 5.

Chapter 2

Background

2.1 Particle Image Velocimetry

Figure 2.1 is a schematic diagram of a PIV system. Light from a pulsed Nd-YAG laser is formed into a thin sheet to illuminate a flow seeded with tracer particles. The laser is pulsed twice. The separation time between the two pulses is known accurately. In dual-frame cross-correlation PIV, a CCD camera captures the images of the illuminated particles from the two pulses on separate frames. The displacement of particles in the time between illuminations is determined by appropriate analysis of these two images. The x and y velocity components are obtained by dividing the corresponding displacements by the separation time.
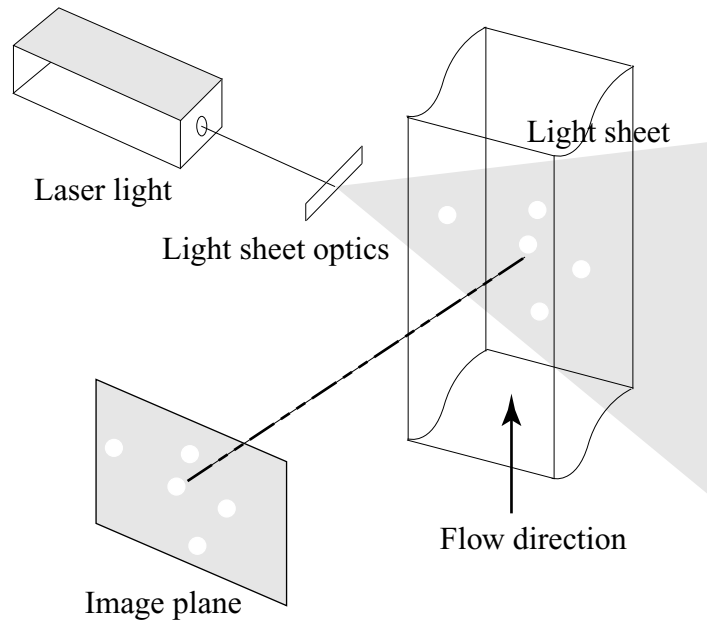
Figure 2.1: *Schematic diagram of a system for particle image velocimetry.*

2.2   PIV System

Laser Light Source

The light source for PIV is usually a Q-switched, pulsed Nd-YAG laser. It produces an intense beam of light having an approximately Gaussian intensity distribution and a duration as short as 8ns when operated in TEM_{00} mode.

Transverse electro-magnetic (TEM) modes describe electric field variation within a cross-section of a laser beam. Transverse modes are labelled TEM_{mn} where m, n are integers. Figure 2.2 shows beam cross sections for several transverse modes. The TEM_{mn} mode has m nodes or zeroes in the x direction and n nodes in the y direction. The intensity profile of the TEM_{00} mode is in the top, left corner. For a
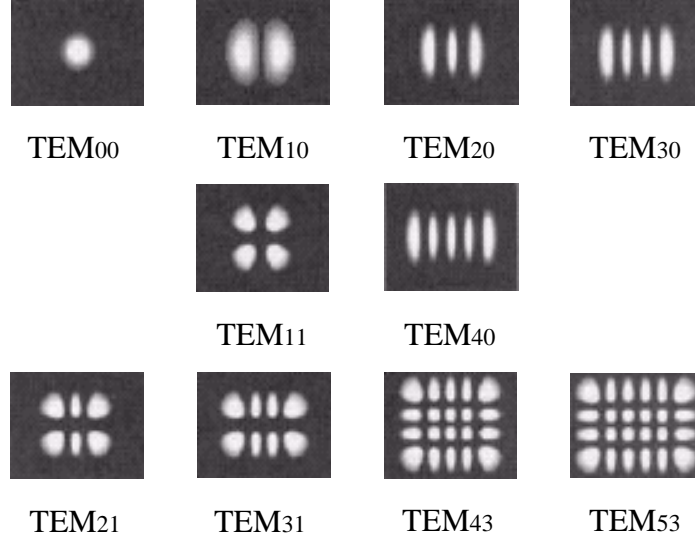
Figure 2.2: *Beam profiles for different laser modes. Adapted from Fox [3]. The Gaussian intensity distribution of the* TEM_{00} *mode is the one in the top, left corner.*

field propogating in the z direction, the x, y dependence of the field is

$$E_{mn}(x, y) = E_0 H_m\left(\frac{\sqrt{2}x}{w}\right) H_n\left(\frac{\sqrt{2}y}{w}\right) \exp\left(-\frac{x^2 + y^2}{w^2}\right). \tag{2.1}$$

H_m and H_n are mathematical functions called Hermite polynomials [4]. The TEM_{00} mode has a Gaussian radial distribution:

$$E_{00}(x, y) = E_0 \exp\left(-\frac{x^2 + y^2}{w^2}\right), \tag{2.2}$$

where r is the radial distance from the center of the beam and the parameter w determines the size of the beam. The TEM_{00} has the least divergence and can be focussed to the smallest size of all modes.

Light Sheet Optics

The laser beam is formed into a light sheet by an optical arrangement consisting of a cylindrical plano-concave lens and a spherical double-convex lens. The optical arrangement is illustrated in Figure 2.3. A cylindrical lens magnifies only in one plane. Figure 2.4 illustrates the refraction of a light beam through a cylindrical lens. The role of the spherical lens is to control the thickness of the light sheet. Typically, the spherical lens has quite a long focal length (250–1000 mm). As the beam passes through the spherical lens it converges to a finite thickness waist at a distance away from the lens equal to its focal length. This is typically the region where PIV measurements are made. The cylindrical lens typically has a much shorter focal length (12-50 mm) and causes relatively rapid beam expansion in one direction.

Seeding Particles

A body immersed in a fluid is called positively buoyant, neutrally buoyant, or negatively buoyant depending on whether the weight of the fluid displaced is greater than, equal to, or less than the weight of the body. Positively bouyant particles float in a flow, negatively bouyant particles settle to the bottom, and neutrally bouyant particles follow the flow. For a body to be neutrally buoyant its density should be equal to the density of the fluid it is immersed in. Since seeding particles should follow the flow faithfully, neutrally buoyant, spherical seeding particles are used in PIV work. In practice the density of a seeding particle can differ from the density of the fluid. The acceleration due to gravity then introduces a velocity which is proportional to

(a)

Beam

waist

Light sheet

S.L   C.L.

(b)

Beam

Light sheet

S.L   C.L
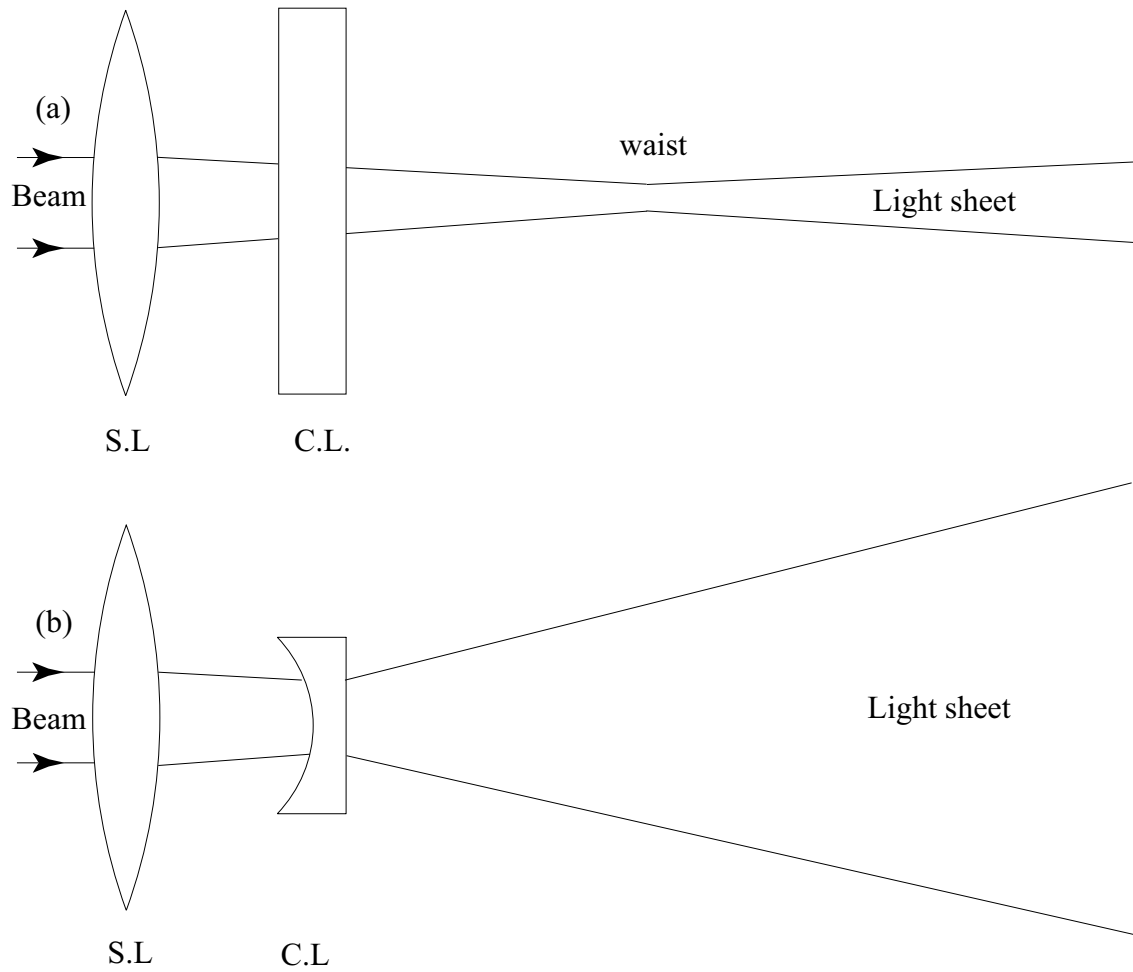
S.L. - Spherical lens

C.L. - Cylindrical lens

Figure 2.3: *The optical arrangement for producing a laser light sheet for particle image velocimetry. (a) Top-view. (b) Front-view.*
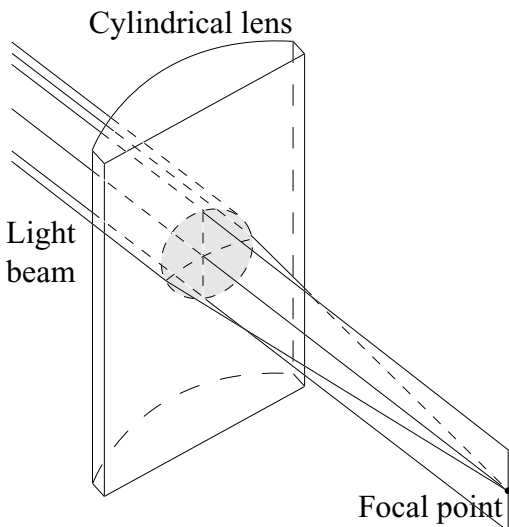
Figure 2.4: *The refraction of a light beam through a cylindrical lens.*

the square of the particle diameter D_p. Inertia forces in accelerating flows cause the particle velocity to lag behind the fluid velocity with a velocity difference proportional to the square of the particle diameter [5], [6]. Since the velocity differences are directly proportinal to the square of the particle diameters, particles which have smaller diameters follow the flow more accurately.

The scattering of light without change in the wavelength of the incident light is called elastic scattering. Elastic scattering of light from spherical particles which have diameters matching the wavelength of the incident light is described by the generalised Lorenz-Mie theory [7], and is called Mie scattering. In Mie scattering, the average intensity of the scattered light is directly proportional to the square of the particle diameters. Large particles scatter more light and are more visible on a PIV photograph. As the diameter of a particle increases its scattering efficiency increases while its velocity fidelity decreases. Seeding particle diameters are choosen to strike

a balance between the contradicting requirements for high scattering efficiency and high velocity fidelity. Seeding particles used in PIV have diameters in the range $1 - 10\mu$m [6],[8]. Aerosols, suspensions of liquid or solid particles in air, are often used for seeding gas flows. Examples of seeding particles used for PIV in liquid flows are hollow glass spheres and polysterene spheres. Examples of seeding particles for gas flows are aerosols of olive oil or corn oil. Melling [6], Stanislas and Monier [9], and Meyers [10] discuss seeding particles for PIV in detail.

Image Recording Device

In dual-frame cross-correlation PIV, the images from the two laser pulses are recorded on separate frames using a CCD camera. A CCD camera sensor consists of a very large number of light sensitive cells or pixels, each capable of producing an electric charge proportional to the amount of light falling on it. The pixels are arranged in a two-dimensional array called an *area array* and facilitate the capture of single image with a single exposure. The *resolution* of a CCD camera is the total number of pixels which make up the light sensitive area of the camera sensor. CCD cameras having a resolution of 4.2 million pixels (TSI PowerView Model 630049/630050) are now available for PIV applications.

2.3   PIV Image Analysis

Digital Image

An analog image is a continous function $I(x, y)$ of two spatial coordinates (x, y). A discrete image is obtained from an analog image by spatial sampling. Consider the image in Figure 2.5. The image is sampled by dividing it into an $M \times N$ matrix of picture elements or *pixels*. The intensity

$$I(m, n) \quad m = 0, 1, \ldots, M - 1, \quad n = 0, 1, \ldots, N - 1$$

assigned to the pixel at location (m, n) is the average value of the function $I(x, y)$ over the area of the pixel. The set of possible values of $I(m, n)$ is continuous. If $I(m, n)$ is restricted to a finite set of values, the discrete signal is said to be amplitude quantised. Amplitude quantisation is usually done by rounding $I(m, n)$ to the nearest integer. A discrete, amplitude-quantised image is called a *digital image*. A greyscale digital image is a matrix of pixels, each having a specific intensity. The number of distinct intensity levels is 2^B where B is the number of bits in the binary representation of the intensity level. There are 256 intensity levels for 8-bit greyscale images. Intensity level 255 represents white and zero represents black.
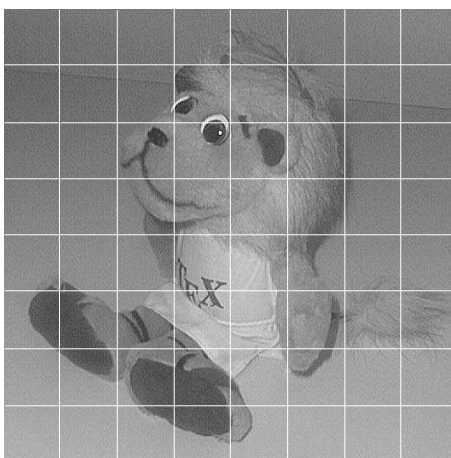
Figure 2.5: *An illustration of a sampling grid superimposed on an analog image. An analog image is converted to a digital image by spatial sampling and amplitude quantisation.*

Convolution and Correlation

The *convolution* $G(m, n)$ of the image $I(m, n)$ with the image $J(m, n)$ is defined as

$$G(m, n) = I(m, n) * J(m, n) = \sum_{k=0}^{M-1} \sum_{l=0}^{N-1} I(m, n) J(k - m, l - n)$$

$$\text{for} \quad k, l = 0, \pm 1, \pm 2, \ldots \quad (2.3)$$

The image $J(k - m, l - n)$ is called the *spatial convolution mask*, the *convolution filter*, or the *convolution kernel*. The pixel values of $J(m, n)$ are called the *kernel values*. The asterisk $(*)$ is used to denote the convolution operation.

The *cross-correlation* $C(m, n)$ between the images $I(m, n)$ and $J(m, n)$ is defined as

$$C(m,n) = I(m,n) \star J(m,n) = \sum_{k=0}^{M-1}\sum_{l=0}^{N-1} I(m,n)J(m-k, n-l)$$

$$\text{for} \quad k, l = 0, \pm 1, \pm 2, \dots \quad (2.4)$$

The pentagram or the five-pointed star $(\star)$ is used to denote the cross-correlation operation. Equation 2.4 can be written as

$$C(m,n) = I(m,n) \star J(m,n) = \sum_{k=0}^{M-1}\sum_{l=0}^{N-1} I(m,n)J\left(-(k-m), -(l-n)\right). \quad (2.5)$$

PIV image analysis involves finding the mean displacement of the particle images that are in the interrogation area. This is an image registration problem. *Image registration* is the procedure of aligning multiple images of the same scene. The image to which the other images are compared is called the base image. The images which are to be aligned to the base image are called input images or templates. The aim of image registration is to find the position which best aligns an input image to a base image. A survey of image registration techniques is given in Brown [11].

The sum of squared differences (SSD) and cross correlation are widely used, and related, techniques for image registration. The sum of squared deviation is a measure of the dissimilarity between two images. It measures the square of the Euclidean distance between the intensities of aligned pixels at each value of the shift between the two images [12]. Let $I(m, n)$ and $J(m, n)$ be $M \times N$ images. The sum of squared

14

difference between the images $I(m,n)$ and $J(m,n)$ is defined as

$$SSD(k,l) = \sum_{m=0}^{M-1}\sum_{n=0}^{N-1}\left(I\left(m,n\right) - J\left(m-k,n-l\right)\right)^2 \quad \text{for} \quad k,l = 0,\pm1,\pm2,\ldots \quad (2.6)$$

The right-hand side of Equation 2.6 can be written as follows.

$$\sum_{m=0}^{M-1}\sum_{n=0}^{N-1}\left(I\left(m,n\right) - J\left(m-k,n-l\right)\right)^2$$

$$= \sum_{m=0}^{M-1}\sum_{n=0}^{N-1} I(m,n)^2 - 2I(m,n)J(m-k,n-l) - J(m-k,n-l)^2$$

$$= \sum_{m=0}^{M-1}\sum_{n=0}^{N-1} I(m,n)^2 - 2\sum_{m=0}^{M-1}\sum_{n=0}^{N-1} I(m,n)J(m-k,n-l) - \sum_{m=0}^{M-1}\sum_{n=0}^{N-1} J(m-k,n-l)^2.$$

$$(2.7)$$

The sum of squared difference has a minimum value when the images $I(m,n)$ and $J(m,n)$ are aligned. This occurs when the second term in the expansion has its maximum value, that is, when

$$\sum_{m=0}^{M-1}\sum_{n=0}^{N-1} I(m,n)J(m-k,n-l) \qquad (2.8)$$

has a maximum value. Equation 2.8 is the cross correlation $C(m,n)$ between the images $I\left(m,n\right)$ and $J\left(m,n\right)$ (see Equation 2.4). The cross correlation varies when there are changes in illumination across the input images. Consider the case where two input images having the same image pattern are being compared to a base image. If one of the images has a higher illumination intensity, it will produce a higher value

of cross-correlation at any value of the shift between the base image and the input images. To avoid this problem, the normalised cross correlation — or the cross-correlation coefficient — is often used as the similarity metric. It is defined as

$$C_N\left(m,n\right)=\frac{\sum\limits_{m=0}^{M-1}\sum\limits_{n=0}^{N-1}\left(I(m,n)-\mu_{I(m,n)}\right)\left(J\left(n-k,n-l\right)-\mu_{J(m,n)}\right)}{\sigma_{I(m,n)}\sigma_{J(m,n)}}$$

$$\text{for} \quad l,k=\pm1,\pm2,\ldots \quad (2.9)$$

The correlation coefficient measures the cross-correlation between images on an absolute scale which has a range $[-1,1]$. Instead of the pattern of intensity values, it is the pattern of deviations from the mean, in multiples of the standard deviation which are now being cross-correlated. A correlation coefficient of 1 indicates maximum alignment and -1 indicates minimum alignment [12].

Figure 2.6 is a schematic illustration of a pair of dual-frame cross-correlation PIV photographs dilineated into *interrogation areas* for cross-correlation analysis. The particles within each interrogation area form a pattern. Since the time interval between the laser pulses is very short, particles in an interrogation area are assumed to maintain their relative alignment from the first to the second photograph. Under this assumption the extraction of the mean velocity of the particles within an interrogation is an image registration problem. The registration of the interrogation areas is done by finding the cross-correlation between them. The shift in pixels required to align an interrogation area on the second photograph with the corresponding interrogation area on the first photograph is the displacement of the particle images in
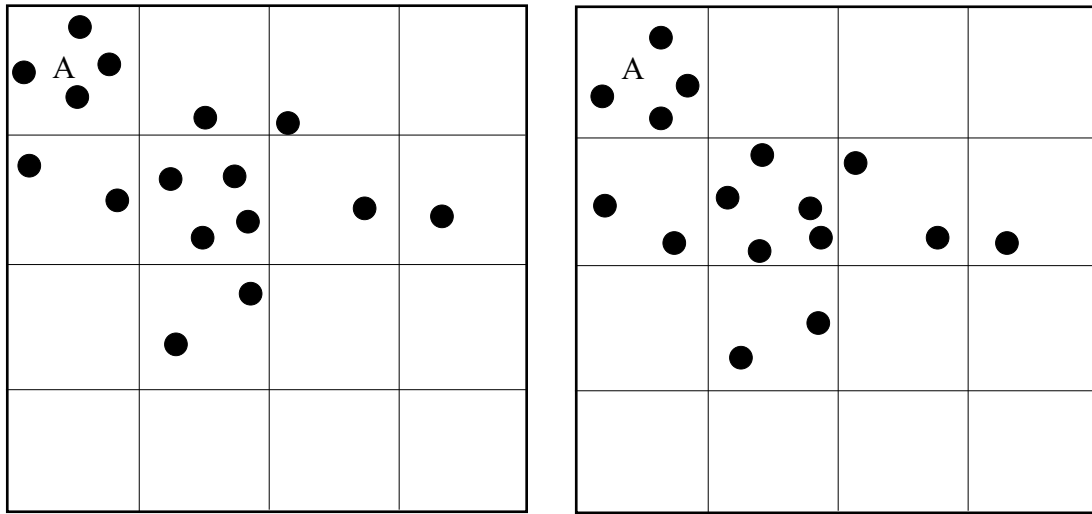
Figure 2.6: *(a) First PIV image. (b) Second PIV image. The two PIV images are delineated into interrogation areas of equal size (the grid in the figure). Cross-correlation between corresponding interrogation areas of the images is employed to determine the mean velocity of the particles within that interrogation area.*
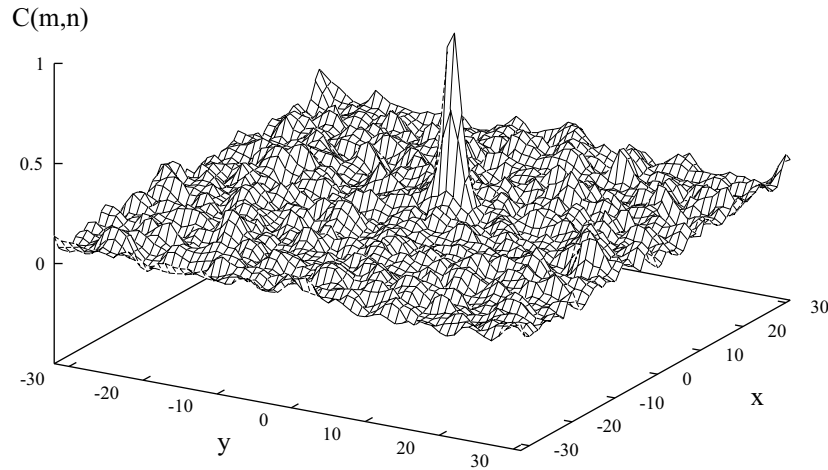
Figure 2.7: *The cross-correlation function between two interrogation areas. The displacement of the peak in the discrete cross-correlation function C(m,n) from the origin of the cross -correlation plane is the mean displacement of the particles in the interrogatin area.*

the time between the laser pulses. The pixel shift at which the interrogation areas are best aligned is indicated by the highest correlation peak in the cross-correlation plane (the maximum value of the cross-correlation function). The displacement of the highest correlation peak from the origin gives the mean displacement of the particles in the time between the laser pulses. Dividing the displacement by the known time between the laser pulses gives the mean velocity of the particles in pixels per pulse. The graph of the discrete cross-correlation between two interrogation areas in shown in Figure 2.7. Carrying out the analysis for all interrogation areas in the PIV photograph yields the flow velocity vector field in the plane of the laser light sheet. Figure 2.8 is a schematic diagram of a velocity vector field obtained by PIV analysis. The computation of the cross-correlation between two images in the spatial domain re-

18
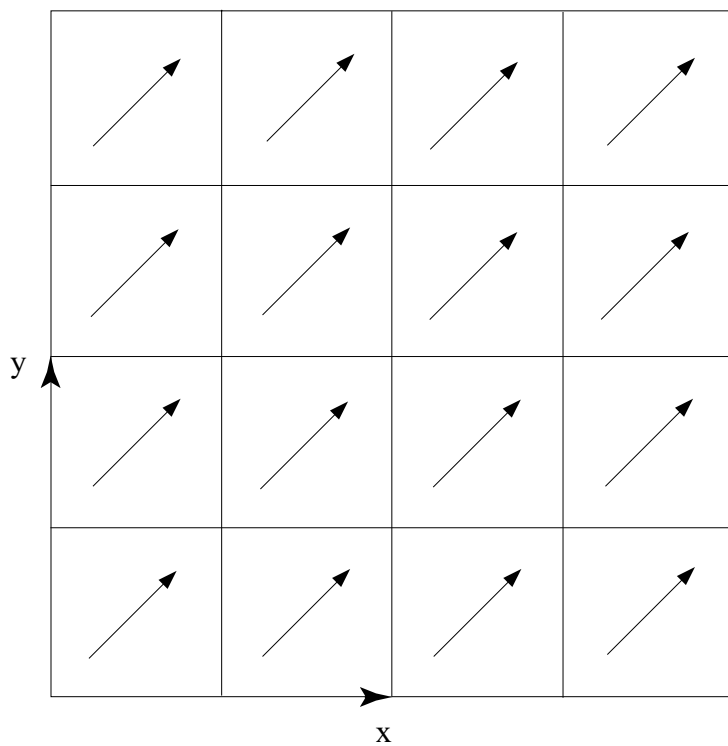
Figure 2.8: *Velocity vector field obtained by cross-correlation.*

quires significant computational resources. Cross-correlation can be performed much faster in the spatial frequency domain using Fourier transform techniques.

Fourier Transform Techniques

Let $I(m, n)$ be an $M \times N$ digital image. The *forward discrete Fourier transform* (DFT) of $I(m, n)$ is defined as

$$\mathcal{F}\{I(m,n)\} = I(\omega_x, \omega_y) = \frac{1}{MN} \sum_{m=0}^{M-1} \sum_{n=0}^{N-1} I(m,n) e^{-2\pi j(\omega_x n/M + \omega_y m/N)} \qquad (2.10)$$

where ω_x and ω_y are spatial frequency variables in the x and y directions respectively and $j = \sqrt{-1}$. The *inverse discrete Fourier transform* is defined as

$$\mathcal{F}^{-1}(F\{I(m,n)\}) = \sum_{\omega_x=0}^{M-1} \sum_{\omega_y=0}^{N-1} I(\omega_x, \omega_y) e^{2\pi j(\omega_x n/M + \omega_y m/N)}. \qquad (2.11)$$

Cyclic Convolution Theorem

Theorem 2.3.1 (Cyclic Convolution) *The discrete Fourier transform of the convolution of $I(m, n)$ with $J(m, n)$ is the product of their discrete Fourier transforms.*

$$\mathcal{F}\{G(m,n)\} = \mathcal{F}\{I(m,n)\} \cdot \mathcal{F}\{J(m,n)\}. \qquad (2.12)$$

20

Convolution in the spatial domain is equivalent to multiplication in the frequency domain. From Equation 2.12,

$$\mathcal{F}^{-1}\left(\mathcal{F}\left\{I\left(m,n\right)\right\}\cdot\mathcal{F}\left\{J\left(m,n\right)\right\}\right)=\mathcal{F}^{-1}\left(\mathcal{F}\left\{G\left(m,n\right)\right\}\right)=I\left(m,n\right)*J\left(m,n\right).$$

(2.13)

According to Equation 2.13, the convolution of an image with another can be obtained by multiplying their Fourier transforms and finding the inverse Fourier transform of the product. The proof of the cyclic convolution theorem is given in [13]. Cyclic convolution is also called circular convolution. Compare the right most term in Equation 2.5 to the right most term in Equation 2.3. The image $J(k-m,n-l)$ in the expression for convolution is $J(-(k-m),-(l-n))$ in the expression for cross correlation rotated 180 degrees. The cross correlation between $I(m,n)$ and $J(m,n)$ is equivalent to the convolution of $I(m,n)$ and $J(-m,-n)$. This means that the convolution theorem can be used to compute the cross-correlation between $I(m,n)$ and $J(m,n)$ in the frequency domain.

Cyclic Cross-correlation Theorem

Let $I\left(m,n\right)$ and $J\left(m,n\right)$ be $M\times N$ images. Let $C\left(m,n\right)$ be the cross correlation between the images $I\left(m,n\right)$ and $J\left(m,n\right)$.

Theorem 2.3.2 (Cyclic cross-correlation) *The discrete Fourier transform of the correlation of $I\left(m,n\right)$ with $J\left(m,n\right)$ is the product of the discrete Fourier transform*

of $I(m,n)$ and the complex conjugate of the discrete Fourier transform of $J(m,n)$.

$$\mathcal{F}\left\{G\left(m,n\right)\right\} = \mathcal{F}\left\{I\left(m,n\right)\right\} \cdot \mathcal{F}^*\left\{J\left(m,n\right)\right\}. \qquad (2.14)$$

From Equation 2.14,

$$\mathcal{F}^{-1}\left(\mathcal{F}\left\{I\left(m,n\right)\right\} \cdot \mathcal{F}^*\left\{J\left(m,n\right)\right\}\right) = \mathcal{F}^{-1}\left(\mathcal{F}\left\{G\left(m,n\right)\right\}\right) = I\left(m,n\right) * J\left(m,n\right).$$
$$(2.15)$$

The cross-correlation theorem provides an alternate formula for calculating the cross correlation between the images $I(m,n)$ and $J(m,n)$ in the frequency domain. In practice, the Fourier transforms required by this approach can be very rapidly calculated using the Fast Fourier Transform (FFT).

Sub Pixel Interpolation

In PIV image analysis, the distance between the peak in the discrete cross-correlation function $C(m,n)$ and the origin of the cross-correlation plane is the mean displacement of the particle images in an interrogation area. Since $C(m,n)$ is a discrete function, the location of the cross-correlation peak is available only at spatial increments equal to the pixel size. The cross-correlation peak can be located with an accuracy of less than one pixel by *sub-pixel interpolation* (also termed *sub-pixel image registration* in the computer vision literature). Sub-pixel interpolation involves fitting a function, usually Gaussian or parabolic, to the discrete cross-correlation function near the peak and finding the location of the maximum in that function.

2.4 Particle Tracking

Correlation particle image velocimetry and particle tracking velocimetry belong to a family of techniques referred to as pulsed light velocimetry. The distinction between the two techniques is based upon the particle image density in the recorded images (see the review article by Adrian [1]). Particle tracking is a relatively old technique. In the early days of pulsed light velocimetry, very low particle densities were used so that the identity of individual particles in multiple exposures was clear. This made particle tracking relatively easy because the task was restricted to finding the particle centroid. There was no confusion over which particle images belonged to which particle. It was recognised, however, that low particle image density lead to low resolution of the velocity field. Therefore, higher particle loadings became common and correlation-based techniques (as described in 2.1) were developed that did not need to identify individual particles. This, coupled with the simultaneous development of digital imaging techniques, lead to rapid development in PIV techniques in the 1990s. Recently, particle tracking algorithms have been incorporated into super-resolution particle image velocimetry algorithms. Here a PIV analysis stage precedes the particle tracking and provides the particle tracking algorithm with an anticipated location for the second particle image. The next section reviews several implementations of this concept.

2.5   Super-resolution PIV Literature

Keane *et al.* [14] coined the term super-resolution PIV. They make the point that the resolution of a particle tracking technique is ultimately determined by the lesser of mean spacing between particles and the distance traveled by particles between laser light pulses. They reported successfully increasing the spatial resolution by a factor of 2.5 for a specific turbulent flow over that achieved by conventional PIV analysis. Their work was performed in the context of double-exposed PIV photographs using auto-correlation analysis techniques whereas this thesis focuses on cross-correlation techniques applied to single-exposed digital images. Their algorithm differs slightly from the one proposed in this thesis in that a successful pair identification is only recognised if a single particle image falls in the search region. They also performed a Monte-Carlo simulation to assess their technique but they used a rather small sample size (300) in their study. Their assessment was restricted to the success rate of the algorithm an did not talk about the uncertainty in the successful measurements.

Guezennec *et al.* [15] describe an analysis technique that appears to be the earliest implementation of the super-resolution concept. They assessed both the success rate and standard deviation of the technique by analysing simulated images, but used small samples (50 images). They identified the most important parameter to be the ability to distinguish between the particles and the background (i.e. the image contrast) and, as a result, the most important algorithm parameter as the threshold.

Keane & Adrian [16] performed a Monte-Carlo simulation of double-exposed PIV photographs. Their main aims were to assess the effects of in-plane velocity gradi-

ents and pair loss due to out-of-plane velocity gradients. They found that a bias was introduced that favoured the high velocity regions of the interrogation area. Their simulated images had no background noise, assumed constant diameter particle images, and used a low particle concentration so that there would be very little chance of particle overlap. In [17] they generalised their approach to multiple pulse systems with similar results.

Cowen & Monismith [18] describe essentially the super-resolution technique but call it the hybrid particle tracking velocimetry technique in reference to the fact that it uses a PIV stage as a preconditioner and a PTV stage which attempts to track individual particles. They are specifically interested in measuring turbulence statistics. So they avoid the usual final step of re-interpolating the random velocity measurements that result from the PTA and calculate the turbulence statistics on a regular grid directly from the randomly positioned velocity measurements.

Rehm & Clemens [19] also describe a hybrid algorithm that is another implementation of the super-resolution concept. They claim that improvements to the technique have been made that allow it to recognise and account for overlapping particle images. They also tested the method with simulated images and applied the technique to turbulent flows and observed a factor of six increase in resolution over conventional PIV. Their technique focussed on double-exposed images where the problem of particle overlap is more pronounced.

In [20], Hart describes a correlation based super-resolution PIV technique. Other super-resolution PIV techniques use a particle tracking stage to produce velocity measurements at a scale smaller than that of the interrogation areas used for the

primary correlation analysis. The correlation based super-resolution technique described in [20] employs recursive correlation analysis on progressively smaller regions to produce velocity measurements at these scales.

2.5.1 Summary

The super-resolution literature contains a number of variations on the technique. However, the essential features are very similar. This thesis will address the need to measure the uncertainty in the technique consistent with international standards [21], [22]. In addition it will establish these uncertainties as functions of a larger number of parameters than are available in the literature.

2.6 Measurement Uncertainty

A measurement result must be reported with a statement of the measurement uncertainty. Measurement uncertainty characterises the dispersion of values that can reasonably be attributed to the measurand. It is an estimate of the limits of the measurement error about the best value of the measurand and is usually expressed at the 95% confidence level. When repeated measurements are made, the best value is taken as the mean of the measurements. This chapter explains the procedure for calculating and reporting measurement uncertainty. The calculation of measurement uncertainty involves statistical analysis. A description of the mathematical background for this chapter is given in Appendix A.

2.6.1 Terminology

Measurement is the procedure of determining the value of a measurable physical quantity. It involves the entity being measured (*measurand*), the entity to which quantitative comparisons are made (*reference*), and the means of comparing the measurand with the reference to render judgement (*comparator*). The result of the measurement is reported with a statement of the quality and reliability of that value.

Metrology is the science of measurement. It is concerned with establishing, reproducing, conserving, and transferring units of measurements and their standards.

Standardisation is minimisation of metrological diversity. International standardisation is acheived by conforming to the International System of Units (SI) [23]. The SI definition of the appropriate unit is the ultimate standard for a measurement result. SI is rational, coherent and comprehensive. The seven base units [23] of SI cover all disciplines.

Realisation is the process, experiment or artifact by which definitions of SI base units are made incarnate.

Primary Standards are the methods and associated instrumentation used to realise SI base units. They are of the highest metrological quality. A primary standard is the starting point for accurate measurement of a quantity as its value, the *primary value* is accepted without reference to any other standard of the same quantity.
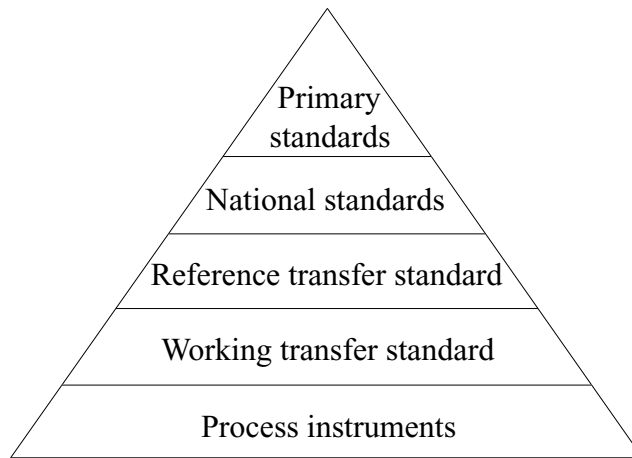
Figure 2.9: *Calibration Pyramid*

Transfer Standards A hierarchy of facilities, procedures, and instruments termed the calibration pyramid transfers primary values to measuring instruments. Figure 2.9 illustrates the calibration pyramid. *Transfer standards* are the instruments used to make the transfer. *Reference transfer standards* are standards of the highest metrological quality at a given location or organisation. If frequent comparisons are made against a national standard it will loose accuracy. Reference transfer standards which are calibrated against the national standard are placed at several locations to prevent this. *Working transfer standards* are used for routine calibration and checking of measuring instruments.

Calibration is the set of operations that establish, under specified conditions, the relationship between values of quantities indicated by a measuring instrument or measuring system, or values represented by a material measure or a reference material and the corresponding values realised by standards [24].
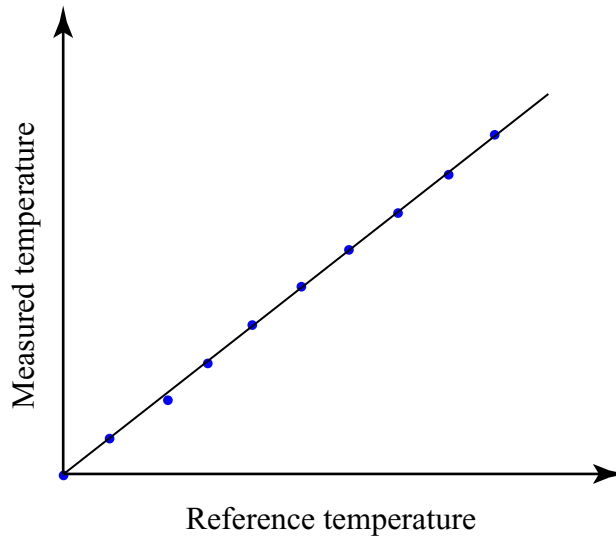
Figure 2.10: *Thermometer Calibration Curve*

Calibration curve A *calibration curve* calibrates a measuring instrument which has a response over a range of values. An instrument is calibrated to reduce systematic errors (see Sections 2.6.2 and 2.6.2) over the response range. The instrument is used to make measurements on reference standards which have known values, at several points in the response range. The calibration curve for the instrument is a linear least squares fit to the scatter plot of measured values vs. reference values. A calibration curve maps a measured value to the correct value. For example, Figure2.10 is a scatter plot of the temperature measured with a thermometer against the corresponding reference temperature. The calibration curve of the thermometer is the linear least squares fit to the scatter plot. It is the line shown in the graph.

Traceability is the property of the result of a measurement or the value of a standard

29

whereby it can be related to stated references, usually national or international standards, through an unbroken chain of comparisons all having stated uncertainties [24].

2.6.2   Measurement Error

Total Measurement Error

It is rare in metrology to report the value of a measurand on the basis of a single measurement. Usually a number of measurements are made and the best value is reported. Frequently, the mean of the sample values is taken as the best value. Consider a sequence of n measurements of a variable X. Let x_{true} be the true value of the variable and x_i be the ith measured value. The total measurement error in the ith measurement of X is

$$\delta_{x_i} = x_i - x_{true}. \tag{2.16}$$

The total measurement error δ_{x_i} is the sum of a fixed component β_{x_i} termed the *systematic error* and a random component ϵ_{x_i} termed the *random error*.

$$\delta_{x_i} = \beta_{x_i} + \epsilon_{x_i}. \tag{2.17}$$

Systematic Error

The systematic error has a constant value β_x for all n measurements:

$$\beta_{x_i} = \beta_x \quad \forall \quad i, \quad i = 1 \ldots n. \tag{2.18}$$

It is defined as the difference between the true value of the measurand and the mean value μ_x of the n measurements:

$$\beta_x = \mu_x - x_{true}. \tag{2.19}$$

It is the error that remains after all possible calibration corrections have been made. Calibration of measuring instruments is intended to eliminate or reduce the systematic error. All systematic errors cannot be eliminated. The systematic error of the primary standard will be retained.

Random Error

The random error ϵ_{x_i} scatters the measurements about the mean value. The random error ϵ_{x_i} is different for each i. Figure 2.11 illustrates the measurement errors for the ith and $i + 1^{\text{th}}$ measurements. As $n \to \infty$ a histogram of the measurements tends to approach a normal curve (Figure 2.12).
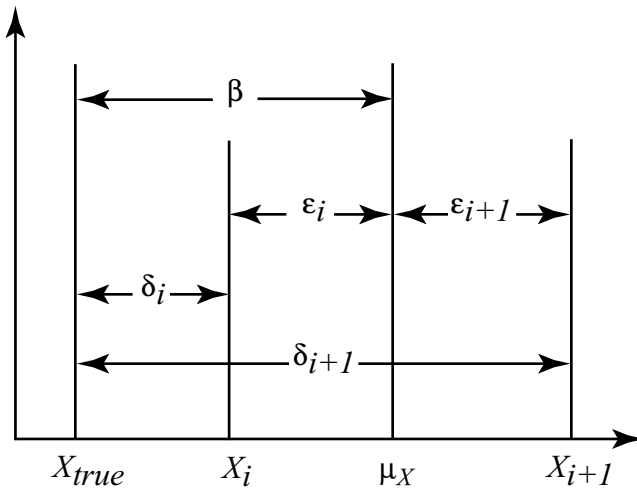
Figure 2.11: *The figure shows the total measurement error in two successive measurements of a variable X. The total measurement error in the ith measurement is made up of a fixed component called the bias error δ_i and a random component called the random error ϵ_i.*
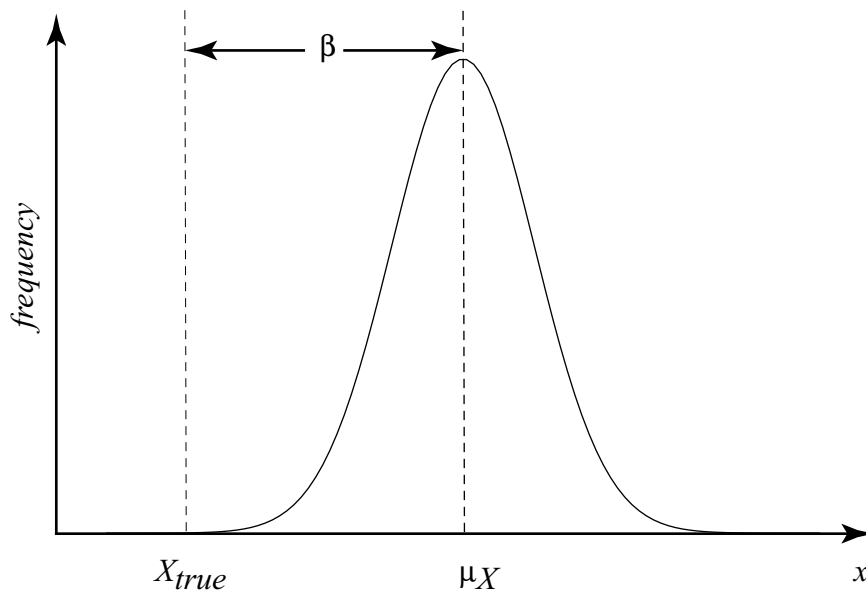
Figure 2.12: *Histogram of n measurements of the variable X as $n \to \infty$. The difference between the mean value μ_X of the n measurements and the true value X_{true} is the bias error β.*

2.6.3 Measurement Uncertainty

The true value of the measurand x_{true} is seldom known. This precludes calculation the total measurement error δ_{x_i} from Equation 2.16. Therefore, δ_{x_i} has to be estimated. The measurement uncertainty is the estimate of the limits of the measurement error. It is reported as a confidence interval about the best value of X (usually the mean of the n measurements) at some level of confidence $C\%$. The International Standards Organisation (ISO) recommends using the 95% confidence level. The *random uncertainty* is the estimate of the limits of the random error. The *systematic uncertainty* is the estimate of the limits of the systematic error.

Random Uncertainty

In Section 2.6.2 it was mentioned that a histogram of the sequence of n measurements of a random variable X tends to approach a normal curve as $n \to \infty$. That is, the meausurements tend to be normally distributed. A sequence of measurements $X_1, X_2 \ldots X_n$ of X form a random sample drawn from a normal distribution. If it were possible to take an infinite number of measurements then the best value of the measurand reported would be the population mean μ_x. When $n \neq \infty$ the best value reported is the sample mean $\bar{X}$. In this case the population mean μ_X is being estimated by the sample mean $\bar{X}$. The 95% confidence interval for the population mean μ_x about the sample mean $\bar{X}$ is given by Equation A.31:

$$P\left(\bar{X} - t_{0.025,\nu} \frac{S}{\sqrt{n}} \leq \mu \leq \bar{X} + t_{0.025,\nu} \frac{S}{\sqrt{n}} \right) = 0.95.$$

The random uncertainty $P_{\bar{X}}$ is defined as the 95% confidence limit about the sample mean $\bar{X}$ by Coleman and Steele [25].

$$P_{\bar{X}} = t_{0.025,\nu} \frac{S}{\sqrt{n}} = t_{0.025,\nu} S_{\bar{X}}, \tag{2.20}$$

The number of degrees of freedom $\nu = n - 1$. As n approaches infinity the t distribution approaches the normal distribution, and $t_{0.025,\nu}$ approaches $1.96 \approx 2$. This value is used in Equation A.17, the confidence interval for the mean of a normal population distribution, and in Equation A.21, the large sample confidence interval. Often in scientific and engineering experiments, the sample sizes are large enough to consider $t_{\alpha,\nu}$ in Equation 2.20 constant at the approximately Gaussian value of two.

After performing Monte Carlo simulations to determine the number of measurements required to consider the sample size large, Coleman and Steele [25] recommend that the t critical value be used for $n < 10$. The approximately Gaussian value 2 can be used for $n \geq 10$. The approximate 95% confidence estimate of the random uncertainty of a variable about the sample mean is

$$P_{\bar{X}} = t_{0.025,\nu} \frac{S}{\sqrt{n}} \qquad\qquad n < 10. \tag{2.21}$$

$$P_{\bar{X}} = 2 \frac{S}{\sqrt{n}} \qquad\qquad n \geq 10. \tag{2.22}$$
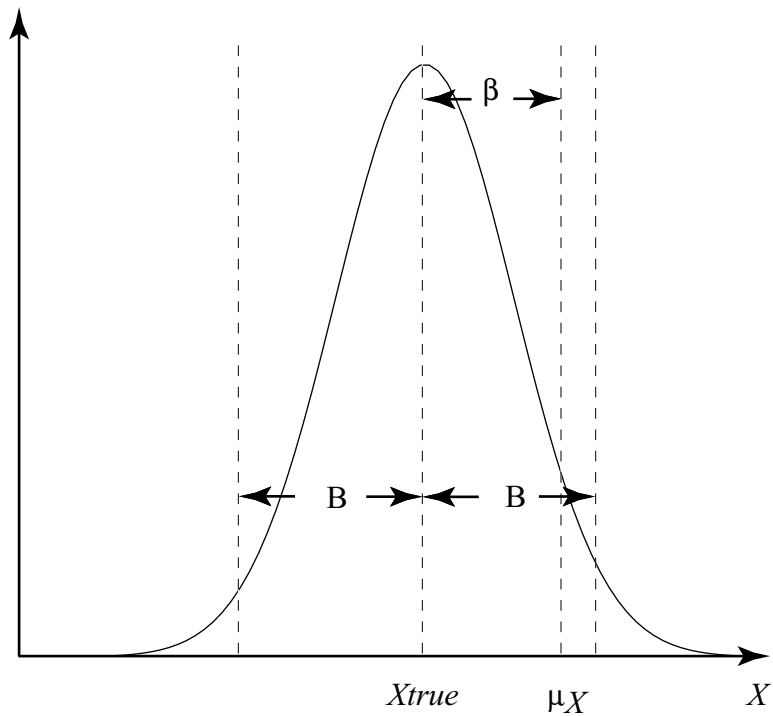
Figure 2.13: *The ANSI/ASME standard [22] and the AIAA standard [26] (by the standards subcommittee, AIAA-GTTC) define the systematic uncertainty B as an estimated value of the limits of the true value of the systematic error β at the 95% confidence level. This is illustrated in the figure. This confidence interval for the systematic uncertainty means that 95% of the time the magnitude of the systematic error β is equal to or less than B.*

Systematic Uncertainty

In obtaining the random uncertainty, there are n sample observations to compute a statistic (e.g., the standard deviation). In calculating the systematic contribution to the uncertainty, there is only a single constant measurement of the systematic error. The true value of the systematic error can be calculated only if X_{true} is known. But X_{true} is usually not known. The ANSI/ASME standard [22] and the AIAA standard [26] (by the standards subcommittee, AIAA-GTTC) define the systematic uncertainty B as an estimated value of the limits of the true value of the systematic error β at the 95% confidence level. This is illustrated in Figure 2.13. This confidence interval for the systematic uncertainty means that 95% of the time the magnitude of the systematic error β is equal to or less than B.

$$|\beta| \leq B \qquad (2.23)$$

To estimate the magnitude of the systematic error, it is assumed that the systematic error for a given case is a single realisation from a parent population of systematic errors having some statistical distribution. If the distribution is assumed to be normal with standard deviation S_β, the interval

$$\pm B = \pm 2S_\beta \qquad (2.24)$$

will include approximately 95% of all systematic errors that can be realised from the parent population.

2.6.4 Combined Standard Uncertainty

The systematic and random uncertainties are combined to produce the *combined random uncertainty u_c*. The ISO Guide to the expression of uncertainty in measurement (GUM) [21] methodology specifies that the combined standard uncertainty u_c should be obtained by adding the variances for the systematic and random errors. The standard deviation for the systematic error is obtained from Equation 2.24.

$$S_B = \frac{B}{2} \tag{2.25}$$

If the confidence interval is specified about the sample mean $\bar{X}$, the estimated standard deviation for the random error is obtained from 2.20.

$$S = \frac{S}{\sqrt{n}}. \tag{2.26}$$

By definition, the variance is the square of the standard deviation. Equation 2.25 and Equation 2.26 give the variances for the systematic and random errors. The combined standard uncertainty is

$$u_c^2 = S_B^2 + S_{\bar{X}}^2. \tag{2.27}$$

The Central Limit Theorem implies that the distribution of the total error δ for a measured variable should approach the normal distribution. The combined standard uncertainty u_c can be considered as the standard deviation of this total error distribution.

2.6.5   Overall Uncertainty

The *overall uncertainty* of a measured variable X is the interval around its best value where X_{true} is expected to be, at given confidence level. The overall uncertainty is calculated by combining the systematic uncertainty and the random uncertainty. The ISO Guide advises a coverage factor **k** to specify a confidence level with the combined standard uncertainty of a variable.

$$U_\% = \mathbf{k} u_c \tag{2.28}$$

where $U_\%$ is the overall uncertainty at a particular confidence level. X_{true} will be within the $\pm U$ limit. Because the distribution of the total errors is normal, the ISO Guide recommends using the t distribution, and therefore the t critical values for the coverage factor:

$$U_\% = t_\% u_c. \tag{2.29}$$

At the 95% confidence level

$$U_{95} = t_{0.025,\nu} u_c. \tag{2.30}$$

The number of degrees of freedom ν in Equation 2.30 is approximately given by the Welch-Satterthwaite formula:

$$\nu = \frac{\left(S_B^2 + S_{\bar{X}}^2\right)^2}{\frac{S_B^4}{\nu_{S_B}} + \frac{S_{\bar{X}}^4}{\nu_{S_{\bar{X}}}}} \tag{2.31}$$

where ν_{S_B} and $\nu_{S_{\bar{X}}}$ are respectively the degrees of freedom associated with S_B and $S_{\bar{X}}$. The estimate of ν_{S_B} recommended by the ISO Guide is

$$\nu_{S_B} = \frac{1}{2}\left(\frac{\Delta B}{B}\right)^{-2} \tag{2.32}$$

where ΔB is the relative uncertainty of B. For sample size n,

$$\nu_{S_{\bar{X}}} = n - 1. \tag{2.33}$$

2.6.6 Large Sample Overall Uncertainty

In most engineering problems ν is large enough to consider the values in Equation 2.29 constant for a given confidence level. Coleman and Steele [25] state that the large sample approximation can be used for $\nu \geq 9$. At the 95% confidence level, the constant t critical value is

$$t_{0.025,\nu} = 2. \tag{2.34}$$

Using this value in Equation 2.30,

$$U_{95} = 2u_c = \sqrt{(2S_B)^2 + (2S_{\bar{X}})^2} \tag{2.35}$$

From Equation 2.24

$$2S_B = B,$$

the systematic uncertainty. From Equation 2.22, when $n \geq 10$

$$2S_{\bar{X}} = 2\frac{S}{\sqrt{n}} = P_{\bar{X}},$$

the random uncertainty. The overall uncertainty about the sample mean for large sample sizes is

$$U_{95} = \sqrt{B^2 + P_{\bar{X}}^2}\ . \tag{2.36}$$

This work reports the overall uncertainty U_{95} (Equation 2.36) in velocity measurements made by the particle tracking algorithm. The systematic error and random uncertainty can equivalently be calculated from a sample of total measurement errors. This is explained next. Consider a sequence of n measurements of a variable X. Let x_{true} be the true value of the variable and x_i be the ith measured value. Let μ_x and s_x be the mean and standard deviation of the n measurements. The total measurement error in the ith measurement of X is

$$\delta_{x_i} = x_i - x_{true}.$$

When a constant value is subtracted from each element of a sample, the sample mean is reduced by that constant value, while the sample standard deviation remains the same. In the equation for the total measurement error above, x_{true} is a constant. Therefore the mean of the n measurement errors is

$$\mu_{\delta_x} = \mu_x - x_{true}. \tag{2.37}$$

40

The mean of the sample of total measurement errors, $\mu_x - x_{true}$, is the systematic error β_x (see Equation 2.19) in the n measurements. The standard deviation of the n measurement errors is $s_{\delta_x} = s_x$, the standard deviation of the measurements. The systematic uncertainty is $2s_x/\sqrt{n}$. In this thesis the systematic error and random uncertainty are calculated from the sample of total measurement errors.

Chapter 3

Measurement of PTA Uncertainty

This chapter begins with a description of the particle tracking algorithm implemented in this thesis. It then describes the simulation that was done to measure the uncertainty in the particle tracking algorithm. This process involves both generating simulated images and analysing these images to yield an assessment of the uncertainty.

3.1   Details of the Current PTA

The super-resolution PIV technique augments the correlation PIV analysis with a second pass that attempts to track specific particles in the flow. The particle tracking algorithm measures flow velocity in several steps. Individual particles are identified on both images. The location of each particle image is calculated as its intensity weighted centroid. Paired particle images are identified and the displacements between pair members are calculated. The velocity of a particle is assigned to the midpoint of the
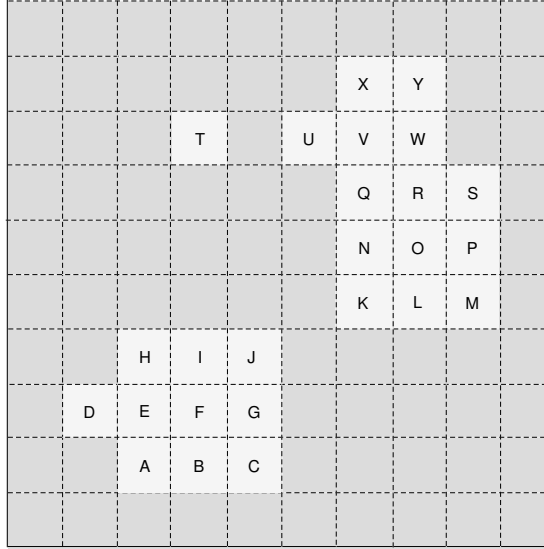
Figure 3.1: *Schematic representation of portion of a PIV photograph. Particle images are groups of pixels above a specified threshold. Pixels above the threshold are highlighted. The letters will be referred to in the description of the PTA.*

line joining the centroids of its images. An optional final step is the interpolation of the randomly placed velocity vectors onto a regular grid.

3.1.1 Particle Identification

Figure 3.1 shows a schematic representation of a portion of a PIV photograph. A particle image is a group of adjacent pixels whose intensities are above a specified threshold I_t. The threshold influences the number and size of identified particles. Therefore, it is a critical algorithm parameter and its effect on the uncertainty of the super-resolution technique is investigated in this thesis.

Identifying particle images computationally is not trivial. Every pixel is assigned a *particle identification number* (PIN), that is used to identify which particle each

pixel belongs to. Initially, every pixel is assigned a PIN of −1. Let `leftpin` and `lowerpin` denote the PIN of the left and lower neighbour of a pixel respectively. The image is scanned from the bottom left corner to the top right corner in a row wise fashion and each pixel above the specified threshold has its PIN set depending upon the PIN of its left and lower neighbour. During this process, only the pixels below and to the left of the current pixel can potentially have their particle identification numbers set to something other than −1. For a pixel in the left most column of the image `leftpin` is taken as −1. For a pixel in the lowest row `lowerpin` is taken as −1. The PIN is set according to the following rules:

1. `lowerpin` < 0 and `leftpin` < 0. The PIN of both the left and lower neighbour is less than 0. In this case a new particle appears to have been found. The PIN for this pixel is set to the next available integer, starting at 0. In Figure 3.1, rule 1 applies to the pixels labelled A, D, K, T, and U.

2. `lowerpin` ≥ 0 or `leftpin` ≥ 0. The PIN of either the left neighbour or the lower neighbour is non-negative. In this case, the current pixel is given the same PIN as its non-negative neighbour. In Figure 3.1 rule 2 applies to pixels B, C, H, L, M, N, Q, and X.

3. `lowerpin` = `leftpin` ≠ −1. Both the left and the lower neighbours have the same non-negative PIN. The current pixel is given this PIN.

4. `lowerpin` ≥ 0 and `leftpin` ≥ 0 but `lowerpin` ≠ `leftpin`. The left and lower neighbours have different non-negative PINs. Since the current pixel connects its left and lower neighbours and they have previously been identified as belonging to different particles this causes problems. The PIN of the current pixel is set to

Figure 3.2: *Particle identification numbers for each pixel after one scan of the image.*

min[leftpin, lowerpin], the minimum of the two. In Figure 3.1 rule 4 applies at pixels E and V.

Figure 3.2 shows the PIN for each pixel after one scan of the image. Next, contiguous pixels are renumbered to have the same PIN. A flag array maintains a record of which pixels need to be renumbered in order that all pixels of a particle have the same PIN. Figure 3.3 shows the photograph after renumbering of pixels. All particles have been identified. The final step is to eliminate missing particle numbers that arise from the renumbering procedure. Figure 3.4 shows the photograph after missing particles numbers have been eliminated.

The threshold I_t determines whether overlapping particle images can be distinguished. Overlapped images which have a common boundary where pixel intensities are below the threshold are distinguishable. Otherwise they are considered to be a
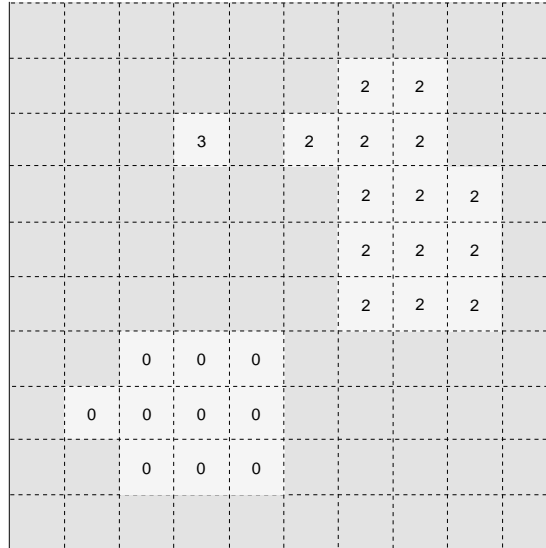
Figure 3.3: *Example photograph after renumbering contiguous pixels.*
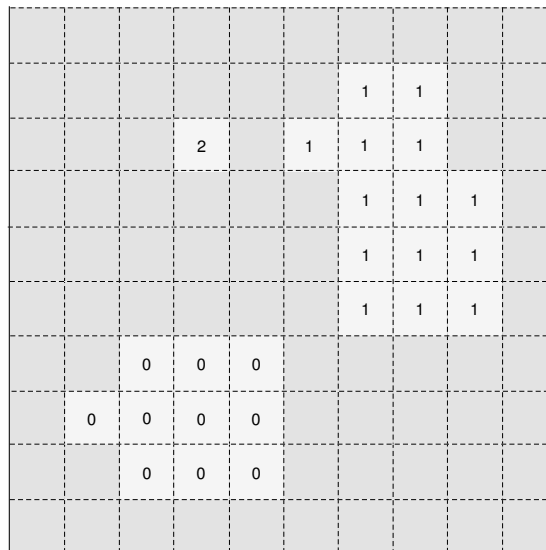
Figure 3.4: *Example photograph after particle identification.*

single particle. This is a limitation of the particle identification algorithm.

3.1.2   Particle Location

The x and y coordinates of the centres of identified particles are calculated as the intensity-weighted averages of pixels having the same PINs:

$$\bar{x} = \frac{\sum_{i=1}^{n} I_i x_i}{\sum_{i=1}^{n} I_i} \tag{3.1}$$

$$\bar{y} = \frac{\sum_{i=1}^{n} I_i y_i}{\sum_{i=1}^{n} I_i} \tag{3.2}$$

where I_i is the intensity of the ith pixel constituting the particle, (x_i, y_i) is the location of the centre of the ith pixel, $(\bar{x}, \bar{y})$ is the location of the particle spot and n is the number of pixels constituting the particle. The location of each particle is saved and the search for particle pairs is carried out.

3.1.3   Pair Identification

The mean velocity obtained by cross-correlation PIV is assigned to the centre of the corresponding interrogation area. The velocity at the location of each identified particle in the first image is required for the pair search. This is obtained by interpolation from the PIV results as explained in the next section.

Interpolation of Velocity to Particle Location

Figure 3.5 shows a PIV image divided into equal sized interrogation areas. An *inter-polation grid* is formed by horizontal and vertical dotted lines through the centres of the interrogation areas. The centres of adjacent interrogation areas form the corners of square interpolation regions on the grid. Consider the interpolation region shown shaded in Figure 3.5 with corners $A(x_A, y_A)$, $B(x_B, y_B)$, $C(x_C, y_C)$ and $D(x_D, y_D)$. The velocity $u(x, y)$ of a particle located at (x, y) inside $ABCD$ is interpolated from the corner velocities using the equation

$$u = \alpha + \beta x + \gamma y + \delta xy. \tag{3.3}$$

The coefficients α, β, γ, and δ are:

$$\alpha = \frac{u_A x_B y_C - u_B x_A y_C - u_C x_B y_A + u_D x_A y_A}{\Delta x \Delta y} \tag{3.4}$$

$$\beta = \frac{-u_A y_C + u_B y_C + u_C y_A - u_D y_A}{\Delta x \Delta y} \tag{3.5}$$

$$\gamma = \frac{-u_A x_B + u_B x_A + u_C x_B - u_D x_A}{\Delta x \Delta y} \tag{3.6}$$

$$\delta = \frac{u_A - u_B - u_C + u_D}{\Delta x \Delta y} \tag{3.7}$$

where u_A, u_B, u_C, and u_D are the velocity at the corners of $ABCD$ and Δx and Δy are the dimensions of the interpolation region (see Figure 3.5). The coefficients are

48

obtained by solving the system

$$u_A = \alpha + \beta x_A + \gamma y_A + \delta x_A y_A, \tag{3.8a}$$

$$u_B = \alpha + \beta x_B + \gamma y_B + \delta x_B y_B, \tag{3.8b}$$

$$u_C = \alpha + \beta x_C + \gamma y_C + \delta x_C y_C, \text{ and} \tag{3.8c}$$

$$u_D = \alpha + \beta x_D + \gamma y_D + \delta x_D y_D. \tag{3.8d}$$

The details are given in Appendix E. System 3.8a – 3.8d results when Equation 3.3 is applied at the corners of $ABCD$. Similarly, Equation 3.3 is used to obtain $v(x, y)$ at any location inside $ABCD$. The interpolation coefficients in this case are:

$$\alpha = \frac{v_A x_B y_C - v_B x_A y_C - v_C x_B y_A + v_D x_A y_A}{\Delta x \Delta y}, \tag{3.9}$$

$$\beta = \frac{-v_A y_C + v_B y_C + v_C y_A - v_D y_A}{\Delta x \Delta y}, \tag{3.10}$$

$$\gamma = \frac{-v_A x_B + v_B x_A + v_C x_B - v_D x_A}{\Delta x \Delta y}, \text{ and} \tag{3.11}$$

$$\delta = \frac{v_A - v_B - v_C + v_D}{\Delta x \Delta y}. \tag{3.12}$$

Particles located near the borders of the image do not lie in interpolation areas where the velocity at the four corners is available. The velocity at such locations is extrapolated from the nearest interpolation region using Equation 3.3. This extrapolation technique is not important to this study since all test particles are placed in the central interpolation region where extrapolation is not necessary.
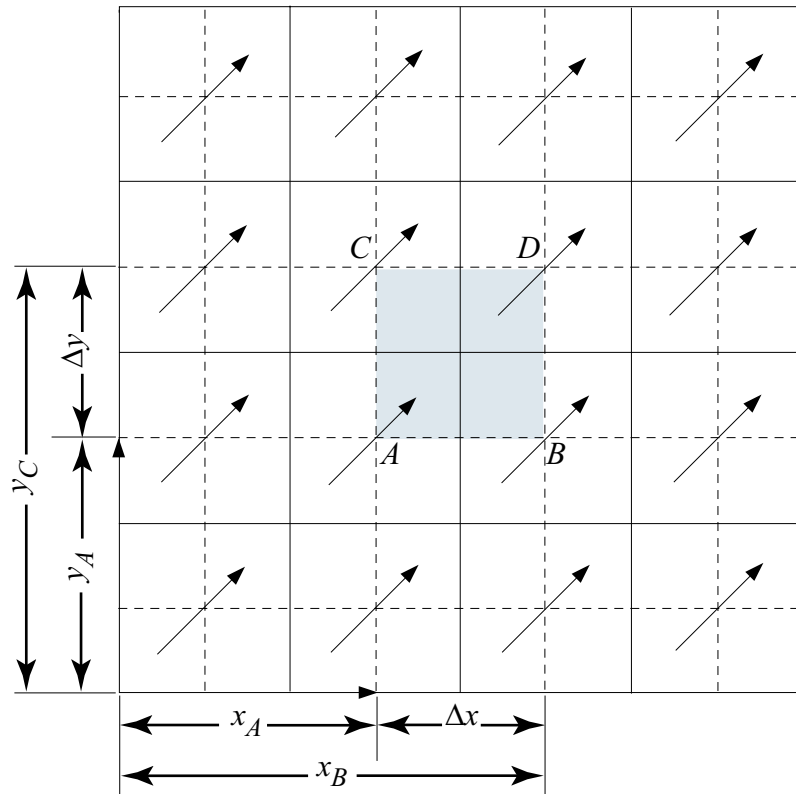
Figure 3.5: *Schematic of the interrogation areas and interpolation grid. The solid lines represent the interrogation areas for the PIV stage of the analysis. The interpolation region is shown shaded.*

Pair Search

Figure 3.6 illustrates the pair search procedure. The interpolation region in which each particle on the first photograph is situated is determined. The velocity components $u(x, y)$ and $v(x, y)$ at this location is interpolated from the coarse grid PIV results using Equation 3.3. An estimate of the expected location on the second photograph where the pair is likely to be is made using the interpolated velocity. The distance from the expected location $E(x_e, y_e)$ to every particle within the specified search radius r_s is calculated. The particle closest to the expected location $E(x_e, y_e)$ and within the search radius is taken to be the matching particle. A particle identified as a member of a pair cannot be a member of another pair. Therefore, this particle is eliminated from the list of particles on the second image. If no particles lie within the search radius, the search was unsuccessful and the next particle in the list is considered.

The procedure is repeated until all particles in the first image have been considered. Each pair of particles found is added to a list of pairs. For each pair, the x and y distances between the particles are calculated to yield the velocity in pixels/pulse. This velocity is considered to be a measurement of the velocity at a location midway between the two particles.

3.1.4 Velocity Interpolation to Regular Grid

Irregularly spaced velocity data obtained by particle tracking is typically interpolated onto a regular grid. The interpolation of the randomly placed velocity vectors onto a

First PIV image.   Second PIV Image.
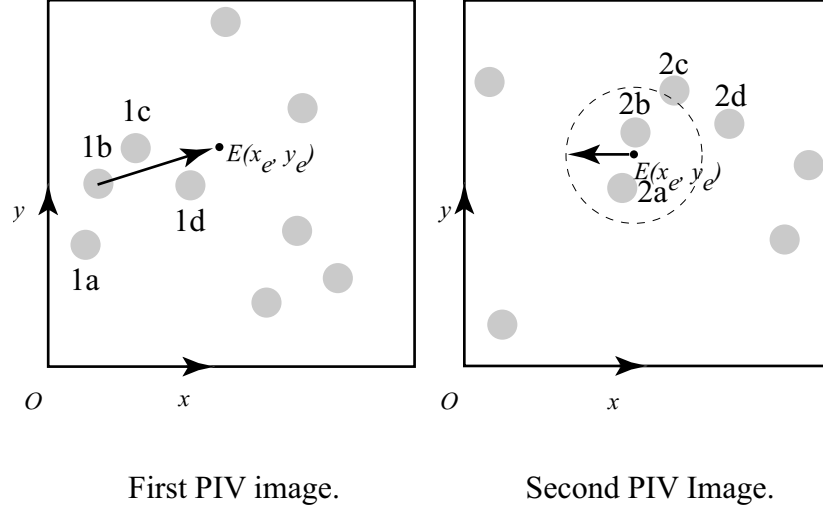
Figure 3.6: *Schematic diagram of the pair search. Particle 2b, within the specified search radius and nearest the expected location is taken as the pair to particle 1b.*

regular grid, and errors in the interpolation procedure do not form part of this study. The method described by Spedding and Rignot [27] is the interpolation scheme used here. The value of an interpolation function $F(x, y)$ is computed at every node (x, y) of a regular grid from the weighted sum of k known data points, f_k.

$$F\left(x, y\right) = \frac{\sum\limits_{k=1}^{n} w_k\left(x, y\right) f_k}{\sum\limits_{k=1}^{n} w_k\left(x, y\right)}. \tag{3.13}$$

All velocity data points f_k which are within a 50 pixel radius from the regular grid node is used to calculate the value at the node. The weighting function $w_k = f(d_k)$ is a function of the distance

$$d_k = \sqrt{\left(x_k - x\right)^2 + \left(y_k - y\right)^2} \tag{3.14}$$

of the known data points (x_k, y_k) from the node (x, y). A Gaussian weighting function given by

$$w_k = f(d_k) = e^{-(d_k/R_w)^2} \tag{3.15}$$

is used. R_w is the width of the Gaussian function, i.e the radial distance where the function w_k falls to a value of 0.3678 from its central value of one. For this study $R_w = 10$. If there are no data points within the 50 pixel radius, the velocity at the regular grid node is set to 0. Once $u(x, y)$ and $v(x, y)$ are interpolated onto the regular grid, a quantity of interest, e.g., the vorticity ω_z can be computed using finite differences.

3.2 Artificial PIV Images

This section describes the generation of artificial 8-bit, 256×256 pixel greyscale image pairs to simulate dual-frame PIV images of a simple shear flow. Images of illuminated particles are referred to as particle images or particle spots. Generating a pair of dual-frame PIV images involves modelling the flow, initialising the background, placing spurious particles, placing the test particle, and placing the paired particles.

1. Modelling the flow: A mathematical model of the flow velocity field is chosen. This model will allow the exact velocity at any point in the flow to be determined, allowing an assessment of the error in the image processing procedure to be made.

2. Initialising the background: Background noise is assumed to be Gaussian. Both images are initialised with a background having a Gaussian intensity distribution with a specified mean and standard deviation.

3. Placing spurious particles: A specified number of *spurious* or unpaired particles are placed on both images at random locations. These particles simulate the effect of motion normal to the light sheet.

4. Placing the test particle: An image of the *test particle* is placed inside the *interpolation region* on the first PIV image. Its pair is placed on the second image at a location determined by the mathematical description of the flow field.

5. Placing paired particles: A number of *paired particles* (particles other than the test particle that appear on both the first image and the second image) are placed. For each pair, the first particle image is placed at a random location on the first image. The location of its pair on the second image is determined by the velocity field.

3.2.1   Simulated Velocity Field

Velocity gradients are responsible for rotations in a flow. The measurement uncertainty of the tracking algorithm in the presence of velocity gradients should be ascertained prior to velocimetry in rotational flows. Therefore, a simple shear flow with a constant velocity gradient $\partial u/\partial y$ was simulated.

Consider the two-dimensional incompressible velocity field

$$u = a + by \tag{3.16a}$$

$$v = c + dx \tag{3.16b}$$

where u is the x component of the velocity, v is the y component of the velocity and

$b = du/dy$, $d = dv/dx$ are constant velocity gradients.

In this work it is assumed that the particles have been suitably selected so that they follow the flow. E rrors due to particle dynamics are assumed to be negligible compared to errors in the image processing. Pathlines $x(t)$ and $y(t)$ can be obtained by solving the following system of ordinary differential equations corresponding to Equations 3.16a and 3.16b.

$$dx/dt = a + by \tag{3.17a}$$

$$dy/dt = c + dx \tag{3.17b}$$

The Maple computer algebra system gives the following solutions:

$$
x(t) = \frac{\left(bc + a\sqrt{bd} + bdx_0 + b\sqrt{bd}y_0\right) e^{\sqrt{dbt}}}{2bd} - \frac{c}{d}
$$
$$
- \frac{\left(ad - c\sqrt{bd} - d\sqrt{bd}x_0 + bdy_0\right) e^{-\sqrt{dbt}} \sqrt{db}}{2d^2b}
\tag{3.18a}
$$

$$
y(t) = \frac{\left(ad - c\sqrt{bd} - d\sqrt{bd}x_0 + bdy_0\right) e^{-\sqrt{bdt}}}{2bd} - \frac{a}{b}
$$
$$
+ \frac{\left(bc + a\sqrt{bd} + bdx_0 + b\sqrt{bd}y_0\right) e^{\sqrt{bdt}} \sqrt{bd}}{2b^2d}
\tag{3.18b}
$$

where x_0 and y_0 are initial conditions representing the position $x(0)$ and $y(0)$.

Equations 3.18a and 3.18b can be written as

$$x(t) = \frac{(c + x_0 d)\cosh\left(\sqrt{bd}t\right) - c}{d}$$
$$+ \frac{(a/b + y_0)\sinh\left(\sqrt{bd}t\right)\sqrt{bd}}{d} \tag{3.19a}$$

$$y(t) = \frac{(a + y_0 b)\cosh\left(\sqrt{bd}t\right) - a}{b}$$
$$+ \frac{(c/d + x_0)\sinh\left(\sqrt{bd}t\right)\sqrt{bd}}{b} \tag{3.19b}$$

When $b = 0$ in Equation 3.18b or $d = 0$ in Equation 3.18a care must be taken to properly evaluate the limits. For all images generated in this thesis $d = 0$. Taking the limit as $d \to 0$ gives the following expressions for $x(t)$ and $y(t)$:

$$x(t) = \frac{cbt^2}{2} + x_0 + (a + by_0)\,t. \tag{3.20a}$$

$$y(t) = y_0 + ct. \tag{3.20b}$$

The streamfunction $\psi(x, y)$ for the shear flow is (see Appendix B)

$$\psi(x, y) = ay + \frac{by^2}{2} - cx - \frac{dx^2}{2}. \tag{3.21}$$

The flow can be visualised by plotting lines of constant ψ, the streamlines. Figure 3.7 is a streamline plot for $a = b = c = d = 1$. A streamline plot for the base case
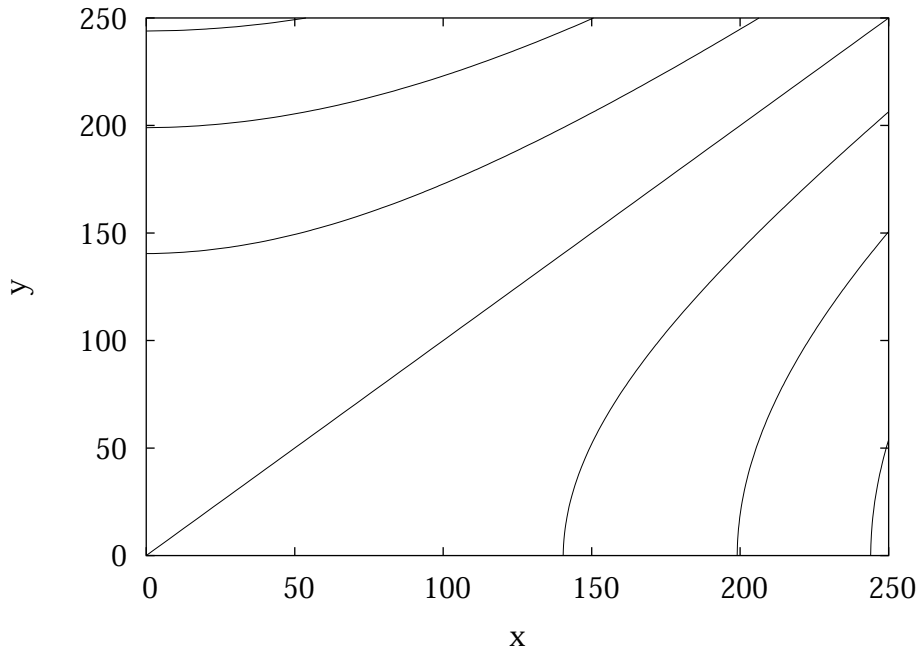
Figure 3.7: *Streamline plot for $\psi(x, y)$ with $a = b = c = d = 1$*

conditions $a = 8, b = 0.05, c = 2, d = 0$ is given in Figure 3.8. For steady flows such as this, streamlines and pathlines are identical.

3.2.2 Background Noise

When background noise is absent, the particle images should be silhouetted against a perfectly black background on a PIV image. In practice, the background is not perfectly black as there is always some inexpungible noise. This may be shot noise associated with the CCD array or noise due to light sources other than the particles of interest. Examples of extraneous light sources are room lights and computer monitors. A more significant stray light source in practice is laser light reflected off of
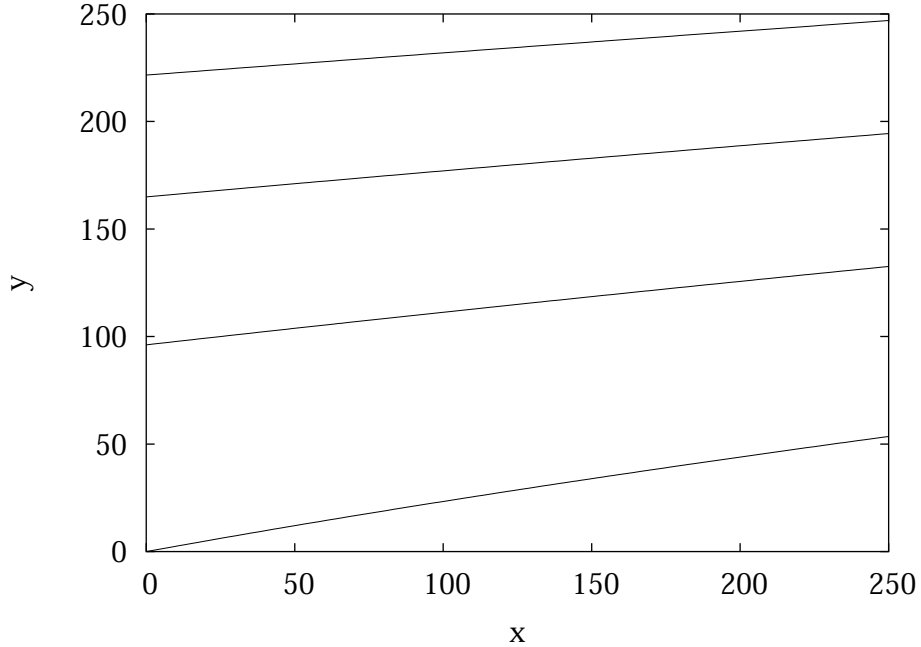
Figure 3.8: *Streamline plot for $\psi(x, y)$ with $a = 8, b = 0.05, c = 2, d = 0$*

various surfaces of the apparatus. This light illuminates particles which are not in the light sheet and they will appear out of focus on the image plane. Background noise is simulated by initialising the images with a Gaussian intensity distribution using Equation 3.22.

$$I_b = Z\sigma_{I_b} + \mu_{I_b} \tag{3.22}$$

I_b is the background intensity, μ_{I_b} is the mean background intensity and σ_{I_b} is the standard deviation of the background intensity. A Gaussian random number generator generates a standard normal random variable Z at each pixel location. Any value of I_b less than zero is set to zero and any value greater than 255 is set to 255. The base case value of the mean background intensity was 120 (see Table 4.2). Because

58

the mean background intensity influences particle image identification the effect of varying μ_{I_b} on the PTA performance was studied.

3.2.3 Particle Images

Particle Image Intensity Profile

The intensity profile $I(r)$ of a particle image is assumed to be Gaussian:

$$I(r) = I_0 e^{-(r/R_p)^2} \tag{3.23}$$

where I_0 is the intensity at the particle centre, $I(r)$ is the intensity at radial distance r from the spot centre and R_p is the radial distance at which the intensity is $0.3768 I_0$. All seeding particles do not have the same diameter. The diameters are likely to be normally distributed. To consider the variation in seeding particle diameters, particle image diameters are drawn from a normally distributed population with mean μ_D and standard deviation σ_D:

$$D_p = Z\sigma_D + \mu_D. \tag{3.24}$$

The central intensity I_0 of the particle image is a function of particle position within the light sheet and the efficiency with which the particle scatters the incident light. Figure 3.9 shows the volume in the flow illuminated by the light sheet. The light sheet is centred at $z = 0$. For a light sheet with a Gaussian profile along the z
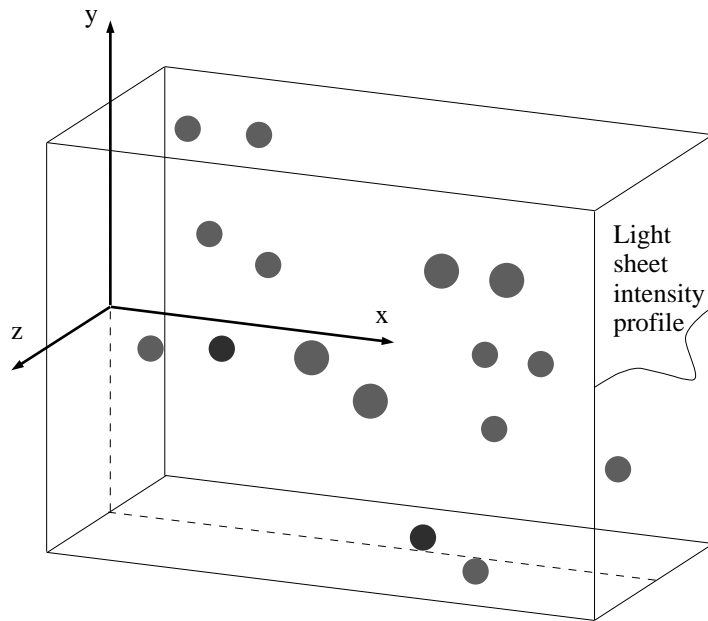
Figure 3.9: *Light sheet intensity profile. Adapted from Markus Raffel et. al. [5].*

coordinate axis, the central intensity I_0 is [5]

$$I_0 = qe^{-8z^2/\Delta z_0^2}, \tag{3.25}$$

where q is the efficiency with which the particle scatters light and Δz_0 is the thickness of the light sheet between the e^{-2} waist points. Equation 3.25 implies that even if particles of the same diameter were to be illuminated in the light sheet, a particle closer to the centre of the light sheet would register on the PIV photograph with a greater intensity. This is simulated by drawing I_0 from a normally distributed population with a specified mean μ_{I_0} and standard deviation σ_{I_0}:

$$I_0 = Z\sigma_{I_0} + \mu_{I_0} \tag{3.26}$$

The performance of the PTA as the parameter μ_{I_0} was varied was studied. The base case value of μ_{I_0} is 120 (see Table 4.2). The central intensity affects image contrast from the background. Therefore, it affects the performance of the PTA.

Particle Image Generation

To generate a particle image (1) a location is selected for the image, (2) pixels constituting the image are identified and, (3) the intensity of each pixel in the image is set. Figure 3.10 shows a spot on a PIV image. The xOy coordinate system has its origin at the bottom, left corner. The $x'O'y'$ coordinate system has its origin at the centre of the particle. In both, unit length is the length of a pixel. To place an image at a random location, a random number generator is called twice to obtain two uni-

form deviates (real random numbers which have equal probability of being anywhere between 0 and 1). They are multiplied by 255 to obtain real random numbers x_p and y_p in the range $[0, 255]$. The spot centre is (x_p, y_p).

The radius of the particle image R_p is the distance from its centre to where the intensity falls to $0.3768I_0$.

$$I(R_p) = 0.3768I_0. \tag{3.27}$$

The central intensity I_0 is drawn from a normal distribution (Equation 3.26). Equation 3.24 is used to determine the spot diameter D_p. Since D_p is normally distributed, the radius

$$R_p = D_p/2 \tag{3.28}$$

is also normally distributed. The intensity is adjusted according to the Gaussian profile only for pixels which fall inside a radius $r = R_{I=1}$ from the centre such that $I(R_{I=1}) = 1$. In $x'O'y'$ coordinates (Figure 3.10), Equation 3.23 is

$$I(x', y') = I_0 e^{-\left(x'^2 + y'^2\right)/R_p^2}. \tag{3.29}$$

The level curve $I(x', y') = 1$ of Equation 3.29 on the $x'y'$ plane is circular. Substituting $I(R_{I=1}) = 1$ in Equation 3.23 gives

$$\frac{1}{I_0} = e^{-(R_{I=1}/R_p)^2}. \tag{3.30}$$

From Equation 3.30

$$R_{I=1} = R_p\sqrt{\ln I_0}. \tag{3.31}$$
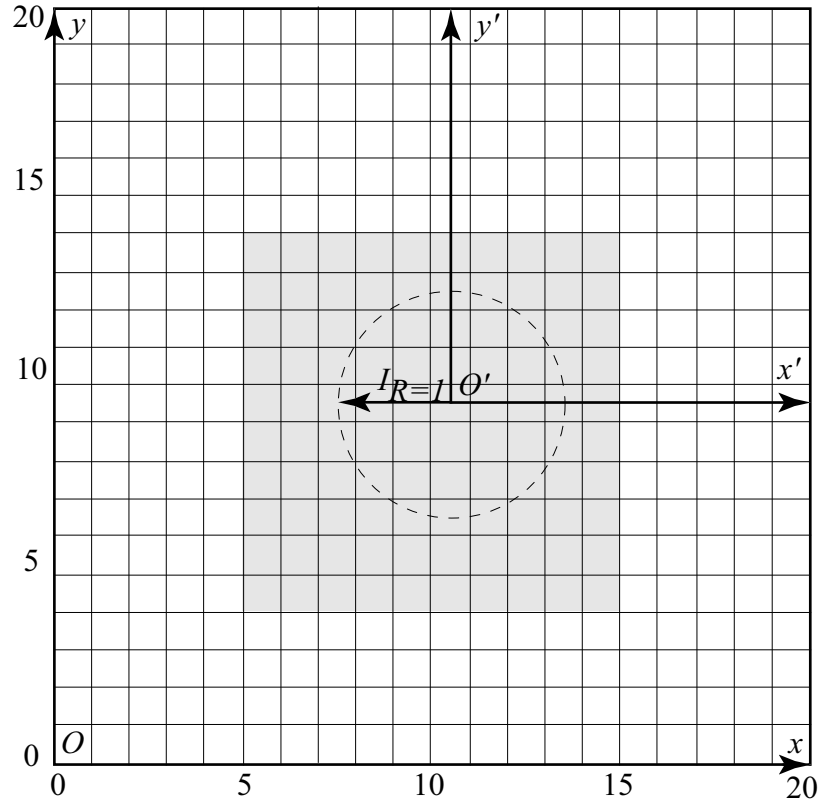
Figure 3.10: *Schematic diagram of a single particle image on an artificial PIV image.*

Two pixels were added to $R_{I=1}$ to ensure that all pixels affected by the particle are considered. Intensities are adjusted for pixels which fall within a square region centred on the centre of the particle image, with side length

$$R_a = 2 \times R_p \sqrt{\ln I_0} + 2. \tag{3.32}$$

In the corners of the square region the intensity I due to the particle will be less than one.

The pixel intensity is set to a brightness level which is the maximum of the value calculated from Equation 3.29, and the background intensity. Equation 3.23 shows that the intensity of a particle image subsides continously with distance from its central value I_0. However, pixels constituting the spot can only assume an integer value in the range $[0, 255]$. Each pixel is set to the average value of the intensity function (Equation 3.29) over its area. Physically, this corresponds to the fact that the output of a single element of a CCD array (pixel) is determined by the total light which is incident upon it.

The average value of a function $f(x, y)$ of two variables defined on a closed rectangle $\mathbf{R} = [\mathbf{a}, \mathbf{b}] \times [\mathbf{c}, \mathbf{d}] = \{(x, y) \in \mathbb{R}^2 | \mathbf{a} \leq x \leq \mathbf{b}, \mathbf{c} \leq y \leq \mathbf{d}\}$ is

$$\bar{f}(x, y) = \frac{1}{A(\mathbf{R})} \iint\limits_{\mathbf{R}} f(x, y) dA. \tag{3.33}$$

$A(\mathbf{R})$ is the area of the rectangle $\mathbf{R}$. Figure 3.11 shows a single particle image on a PIV image. Coordinate system xOy has origin O at the bottom, left corner of the image. Coordinate system $x'O'y'$ has origin O' at the particle image centre. Unit length is the length of a pixel in both xOy and $x'O'y'$ coordinates. The particle image is represented in xOy coordinates by the rectangle

$$\mathbf{S} = [i, j] \times [k, l]. \tag{3.34}$$

with left, right, bottom and top edges i, j, k and l respectively. Let

$$\mathbf{P} = [e, f] \times [g, h] \tag{3.35}$$

64
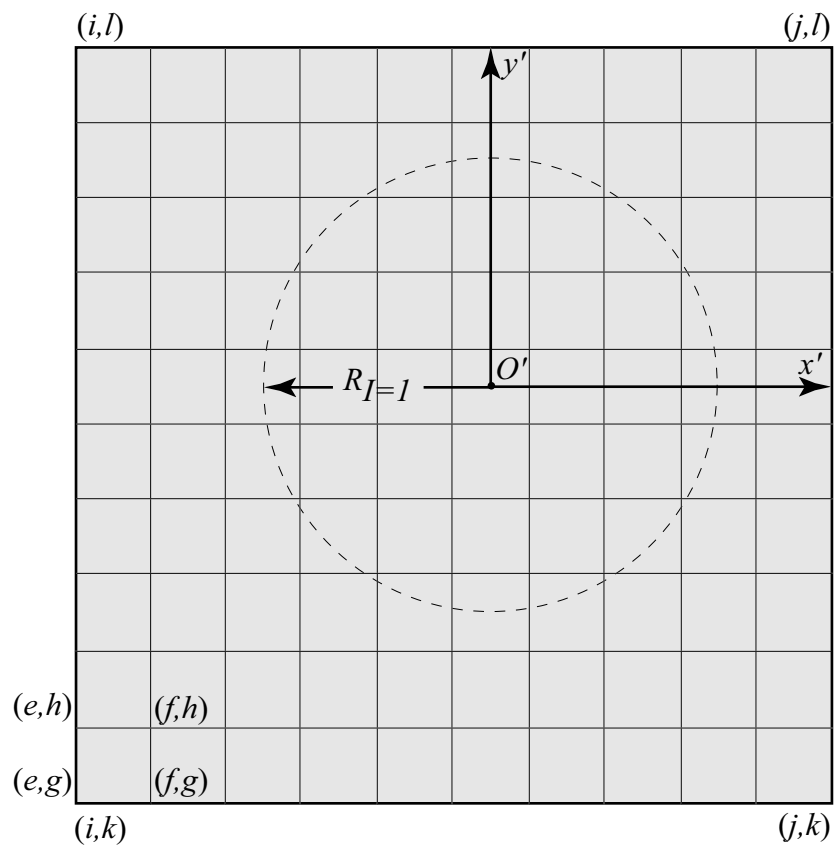
Figure 3.11: *Calculating the average intensity over a pixel. The figure is an enlarged view of the shaded area of Figure 3.10.*

be a rectangular region representing a single pixel in $x'O'y'$ coordinates. The left, right, bottom and top edges of $\mathbf{P}$ in $x'O'y'$ coordinates are respectively e, f, g and h. The edges of $\mathbf{S}$ in xOy coordinates are used to calculate the edges of $\mathbf{P}$ in $x'O'y'$ coordinates. Formula 3.33 is applied to the intensity function Equation 3.23 to get the average value of the intensity over the area of the pixel.

$$\bar{I}(x,y) = \frac{1}{A(\mathbf{P})} \iint\limits_{\mathbf{P}} I\left(x',y'\right) dA \tag{3.36}$$

Substituting for $I(x,y)$ using Equation 3.29,

$$\bar{I}(x',y') = \frac{1}{A(\mathbf{P})} \int_i^j \int_k^l I_0 e^{-\left(x'^2 + y'^2/R^2\right)}. \tag{3.37}$$

$A(\mathbf{P})$ is the area of the pixel. Equation 3.37 evaluates to (see Appendix C)

$$\bar{I}(x',y') = \frac{I_0 R^2 \pi}{4} \left(\operatorname{erf} m - \operatorname{erf} n\right) \left(\operatorname{erf} o - \operatorname{erf} p\right), \tag{3.38}$$

where $m = i/R$, $n = j/R$, $o = k/R$, and $p = l/R$. If I_{ave} is less than 0, it is taken as 0. If it is greater than 255, it taken as 255. I_{ave} is compared with the background intensity already set for the pixel $\mathbf{P}$. Pixel $\mathbf{P}$ is set to the maximum value of the two. Every pixel within the region where the intensity is adjusted has its intensity calculated and set similarly to place the spot representing a particle image.
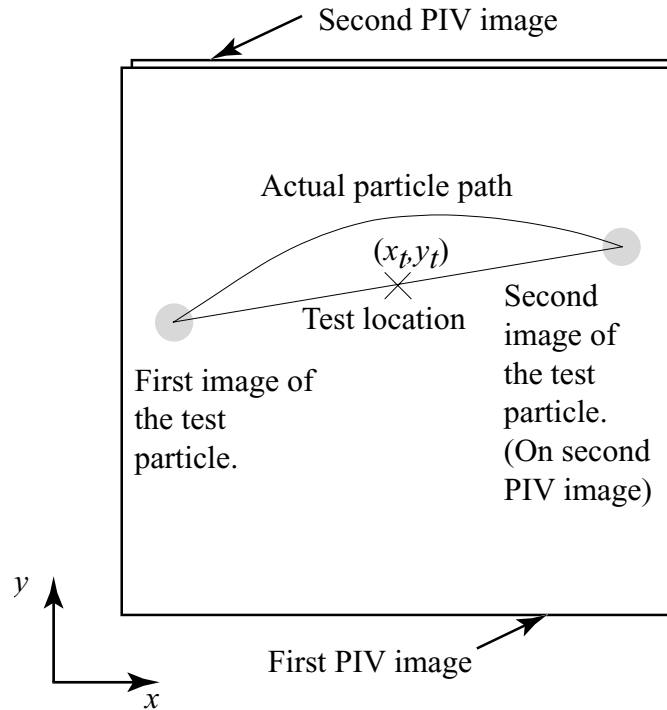
Figure 3.12: *The particle tracking algorithm places the velocity of a particle at the midpoint of the line joining the centroids of its images. In Figure 3.12 an interrogation area on the first image is superimposed on the corresponding area on the second image. The two images of the test particle are also shown. The location midway between the two images of the test particle is the test location (x_t, y_t).*

Placing Particle Images

The PTA places the velocity of a particle at the midpoint of the line joining the centroids (See Section 3.1.3) of the two particles identified as its images. In Figure 3.12 an interrogation area on the first image is superimposed on the corresponding area on the second image. The two images of the test particle are also shown. The location midway between these two images is the *test location* (x_t, y_t).

To use SPIV over a range of fluid velocities, its measurement uncertainty over
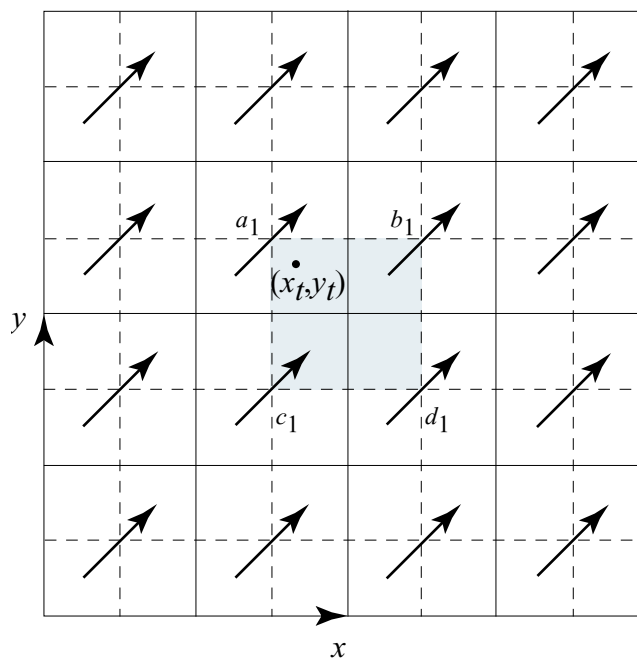
Figure 3.13: *Schematic diagram of the interrogation areas (solid lines) and the interpolation grid (dashed lines).*

this range must be known as a function of the velocity itself. All velocities in this thesis will be expressed in units of pixels/pulse. Therefore, velocity and particle displacement are synonymous. Table 4.2 gives the base case value of $|\Delta \vec{D}|$ along with the range investigated.

Figure 3.13 represents the first PIV photograph. As the first step in placing the images of the test particle, a random test location (x_t, y_t) is chosen inside the interpolation region ($96 \leq x \leq 160$, $96 \leq y \leq 160$). A test location inside the central interpolation region ensures that the velocity at the test location can be interpolated from the corners of the interpolation region during the pair search. It is important that this location be randomly chosen so that statistics based on the ensemble accurately

represent those for real images where the particle locations are random.

Even though the location of the test particle is random, the velocity at the test location must remain constant for all the image pairs in the ensemble. In Equation 3.16a,

$$u = a + by,$$

a is the velocity at the bottom edge of the image. The value of a is calculated from

$$a = u_t - by_t. \tag{3.39}$$

where u_t is the desired u velocity of the test particle and y_t is the randomly chosen position of the test particle. If this value of a is used in Equation 3.16a, the velocity at the test location will remain constant at any desired set point u_t. Once the test location has been obtained, the location of the first image (x_{t1}, y_{t1}) is obtained by substituting $t = -1/2$ in Equations 3.20a and 3.20b:

$$x_{t1} = \frac{cb}{8} + x_t - \frac{1}{2}(a + by_t) \tag{3.40a}$$

$$y_{t1} = y_t - \frac{c}{2} \tag{3.40b}$$

The location of the second image of the test particle (x_{t2}, y_{t2}) is obtained by substi-

tuting $t = 1/2$ in Equations 3.20a and 3.20b:

$$x_{t2} = \frac{cb}{8} + x_t + \frac{1}{2}(a + by_t) \tag{3.41a}$$

$$y_{t2} = y_t + \frac{c}{2} \tag{3.41b}$$

The test particle images are placed at (x_{t1}, y_{t1}) and (x_{t2}, y_{t2}) as explained in Section 3.2.3.

Paired particles are particles which have been illuminated twice. To place the first image of a paired particle a random location (x_1, y_1) is generated inside the first photograph (see Section 3.2.3). The location of the second image x_2, y_2 is obtained by substituting $t = 1$ in Equations 3.19a and 3.19b. The images are placed at $x_1, y1$ and x_2, y_2 as explained in Section 3.2.3.

A specified number of spurious particles are placed on each photograph at random locations. Spurious particles may be present on a PIV photograph due to an out-of-plane velocity component. An out-of-plane component may carry particles which were in the light sheet during the first pulse of the laser out of it by the time the laser pulses a second time. The first image of such particles will have no pair image corresponding to the second pulse. The reverse may also occur. Large numbers of spurious particles can cause inaccurate tracking. Therefore, the number of spurious particles N_s was a parameter studied in this thesis. To place a spurious particle on a photograph a random location (x_s, y_s) is obtained as described in Section 3.2.3 and a particle image is placed at (x_s, y_s) as described in Section 3.2.3. Figure 3.14 shows the first and second artificial PIV images. The images have been generated with all

70

(a)

(b)
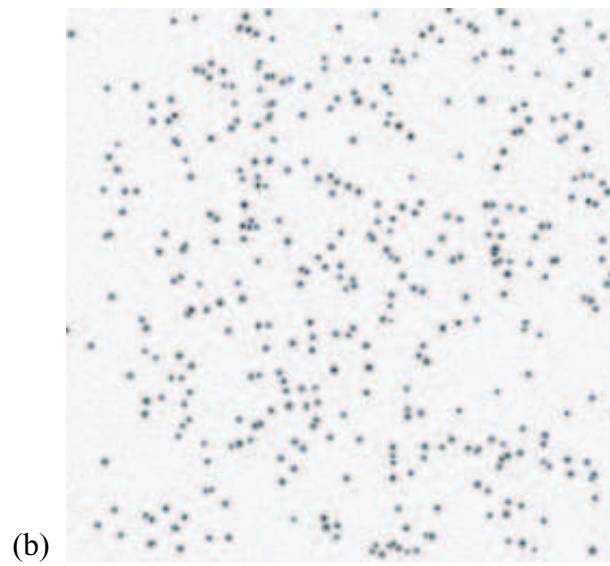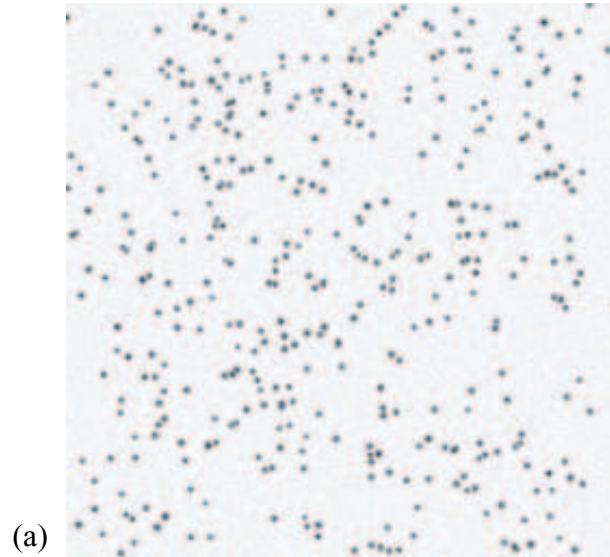
Figure 3.14: *(a) First artificial PIV image. (b) Second artificial PIV image. All parameters are at default values. The greyscale has been inverted for clarity.*

parameters set to the default values.

3.3   Measurement of Uncertainty

Section 3.1 described the particle tracking algorithm. Section 2.6 explained measurement uncertainty. Section 3.2 described the generation of artificial dual-frame PIV images. A sample of measurements of the measured variable is required to calculate the measurement uncertainty. The measured variable in this thesis is the error in the velocity measurement. Therefore, a sample of velocity measurement errors is needed. This section describes the procedure for sampling the measurement error.

3.3.1   Overview of the Procedure

The procedure for obtaining a single measurement of the error is outlined in this section. It is repeated to obtain a sample of size n_e, the sample size. As explained in Section 3.2.3, artificial PIV images include the images of a test particle of known velocity. If the test pair is correctly identified by the PTA the velocity of the test particle can be measured. The measurement error is the difference between the known velocity of the test particle and its measured velocity. Since velocity is a vector, the error in measurement can be in the magnitude or the direction. The *magnitude error* is the difference between the magnitude of the exact velocity and the magnitude of the measured velocity. The *direction error* is the difference between the direction of the exact velocity and the direction of the measured velocity.

72

3.3.2 Identifying the Test Particle

During the pair search (Section 3.1.3) each pair found is added to a list of pairs. The locations of the members of a pair uniquely identify the pair. One way to identify the test particle is to see if the known exact locations of the test particle images exist as a pair in the list of pairs. However, this approach may not succeed in detecting the test particle because the exact locations of the images of the test particle need not match with the locations of any of the pairs in the list. There can be several reasons for this. The choice of the threshold intensity for segmentation can result in the exclusion of pixels of a test particle image. Inclusion of background pixels in the image can also occur. As the particle image location is calculated as the intensity barycentre (Section 3.1.2), pixel inclusion or exclusion will change the calculated location. If there are particle images overlapping, the test particle image location will be that of the composite spot. For these reasons the following rule is used to determine which pair in the list, if any, represents the test particle.

Rule for Identifying the Test Particle

Consider the first image of a pair. The location (Section 3.1.2) of each identified particle is stored during particle identification. The distance between the known exact location of the first image and the location of each identified particle is calculated. The particle closest to the exact location is taken as the test particle. The same procedure is used to identify the test particle on the second image. These two are the test pair. If they exist as a pair in the list of pairs the algorithm has been successful in finding the test particle and will proceed to calculating the measurement error.

3.3.3   Exact and Measured Velocities

Exact Velocity of Test Particle

The exact velocity $\mathbf{V_t}$ of the test particle is an input parameter to the algorithm which generates the artificial PIV images. The base case velocity is the exact velocity $\mathbf{V_t}$ of the test particle when investigating the effect of all parameters other than the velocity magnitude and the velocity direction. The base case x and y components of the velocity of the test particle are $u_t = 8$ pixels/pulse and $v_t = 2$ pixels/pulse. The magnitude of the base case test particle velocity is (see Table 4.2)

$$V_t = \sqrt{u_t^2 + v_t^2} = \sqrt{8^2 + 2^2} = 8.246 \text{ pixels/pulse.} \tag{3.42}$$

The direction of the base case test particle velocity is

$$\theta_t = \tan^{-1}\left(\frac{v_t}{u_t}\right) = \tan^{-1}\left(\frac{2}{8}\right) = 14.03 \text{ degrees.} \tag{3.43}$$

The velocity at the test particle location (x_t, y_t) is set to any desired value as follows. The velocity field for the simulated images is given by Equations 3.16a and 3.16b. Since for this study the velocity gradient $d = \partial v/\partial x = 0$, the velocity field is

$$u = a + by. \tag{3.44a}$$

$$v = c. \tag{3.44b}$$

To set a velocity u_t at the test location, the value of the constant a is calculated from Equation 3.39. Substituting this value of a in Equation 3.44a gives the x component of the test particle velocity at the test location as

$$u = (u_t - by_t) + by_t = u_t. \tag{3.45}$$

At all locations in the flow velocity field the vertical component of the velocity is constant at a value of c pixels/pulse. The vertical component of the velocity at the location of the test particle is $v_t = c$ pixels/pulse. For the base case $c = 2$.

When the velocity magnitude is the varied parameter, the velocity direction, which is also a parameter under study, should remain at the base case value of $14.03°$. Let u_d be any desired velocity magnitude at the test particle location. Then the horizontal and vertical components of the velocity of the test particle, u_t and v_t, are calculated as

$$u_t = u_d \cos 14.03 \quad \text{and} \tag{3.46a}$$

$$v_t = u_d \sin 14.03. \tag{3.46b}$$

When the velocity direction is the varied parameter, the velocity magnitude should remain at the base case value of 8.246 pixels/pulse. Let θ_d be any desired velocity direction at the test particle location. Then the horizontal and vertical components

of the velocity of the test particle, u_t and v_t, are calculated as

$$u_t = 8.246 \cos \theta_d \quad \text{and} \tag{3.47a}$$

$$v_t = 8.346 \sin \theta_d. \tag{3.47b}$$

Measured Velocity of the Test Particle

The measured displacements are calculated from the locations of the pair identified as the test pair by the PTA (Section 3.3.2). Let (x_{m1}, y_{m1}) and (x_{m2}, y_{m2}) be the locations of the first and second test particle images. The component in the direction of the unit vector $\mathbf{i}$ of the displacement in one pulse of the laser is

$$\Delta x_m = x_{m2} - x_{m1}. \tag{3.48}$$

The component in the direction of the unit vector $\mathbf{j}$ of the displacement in one pulse of the laser is

$$\Delta y_m = y_{m2} - y_{m1}. \tag{3.49}$$

Equation 3.48 is the measured x component of the velocity u_m in pixels/pulse. Equation 3.49 is the measured y component of the velocity v_m. The measured velocity of the test particle is

$$\mathbf{V_m} = u_m \mathbf{i} + v_m \mathbf{j}. \tag{3.50}$$

The magnitude of the measured velocity is

$$V_m = \sqrt{u_m^2 + v_m^2} \qquad (3.51)$$

and the direction is

$$\theta_m = \tan^{-1}\left(\frac{v_m}{u_m}\right). \qquad (3.52)$$

3.3.4 Velocity Measurement Error

The magnitude error δ_V is the difference between the magnitudes of the measured and exact velocities.

$$\delta_V = V_m - V_t. \qquad (3.53)$$

The direction error δ_θ is the difference between the directions of the measured and exact velocities.

$$\delta_\theta = \theta_m - \theta_t. \qquad (3.54)$$

3.3.5 The Sample Size

Equations 3.53 and 3.54 give the magnitude and direction errors. For either, the measurement uncertainty is calculated using Equation 2.36. To calculate the systematic uncertainty B and the random uncertainty P in Equation 2.36, a sample of measurement errors is generated at each level of the input parameters. PIV images are generated and analysed until a sample of size n_e is obtained. The sample size
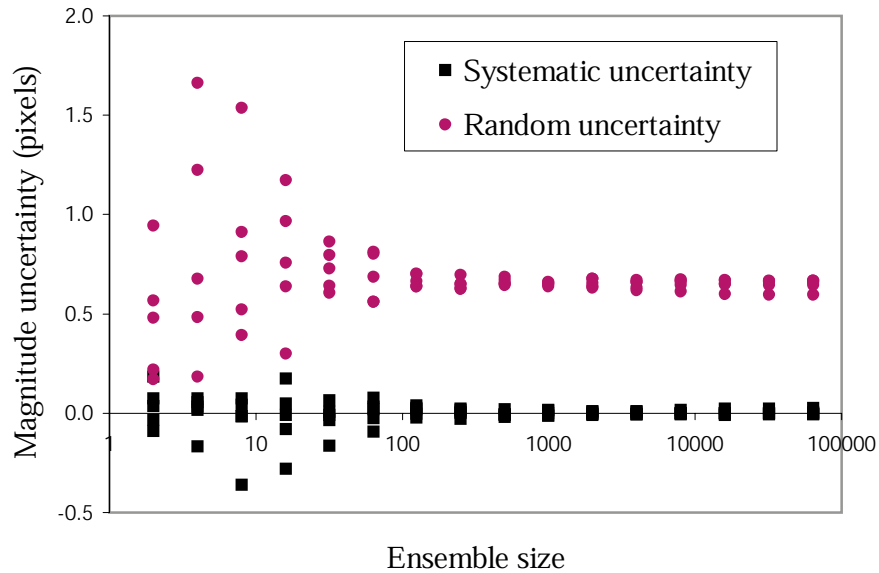
Figure 3.15: *Ensemble size versus velocity magnitude uncertainty with all parameters at base case values.*

should be large enough to yield converged statistics. That is, any statistic calculated from a sample of size n_e should yield essentially the same value for any sample of that size. To determine n_e, five samples were generated with all parameters at the base case values (Table 4.2, p. 82). This was done for sample sizes ranging from 2 to 64000. The systematic uncertainty and the random uncertainty in the velocity magnitude were calculated for all five samples at each sample size. Figure 3.15 shows the results. Appreciable scatter is noticeable in the uncertainties at small ensemble sizes. At an ensemble size of one thousand the uncertainties have both converged. Based upon this result, an ensemble size of 4000 was selected.

3.3.6 Success Rate

In order to generate a sample of measurement errors of size n_e, the simulation program may have to analyse more than n_e pairs of PIV images. This is because the test particle might not be identified for all pairs of PIV images. If the test particle is not identified for a pair of PIV images, a measurement of the test particle velocity, and consequently the measurement error are not available for that image pair. Let n_a be the number of PIV image pairs analysed to obtain a sample of n_e measurement errors. The *success rate* is defined as

$$\text{Success rate} = \frac{n_e}{n_a}.$$

(3.55)

Chapter 4

Results and Discussion

In this thesis, the effects of nine parameters on the success rate and the uncertainty in velocity measurement of a particle tracking algorithm were examined. The systematic and random uncertainties in velocity magnitude and direction are presented separately to facilitate a comparison of their relative magnitudes. This chapter presents the results of the study.

4.1   Fixed Parameters

To reduce the complexity of the study, four parameters were assigned fixed values. They are the mean diameter of the particles μ_D, the standard deviation of the particle diameters σ_D, the standard deviation of the particle central intensities σ_{I_0}, and the standard deviation of the background pixel intensities σ_{I_b}. Table 4.1 lists the fixed parameters and their values.

Table 4.1: *Fixed parameters in the uncertainty analysis of the particle tracking algorithm.*

Fixed Parameter	Value
μ_D	3 pixels
σ_D	0.25 pixels
σ_{I_b}	5
σ_{I_0}	20

In addition, recall that this study focuses on the particle tracking algorithm (PTA) of the super-resolution PIV technique. Therefore, the velocity field available to the PTA, which would normally be produced by a cross-correlation PIV algorithm, is assumed to be exact.

4.2 Dependent and Independent Variables

This study considers five dependent variables, the success rate, the systematic uncertainty in the velocity magnitude, the random uncertainty in the velocity magnitude, the systematic uncertainty in the velocity direction, and the random uncertainty in the velocity direction. Each of these are studied as functions of nine parameters or independent variables. These nine parameters can be divided into three categories, four that are related to image quality (the number of paired particles N_p, the number of spurious particles N_s, the mean particle intensity μ_{I_0}, and the mean background intensity μ_{I_b}), two that are related to PTA settings (the segmentation threshold intensity I_t and the search radius r_s), and three that are related to the velocity field (the velocity direction θ, the velocity magnitude V in pixels per pulse, and the velocity

Table 4.2: *Base case and range of the nine independent variables (parameters) studied.*

Parameter	Minimum	Base case	Maximum
N_s (-)	0	10	40
N_p (-)	10	20	150
μ_{I_0} (-)	90	200	250
μ_{I_b} (-)	90	120	150
I_t (-)	20	80	180
r_s (pixels)	0.1	2	4
θ (degrees)	0	14.03	45
V (pixels)	4	8.246	16
$\partial u/\partial y$(1/pulse)	0	0.05	0.25

gradient $\partial u/\partial y$). Table 4.2 shows the minimum value, base case value, and maximum value of the nine independent variables (parameters). The effect of a parameter on a dependent variable was studied by varying its value from the minimum to the maximum value while holding all other parameters constant at their base case values.

Before studying the influence of each of these parameters, the performance of the base case must be established. Table 4.3 shows the success rate and uncertainties achieved with the base case parameter settings. At the base case settings, the systematic uncertainties are clearly very low compared to the random uncertainties and the success rate is very high. It is clear that the algorithm performs quite well under these rather favourable conditions. The remainder of this chapter will investigate how changes in the parameters can degrade the PTA algorithm performance from those established for the base case.

Table 4.3: *PTA performance for the case when all parameters are at their base case values.*

Dependent Variable	Base Case Value
Success Rate	98.5%
Magnitude Systematic Uncertainty	0.0090 pixels
Magnitude Random Uncertainty	0.56 pixels
Direction Systematic Uncertainty	0.019 degrees
Direction Random Uncertainty	4.0 degrees

4.3 Effect of the Number of Paired Particles

Figure 4.1a shows the effect of the number of paired particles N_p on the success rate. The success rate is 0.98 for 10 pairs/interrogation area and drops to 0.83 when N_p increases to 150. However, more pairs will be identified when the success rate is 0.83 and $N_p = 150$ than when the success rate is 0.98 and $N_p = 10$. The spatial resolution is ultimately determined by the number of image pairs that can be successfully identified. Since the correlation stage of the algorithm produces one measurement of velocity per interrogation area, any number of pairs greater than this identified by the PTA will increase the resolution. The spatial resolution has thus increased at $N_p = 150$ even though the success rate has fallen. It must be remembered that this study does not consider uncertainties in the correlation algorithm. At high particle loads, the uncertainty in the correlation algorithm will increase. A coupled uncertainty analysis of the correlation stage and the tracking stage would be valuable to determine the point at which the increased uncertainty in the correlation stage overcomes the benefit of the increased resolution provided by the tracking stage. This

study indicates that even when the image density is increased well beyond that normally recommended for PIV, good pair identification (i.e. increased resolution) is possible.

When N_p increases, the particle image density increases. Image density is the concentration of particle images per unit area on a PIV image. Increased image density can result in composite particle images. These are images of proximate particles overlapping to form a single particle image. If one or both of the test particle images are involved, their apparent locations (intensity barycentres) will be shifted significantly. A shift in the location of the test particle images can potentially bring other particle images closer to the expected location of the test particle on the second PIV image. This will affect which particle image on the second PIV image gets selected as the pair to the test particle. If the wrong particle gets selected, the success rate will drop.

Particle image overlap can also shift the locations of particles which would have been inside the search radius, outside of it. In this case, the search for the test pair will fail because no pair can be found. This will also decrease the success rate.

The effect of the number of pairs on the magnitude uncertainty is shown in Figure 4.1b. The systematic uncertainty in magnitude is negligible over the range of values of N_p. The random uncertainty is dominant and increases as N_p increases. The direction uncertainty, plotted on the second axis in Figure 4.1, shows a similar pattern. The systematic uncertainty is negligible, while the random uncertainty exhibits an almost linear increase as N_p is increased. These results can also be explained by the increasing likelihood of particle image overlap as N_p increases. Because the positions

84
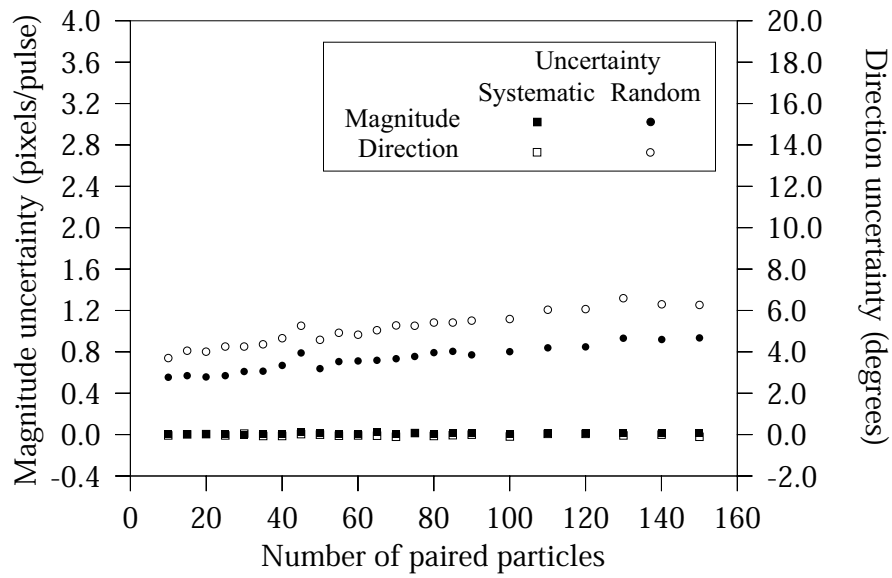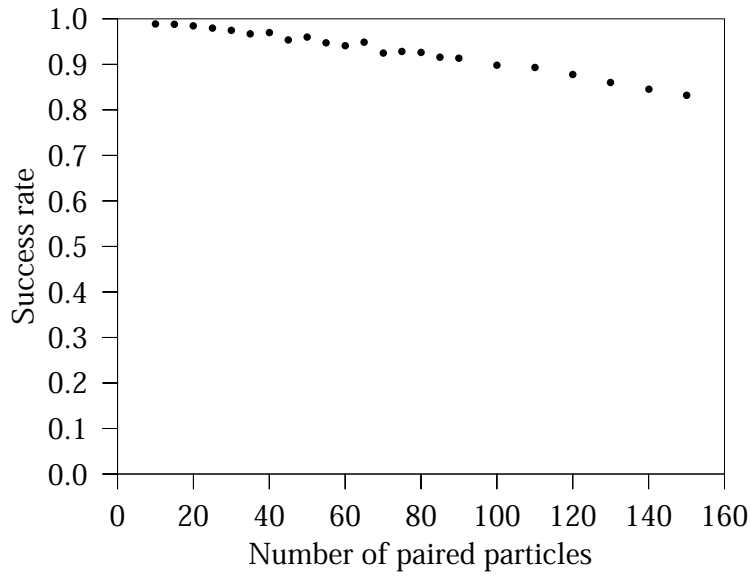
Figure 4.1: *(a) Effect of the number of pairs on the success rate. (b) Effect of the number of pairs on the magnitude and direction uncertainties.*

of the particle images are random, no systematic uncertainty is introduced.

4.4   Effect of Spurious Particles

Increasing the number of spurious particles N_s also increases the image density. The mechanisms that are active when N_p is increased will be active in this case also. Images of spurious particles can overlap with images of other particles. If particle image overlap shifts the location of the test particle, spurious particles can be closer to the trial location within the search radius. Overlap with a spurious particle may carry the centroid of the pair beyond the search radius. If there are no other particles within the search radius, no pair will be identified. This too would lead to a reduced success rate.

A spurious particle can get identified as the first test particle image if it is closer to the actual location of the first test particle image. This may occur if overlap has shifted the image of the test particle. As the spurious particle does not have a pair, it is possible that no particle will be detected within the search radius during the pair search procedure. The search will then fail. The behavior of the success rate and the uncertainties is similar to that when N_p is increased. The success rate, shown in Figure 4.2a, exhibits a small linear decrease. The systematic uncertainties in the velocity magnitude and velocity direction, shown in Figure 4.2b, are both negligible. The random uncertainties dominate, and they increase almost linearly with increasing N_s, as shown in Figure 4.2b.
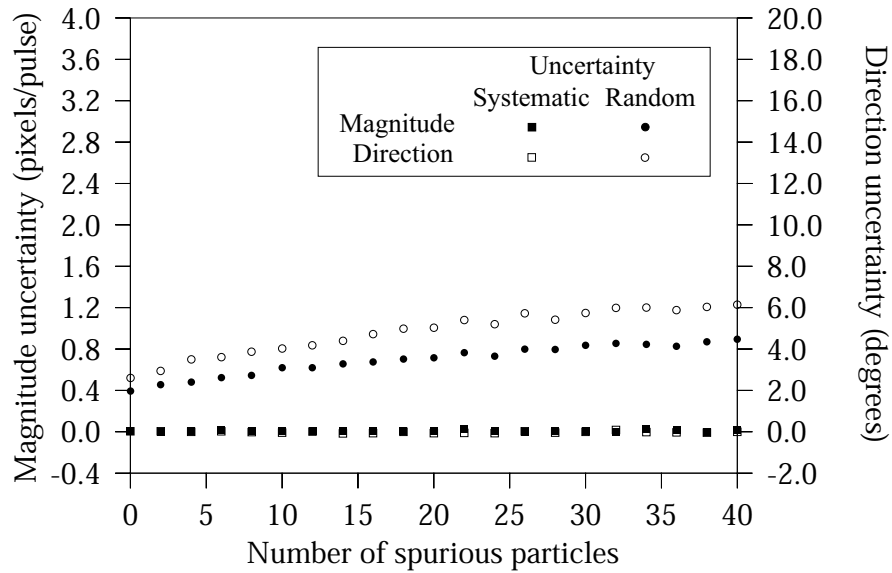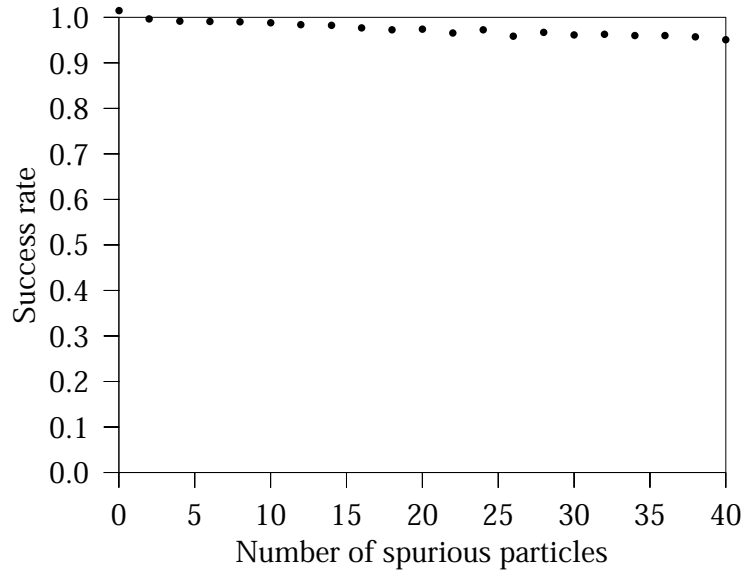
Figure 4.2: *(a) Effect of the number of spurious particles on the success rate. (b) Effect of the number of spurious particles on the magnitude and direction uncertainties.*

4.5 Effect of the Mean Particle Central Intensity

Figure 4.3a shows the effect of the mean particle intensity μ_{I_0} on the success rate. The success rate increases sharply from 0.28 when I_0 is 90 to 0.98 when I_0 is 150 and remains constant for $I_0 > 150$. The base value of the mean background intensity μ_{I_b} is 10. The standard deviation of the mean background intensity σ_{I_b} is fixed at 5. At these values there is little noise present above the base case segmentation threshold I_t of 80. The increase in success rate with μ_{I_0} is due to better visibility of the particles above the segmentation threshold. The standard deviation of the particle intensity distribution σ_{I_0} is 20. When the mean particle intensity μ_{I_0} is 100, the probability that I_0 of both test particle images is greater than or equal to 80 is 0.71. This is considerably higher than the success rate for $I_0 = 100$ which is about 0.47. However, it must be remembered that no pixels making up the particle image will have intensities as high as I_0 since the actual intensity assigned to a pixel constituting the particle image is calculated by integrating the Gaussian intensity distribution over the area of the pixel. Because the particles are quite small ($\mu_D = 3$, $\sigma_D = 0.25$) actual pixel intensities will be considerably less than I_0. The higher the mean particle central intensity, the higher the probability that the test particle images are above the threshold, and the higher their chances of being identified. An increase in the success rate with increasing μ_{I_0} is expected.

Figure 4.3b shows that systematic uncertainty in magnitude is present only at mean particle intensities near the threshold. The systematic uncertainty in the direction is negligible. The random uncertainties are high when the mean particle
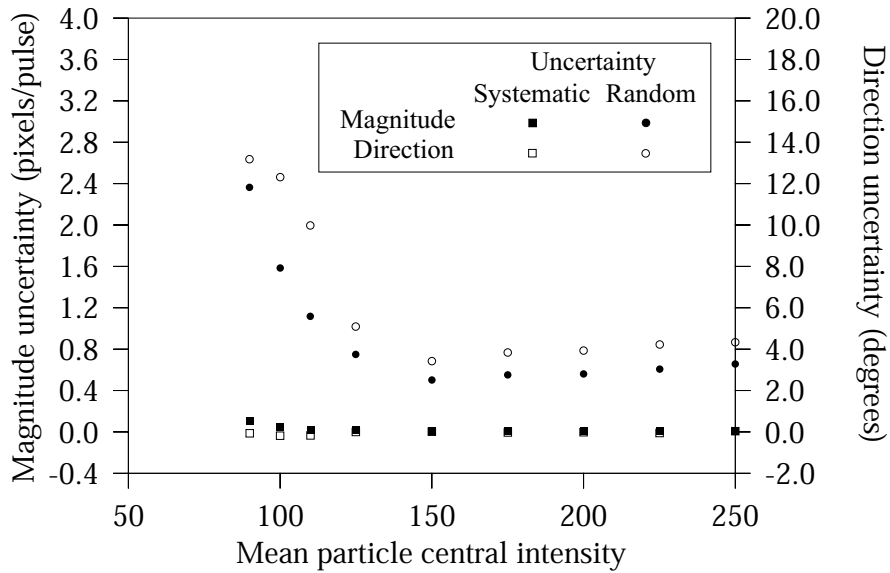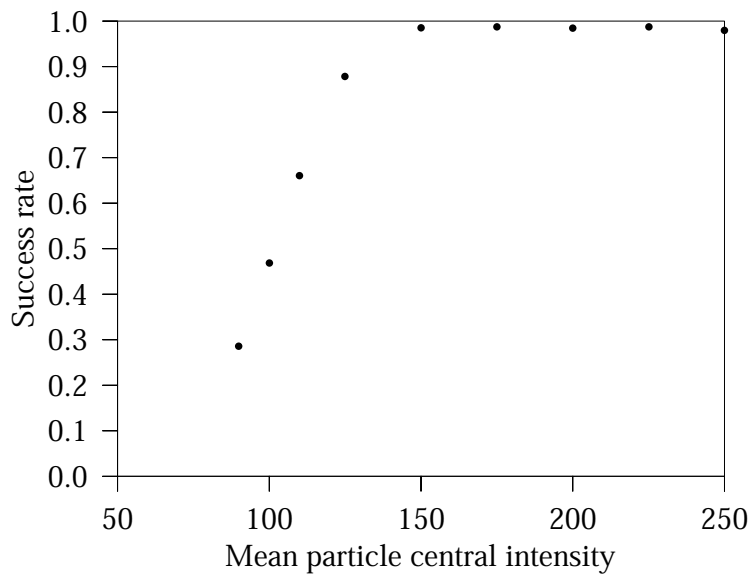
Figure 4.3: *(a) Effect of the mean particle central intensity on the success rate. (b) Effect of the mean particle central intensity on the magnitude and direction uncertainties.*

intensities are near the segmentation threshold. The random uncertainty in magnitude is 2.36 pixels when μ_{I_0} is 90. It falls to 0.49 when μ_{I_0} is 150 and thereafter shows only a slight increase. The random uncertainty in the direction is 13.17 when μ_{I_0} is 90, falls to 3.43 when μ_{I_0} is 150, and thereafter shows only a slight increase. When the particle intensity is near the threshold, the particle will be represented by very few pixels and the uncertainty in its location will increase.

4.6   Effect of the Mean Background Intensity

Figure 4.4a shows the effect of the mean background intensity μ_{I_b} on the success rate. The success rate is constant at 0.98 as the mean background intensity increases from zero to 60. The success rate begins to decrease when μ_{I_b} is 70, and falls abruptly when μ_{I_b} equals 80. This behavior can be explained as follows. The particle tracking algorithm considers noise above the threshold to be particles. Since the PTA cannot distinguish between noise above the threshold and particles, significant noise above the segmentation threshold will degrade its performance. This explains the sharp drop in the success rate as μ_{I_b} increases to 80.

The standard deviation of the mean background intensity is fixed at $\sigma_{I_b} = 5$. The probability that I_b exceeds the base case threshold intensity of 80 when μ_{I_b} is 70 is 0.022. This probability is 0.15 when μ_{I_b} is 75, and 0.5 when μ_{I_b} is 80. Noise begins to appear above the segmentation threshold when μ_{I_b} is 70, increases when μ_{I_b} is 75, and becomes significant when μ_{I_b} is 80.

Figure 4.4b shows the effect of the mean background intensity on the magnitude

and velocity uncertainties. The random uncertainty in magnitude is almost constant at a value of 0.59 pixels until μ_{I_b} is 70, becomes 0.80 when μ_{I_b} is 75 and increases sharply to 1.79 as μ_{I_b} increases to 80. The direction uncertainty is 4.17 pixels when μ_{I_b} is 70, 5.44 pixels when μ_{I_b} is 75 and increases sharply to 12.18 pixels when μ_{I_b} is 80. The mean background noise is an important parameter because it sets limits on possible values of the threshold intensity. A high mean background noise forces the use of a high value of the threshold. When the intensity of the background noise reaches that of particle pixels, the threshold value needed to exclude background noise will begin to exclude particles. This degrades the ability of the PTA to identify and correctly locate particles and results in lower success rates and higher uncertainties.

4.7   Effect of the Threshold Intensity

The threshold intensity I_t is a parameter of the particle tracking algorithm. The effect of the threshold value on the success rate is shown in Figure 4.5a. The success rate is 0.85 when I_t is 20. The success rate increases to 0.99 when I_t increases to 100, is 0.98 when I_t is 120, and falls sharply thereafter to 0.23 when I_t increases to 180. The initial increase in the success rate is due to the progressive exclusion of background noise having intensities greater than the threshold value. When all background noise has been excluded the success rate is steady until I_t is 120. The drop in success rate when the threshold is increased further is due to the exclusion of particle pixels. The dramatic drop in the success rate as the threshold approaches 180, close to the base value of the mean particle intensity of 200, strongly indicates this.

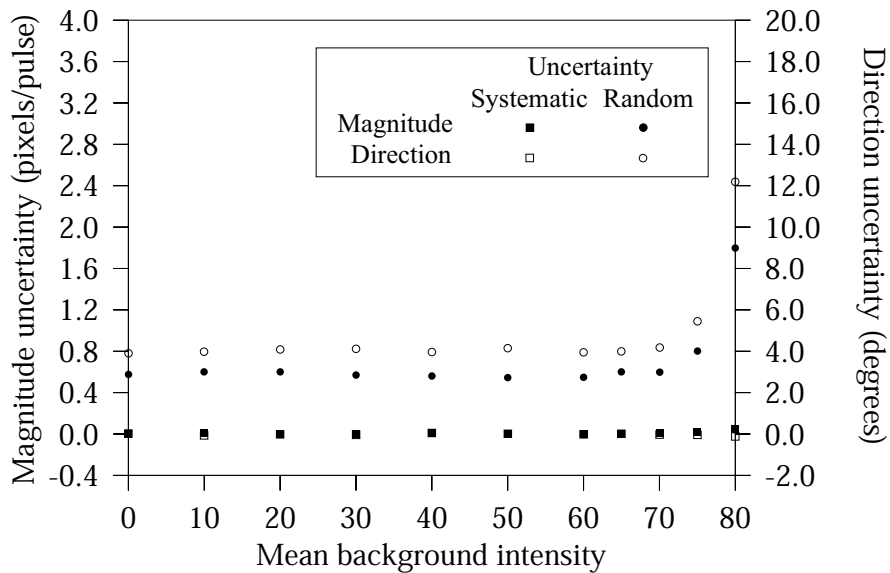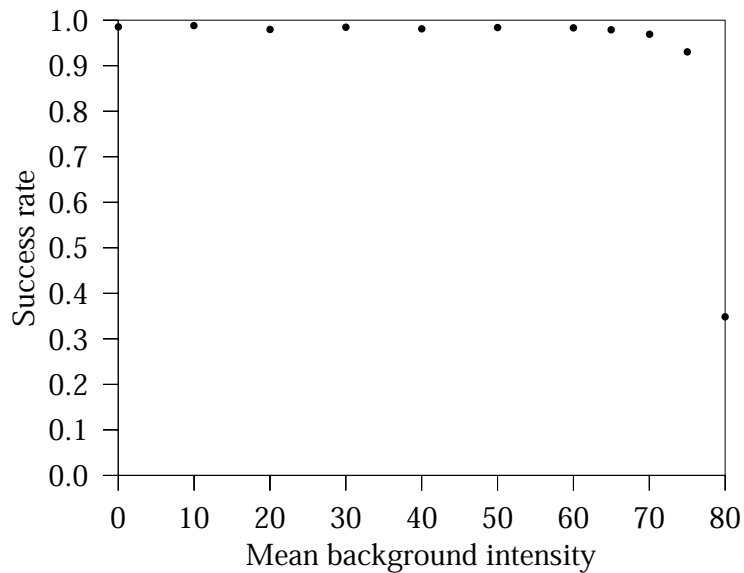**Figure 4.4:** *(a) Effect of the mean background intensity on the success rate. (b) Effect of the mean background intensity on the magnitude and direction uncertainties.*
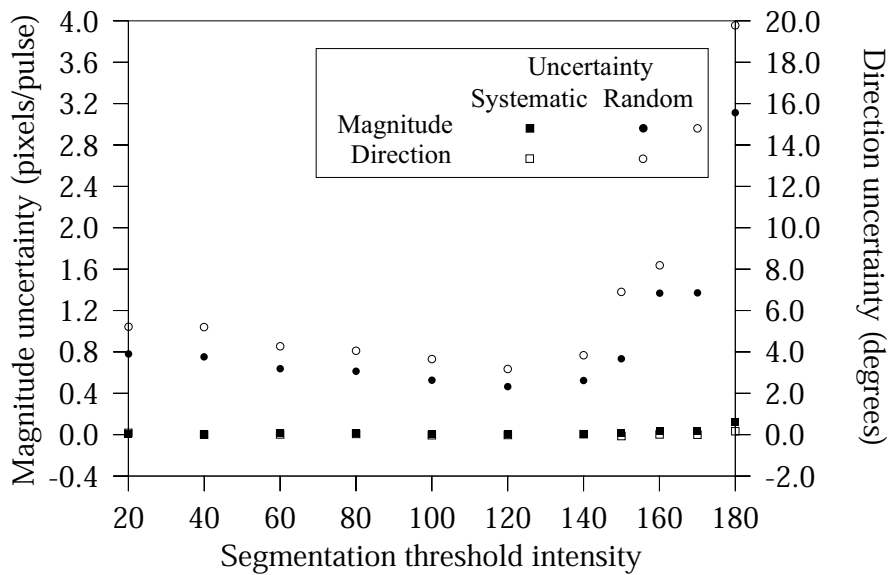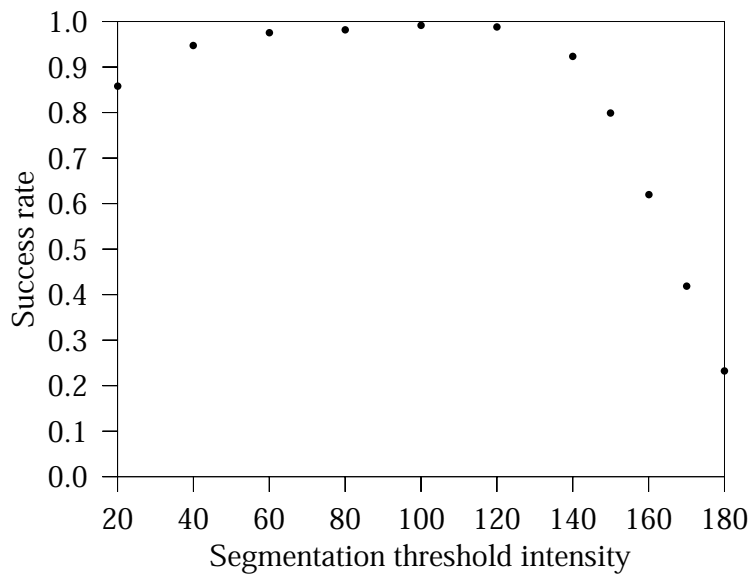
Figure 4.5: *(a) Effect of the threshold intensity on the success rate. (b) Effect of the threshold intensity on the magnitude and direction uncertainties.*

The choice of threshold affects the particle tracking algorithm as follows. If the threshold value is set close to the mean background intensity, the PTA identifies some background noise pixels as particles. This will degrade the performance of the PTA. If the *contrast* is low the threshold value must be close to the mean particle intensity to exclude background noise. This will result in the exclusion of some particle pixels and degrade the performance of the tracking algorithm. Contrast is the amount of greyscale differentiation between features on an image. There are many metrics of contrast. The Weber contrast, the Michelson contrast, the root-mean-square contrast, and local band-limited contrast are some [28]. In this discussion, contrast can be characterised by the difference between the mean particle central intensity and the mean background intensity $(\mu_{I_0} - \mu_{I_b})$. When the contrast is high, a low threshold value can be used. This increases the success rate since more particles are accurately located. The effect of the difference between the mean particle intensity and the threshold value $(\mu_{I_0} - I_t)$ on the success rate is shown in Figure4.7. As long as the mean background intensity μ_{I_b} is low, it makes little difference whether $\mu_{I_b} - I_t$ is varied by fixing the mean background intensity or by fixing the threshold value. This suggests that it is the difference $\mu_{I_b} - I_t$ which is important, and not the absolute values of either μ_{I_b} or I_t.

The effect of the threshold intensity on the magnitude and direction uncertainties is shown in Figure 4.5b. The systematic uncertainties of the velocity magnitude and direction are negligible. The random uncertainty is preponderant in both cases. The random uncertainties in both magnitude and direction decrease where the success rate increases. This can be attributed to accurate identification and location of the test
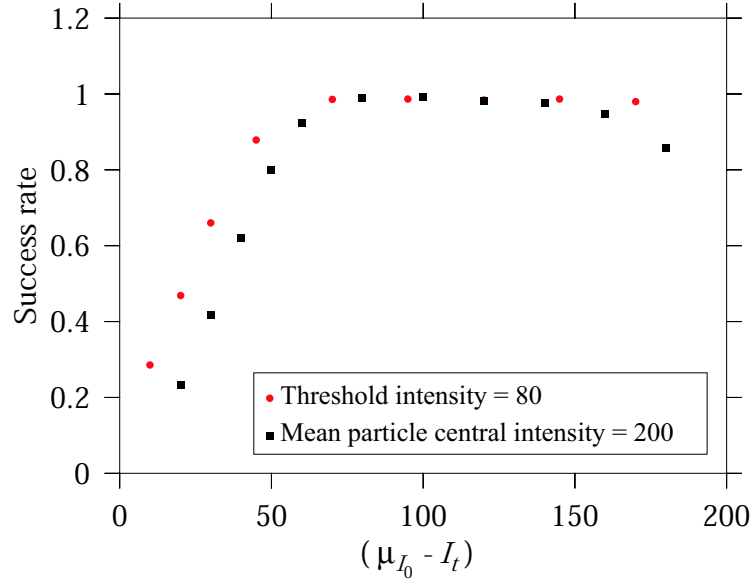
Figure 4.6: *Effect of $\mu_{I_b} - I_t$.*

pair due to exclusion of background noise. Subsequently, the random uncertainties increase where the success rate decreases. The exclusion of particle pixels, the cause of the decreased success rate in this range, is the possible reason for the increased uncertainty.

4.8   Effect of the Search Radius

The search radius r_s is a parameter of the particle tracking algorithm. The effect of the search radius on the success rate is shown in Figure 4.7a. The success rate is 0.97 when the search radius is four pixels. It is constant at a value close to 0.99 as the search radius decreases to two pixels. The success rate decreases thereafter. It begins to drops sharply at a search radius of 0.5 and is 0.39 when the search radius is 0.1

pixels.

This behavior can be explained as follows. During the pair search procedure, the particle closest to the estimated location of the second particle image is selected to form the pair. A very small search radius may exclude all particle images near the estimated location and will decrease the success rate. In fact, the success rate must approach zero as the search radius approaches zero. Increasing the search radius increases the success rate since the chances of finding the correct particle image inside the search circle increases.

The effect of the search radius on the magnitude and direction uncertainties is shown in Figure 4.7b. The systematic uncertainty in the velocity magnitude is negligible although some uncertainty is present at higher values of the search radius. The systematic uncertainty in the velocity direction is negligible. The random uncertainty in magnitude is 0.08 pixels when r_s is 0.1 pixels. It increases to 0.62 pixels when r_s is four pixels. The random uncertainty in direction is 0.46 degrees when the search radius is 0.1 pixels. It increases to 4.60 degrees when r_s is four pixels.

The smaller random uncertainties at lower values of the search radius can be explained as follows. The range of possible error measurements is limited by the search radius since particle locations which fall outside of the search radius will never be identified as pairs. Since the range of possible error measurements is restricted at small search radii, the standard deviation is also reduced. Increasing the search radius increases the success rate, but also increases the uncertainty.
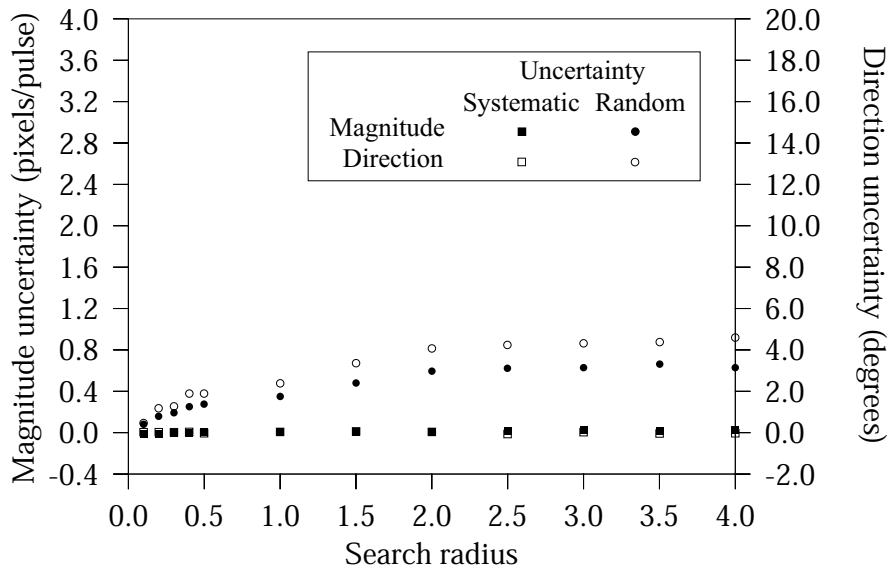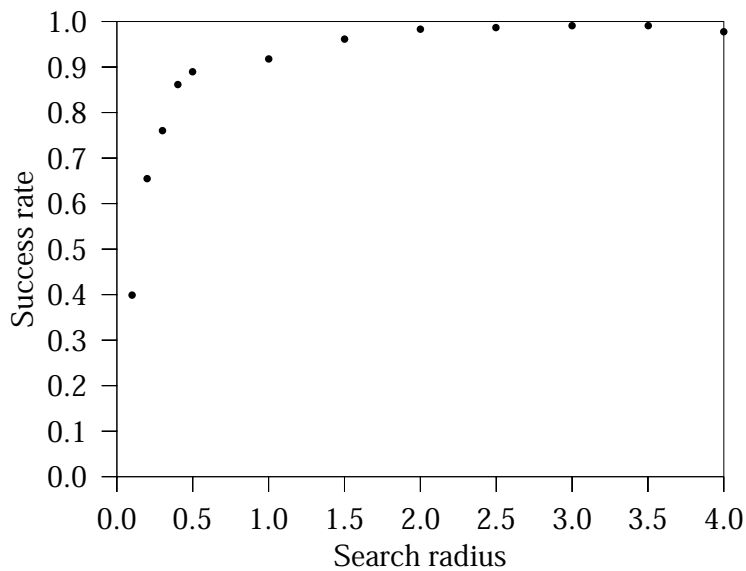
Figure 4.7: *(a) Effect of the search radius on the success rate. (b) Effect of the search radius on the magnitude and direction uncertainties.*

4.9 Effect of the Velocity Gradient

The effect of the velocity gradient $\partial u/\partial y$ on the success rate is shown in Figure 4.8a. The velocity gradient does not have much effect on the success rate. The success rate is almost constant at 0.98 as the velocity gradient increases from zero to 0.25. The velocity interpolation from the coarse grid PIV results to the location of the first particle image during the pair search is exact for the velocity field investigated in this thesis (see Section 3.1.3). Since the interpolation is exact and independent of the velocity gradient, the success rate will not be influenced by the velocity gradient. The effect of the velocity gradient on the uncertainties in velocity magnitude and direction is shown in Figure 4.8b. The systematic uncertainties in magnitude and direction are both negligible. The random uncertainties in magnitude and direction do not seem to be affected much by the velocity gradient. The velocity gradient might have a significant effect on the success rate and uncertainties if real PIV coarse grid results are used. This has not been investigated.

4.10 Effect of the Velocity Magnitude

The influence of velocity magnitude was investigated by varying the velocity magnitude V as the angle of the velocity vector was held constant. The effect of the velocity magnitude on the success rate is shown in Figure 4.9a. The success rate is almost constant at 0.98 as V decreases from 16 to four. The effect of the velocity magnitude on the uncertainties in the velocity magnitude and direction is shown in Figure 4.9b. The systematic uncertainties in the magnitude and direction are negligi-
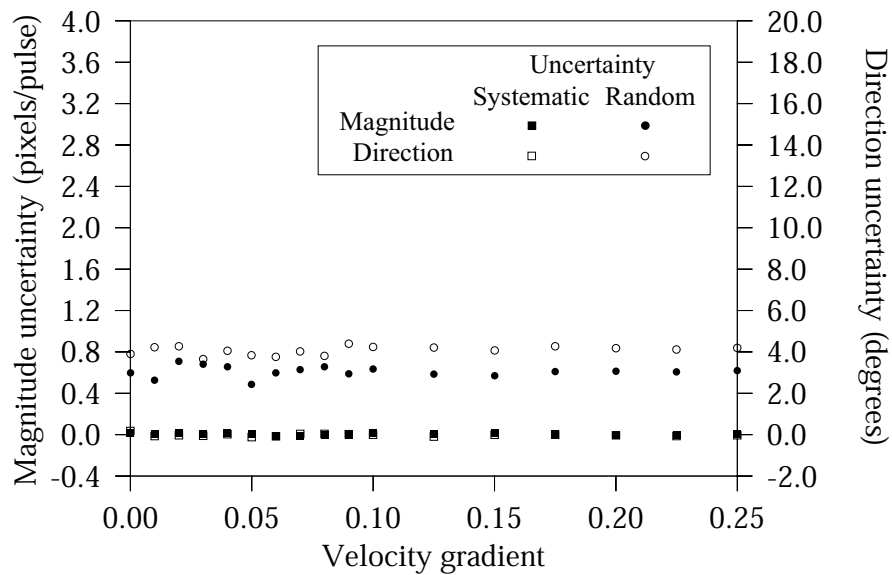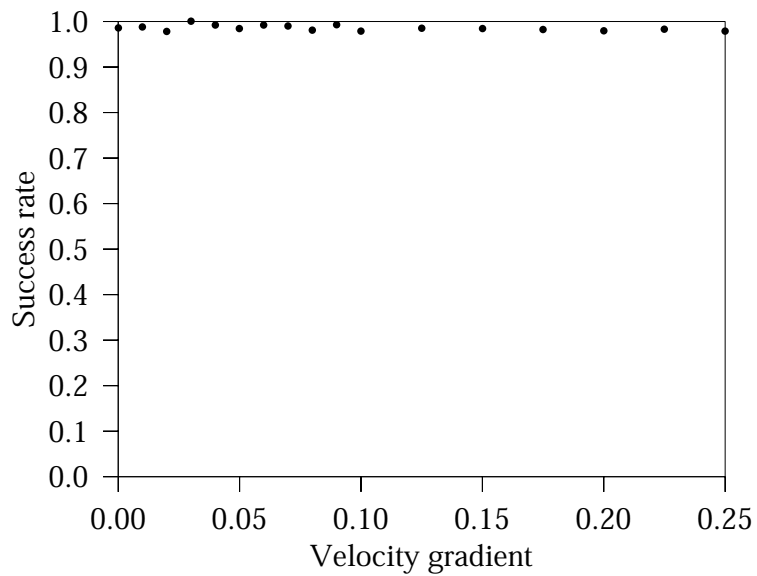
Figure 4.8: *(a) Effect of the velocity gradient on the success rate. (b) Effect of the velocity gradient on the magnitude and direction uncertainties.*

ble. The random uncertainty in the magnitude remains constant as V decreases from 16 to four. There is a steady increase in the random uncertainty in the direction as V decreases. This is probably an effect of equation 3.52 used to calculate the direction of the measured velocity. At smaller displacements, shifts in the locations of the test particle images result in large variations of the velocity direction from the true value. The errors and uncertainties are correspondingly greater.

4.11   Effect of the Velocity Direction

The effect of the velocity direction θ on the success rate is shown in Figure 4.10a. The velocity direction has no effect on the success rate which is almost constant at 0.98. This is because the estimated location of the pair particle is obtained from an exact velocity interpolation (see Section 3.1.3). The effect of the velocity direction on the uncertainties in velocity magnitude and direction is shown in Figure 4.10b. The systematic uncertainties in the magnitude and direction are both negligible. The random uncertainties in magnitude and direction are both almost constant as the direction of the velocity vector is varied. This indicates that they are independent of the direction of the velocity vector. Again, this is because of the exact velocity interpolation to the location of the first test particle image.
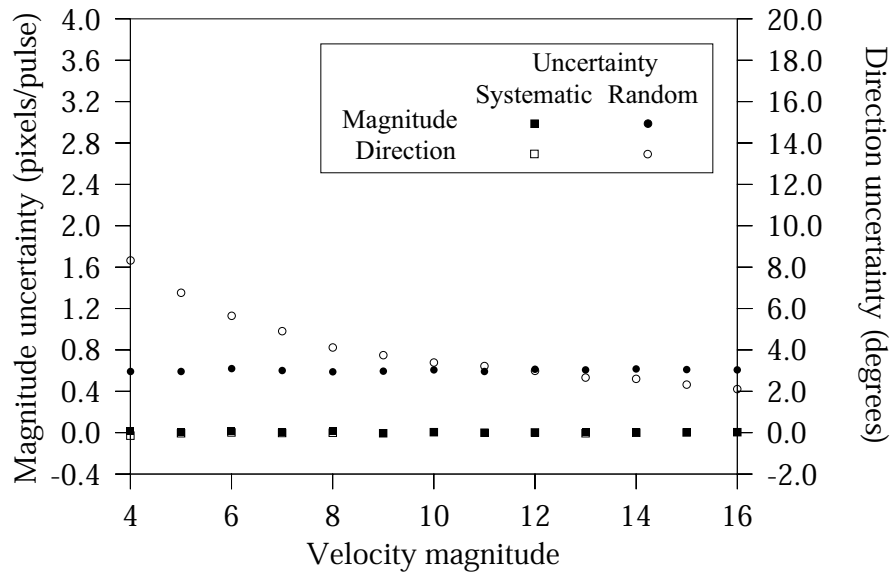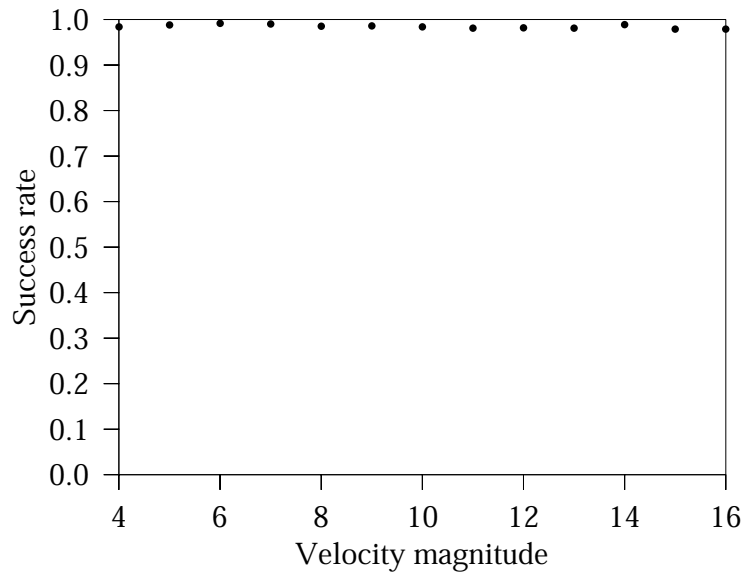
Figure 4.9: *(a) Effect of the velocity magnitude on the success rate. (b) Effect of the velocity magnitude on the magnitude and direction uncertainties.*
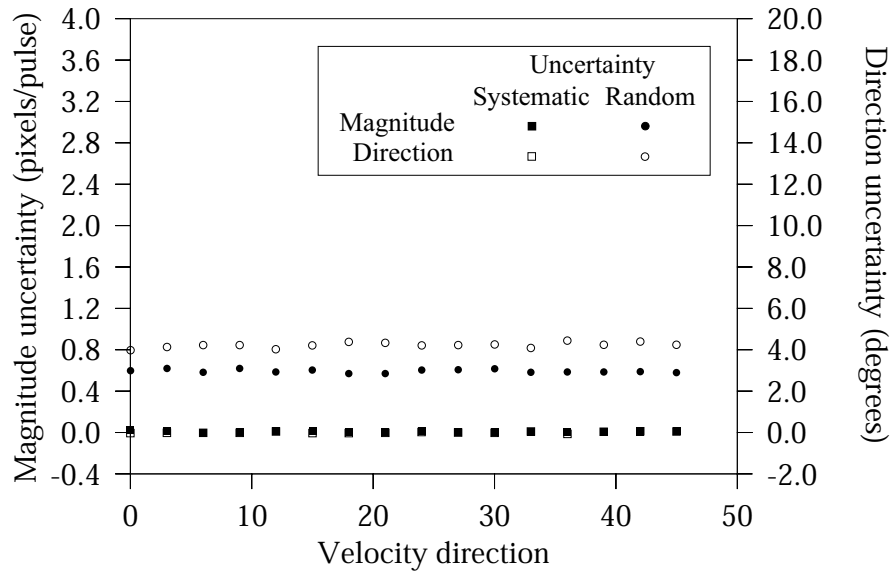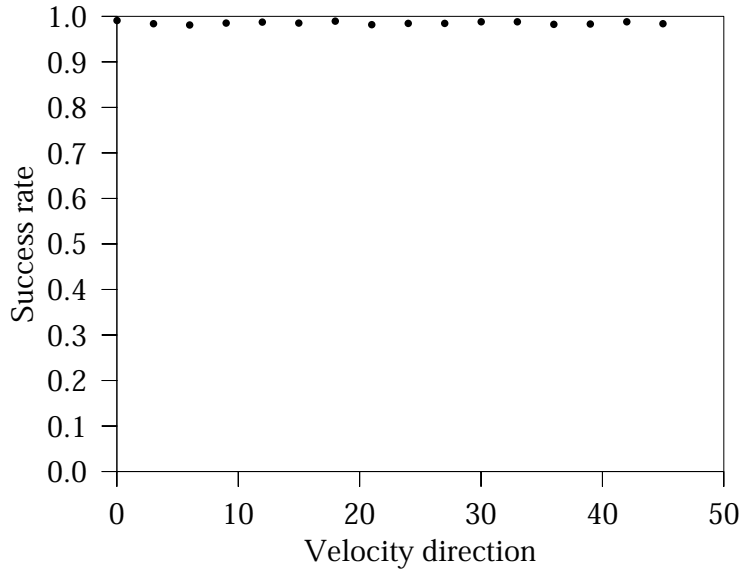
Figure 4.10: *(a) Effect of the direction of the velocity vector on the success rate. (b) Effect of the direction of the velocity vector on the magnitude and direction uncertainties.*

Chapter 5

Conclusions and Recommendations

5.1 Conclusions

In this study, the measurement uncertainty of a particle tracking algorithm was characterised for a range of image, algorithm, and flow field parameters. The results of this study can be summarised as follows.

- There is essentially no systematic uncertainty in the technique. The random uncertainty dominates.

- Particle concentrations can be much larger than that normally recommended for correlation–based PIV, without increasing the uncertainty appreciably. The recommended value of the image density (number of pairs) for correlation–based PIV is 20. Even when the image density is increased to 150 there is only a 15.5% decrease in the success rate.

- From the discussion in Section 4.7 it can be said that the success rate with which the particles can be identified is strongly influenced by the contrast. Higher success rates ensue at higher contrasts.

- Where the background noise is high and the contrast is low, selection of an optimal threshold is critical in ensuring high success rates.

- While the random uncertainties are low at small values of the search radius, the success rate is also low at these ranges. There is an opportunity to trade-off spatial resolution (success rate) with uncertainty.

5.2   Recommendations

The uncertainty analysis done in this study is limited because only the measurement uncertainty of the particle tracking stage of the super–resolution algorithm was examined. Rather than using the velocity field determined by a cross–correlation PIV algorithm, the exact velocities at the centres of interrogation areas are calculated from the velocity field equations. These exact velocities are used in the velocity interpolation to the location of the first test particle image (see Section 3.1.3). This excludes measurement uncertainty from the correlation–PIV stage. To determine the measurement uncertainty of the super–resolution algorithm, a study must be done using cross–correlation PIV results.

The performance of the tracking algorithm was investigated only for a simple shear flow. Other velocity fields should be simulated to give a more representative

indication of the performance. A coupled study with the correlation stage should be done for these flows also.

This study has not taken into account the effect of possible interactions among the independent variables. When there is interaction among two variables, the effect of a particular value of one interacting variable will depend on the value of the other variable. It is reasonable to conjecture interactions among, for example, the background intensity and the particle central intensity in this study. There can be interactions among more than two variables. *Design of experiments* (DOE) [29] offers a rigorous method for studying the effect of interactions among independent variables. A designed study should be carried out to identify the effect of parameters interactions on the measurement uncertainty.

Bibliography

[1] R.J. Adrian. Particle imaging methods in fluid mechanics. *Annual Review of Fluid Mechanics*, 23:261–304, December 1991.

[2] I. Grant. Particle image velocimetry: a review. In *Proceedings Institute of Mechanical Engineers*, C211, pages 55–76, 1997.

[3] A.M. Fox. *Course notes for PHY332 : Atomic and laser physics*. A.M.Fox, Department of Physics and Astronomy, University of Sheffield, Hicks Building, Hounsefield Road, Sheffield S3 7RH, [Online] Autumn 2001 edition, 2001. Available from the World Wide Web at `http://www.shef.ac.uk/uni/academic/N-Q/phys/teaching/phy332/`. Cited on 2002-12-25.

[4] Efunda. *Hermite polynomial*. Efunda Inc, P.O.Box 64400, Sunnyvale, CA 94088, [Online] edition, 2003. Available from the World Wide Web at `http://www.efunda.com/math/Hermite/index.cfm`. Cited on 2003-07-28.

[5] M. Raffel, C.E. Willert, and J. Kompenhans. *Particle Image Velocimetry: A Practical Guide*, chapter 5, pages 135–136. Springer Verlag, New York, June 1998.

[6] A. Melling. Tracer particles and seeding for particle image velocimetry. *Measurement Science and Technology*, 8:1406–1416, 1997.

[7] G. Gouesbet, G. Grehan, B. Maheu, and K.F. Ren. *Electromagnetic scattering of shaped beams (Generalized Lorenz - Mie theory)*. The Process and System Energetics Laboratory (LESP), LESP, CORIA, INSA se Rouen, Saint Etienne du Rouvray, March 1998.

[8] R.J. Adrian and C.-S. Yao. Pulsed laser technique application to liquid and gaseous flows and the scattering power of seed materials. *Applied Optics*, 24(1):44 – 52, January 1985.

[9] M. Stanislas and J.C. Monnier. Practical aspects of image recording in particle image velocimetry. *Measurement Science and Technology*, 8:1417–1476, 1997.

[10] J.F. Meyers. Laser velocimetry. Generation of particles and seeding. Lecture series 8, Von Karman institute for fluid dynamics, Brussels, Belgium, NASA Langley Research Centre, Hampton, Virginia, USA., June 10 - 14 1991.

[11] L.G. Brown. A survey of image registration techniques. *ACM Computing Surveys*, 24(4):325–376, 1992.

[12] J.P. Lewis. *Fast normalized cross-correlation.* Citeseer Scientific Digital Library, http://citeseer.nj.nec.com/lewis95fast.html, Autumn 1995.

[13] A.K. Jain. *Fundamentals of digital image processing.* Prentice-Hall, Englewood Cliffs, New Jersey, U.S.A, first edition, September 1989.

[14] R.D. Keane, R.J. Adrian, and Y. Zhang. Super-resolution particle imaging velocimety. *Measurement Science and Technology*, 6:754–768, 1995.

[15] Y.G. Guezennec and N. Kiritsis. Statistical investigation of errors in particle image velocimetry. *Experiments in Fluids*, 10:138–146, 1990.

[16] R.D. Keane and R.J. Adrian. Optimization of particle image velocimeters: I double pulsed systems. *Measurement Science and Technology*, 1:1202–1215, 1990.

[17] R.D. Keane and R.J. Adrian. Optimization of particle image velocimeters: II multiple pulsed systems. *Measurement Science and Technology*, 2:963–974, 1990.

[18] E.A. Cowen and S.G. Monismith. A hybrid digital particle tracking velocimetry technique. *Experiments in Fluids*, 22:199–211, 1997.

[19] J.E. Rehm and N.T. Clemens. An improved method for enhancing the resolution of conventional double-expose single-frame particle image velocimetry. *Experiments in Fluids*, 26:497–504, 1999.

[20] D.P. Hart. Super-resolution piv by recursive local-correlation. *Journal of Visualization*, 10:1–10, 1999.

[21] ISO. *Guide to the expression of uncertainty in measurement*. ISO, Geneva, Switzerland, 1st edition, 1993.

[22] ASME. Test uncertainty. Instruments and apparatus. Technical Report ASME PTC 19.1-1998, American Society of Mechanical Engineers, 1998.

[23] NIST. The International System of Units. National Institute of Science and Technology special publication 330. Barry N. Taylor, Editor, Gaithersburg, MD 20899, USA, July 2001.

[24] ISO. *International vocabulary of basic and general terms in metrology.* ISO, Geneva, Switzerland, 1993.

[25] H.W. Coleman and G.W. Steele. *Experimentation and uncertainty analysis for engineers.* Wiley Interscience, New York, second edition, December 1998.

[26] Standards Subcommittee AIAA-GTTC. *AIAA Standard S-071-1995. Assessment of wind tunnel data uncertainty.* Standards Series. AIAA, 1995.

[27] G.R. Spedding and J.M. Rignot. Performance analysis and application of grid interpolation techniques for fluid flows. *Experiments in Fluids*, 15:417–430, 1993.

[28] E. Peli. Contrast in complex images. *Journal of the Optical Society of America A*, 7(10):2032–2040, October 1990.

[29] D. Montgomery. *Design and Analysis of Experiments.* John Wiley and Sons, New York, fifth edition, June 2000.

[30] J.L. Devore. *Probability and statistics for engineering and the sciences.* Brooks/Cole Publishing Company, Forest Grove, CA 93950, 4th edition, 1995.

[31] B. R. Munson, D. F. Young, and T. H. Okiishi. *Fundamentals of fluid mechanics*, chapter 6, pages 320–322. John Wiley and Sons, New York, 3rd update edition, 1998.

[32] J. Stewart. *Calculus*, chapter 16, pages 1011–1014. Brooks/Cole Publishing Company, Pacific Grove, CA 93950, USA, 4th edition, 1999.

Appendix A

Review of Mathematics

This appendix gives a review of the mathematics needed for developing the expression for the overall measurement uncertainty.

A.1 Probability Theory Terminology

Experiment An *experiment* is a well defined procedure which generates outcomes. The set of all possible outcomes of the experiment is called the *sample space* of the experiment and is denoted by S.

Event A subset of outcomes in the sample space S of an experiment is called an *event*. A *simple event* consists of exactly one outcome. A *compound event* consists of more than one outcome.

Random variable A *random variable* is a rule that associates a number with each outcome in the sample space S of an experiment. $X(s) = x$ indicates that the

random variable X associates the number x with the outcome s. A continuous random variable can assume an infinite number of values within an interval. A discrete random variable can assume a finite number of values from a discrete set.

Population A *population* consists of the entire collection of individuals or measurements for which information is needed.

Sample A *sample* is an available subset of the population.

A random variable is denoted by an upper case Roman letter, for example, X. The observed value of the random variable is denoted by the corresponding lower case Roman letter, for example, x.

A.2 Probability Density Function

The probability density function of a continuous random variable is a function $f(x)$ such that, for any two numbers a and b, $a < b$, the probability that X takes on a value in the interval $[a, b]$ is given by

$$P\left(a \leq x \leq b\right) = \int_a^b f(x)dx. \tag{A.1}$$

In Figure A.1, the area under the graph of the probability density function $f(x)$ between a and b is the probability that the random variable takes on a value in the interval $[a, b]$.
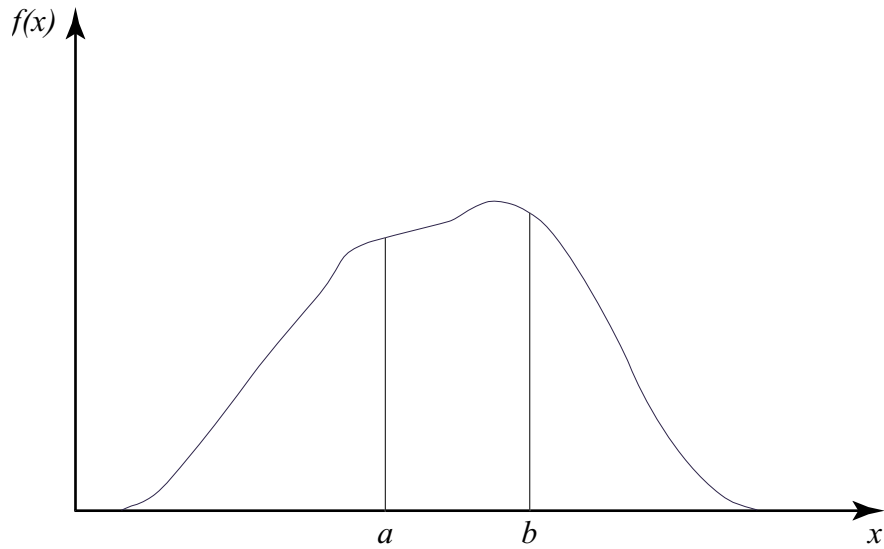
Figure A.1: *Probability Density Function*

A.3 Cumulative Distribution Function

The cumulative distribution function $F(x)$ for a continuous random variable X gives the probability that the random variable is less than or equal to x for every number x.

$$F(x) = P(X \leq x) = \int_{-\infty}^{x} f(y)\, dy. \tag{A.2}$$

$F(x)$ is the area under the graph of the probability density function to the left of the number x on the x axis. If X is a random variable with probability density function $f(x)$ and cumulative distribution function $F(x)$, the probability that X takes on a value in the interval $[a, b]$ is

$$P(a \leq x \leq b) = F(b) - F(a). \tag{A.3}$$
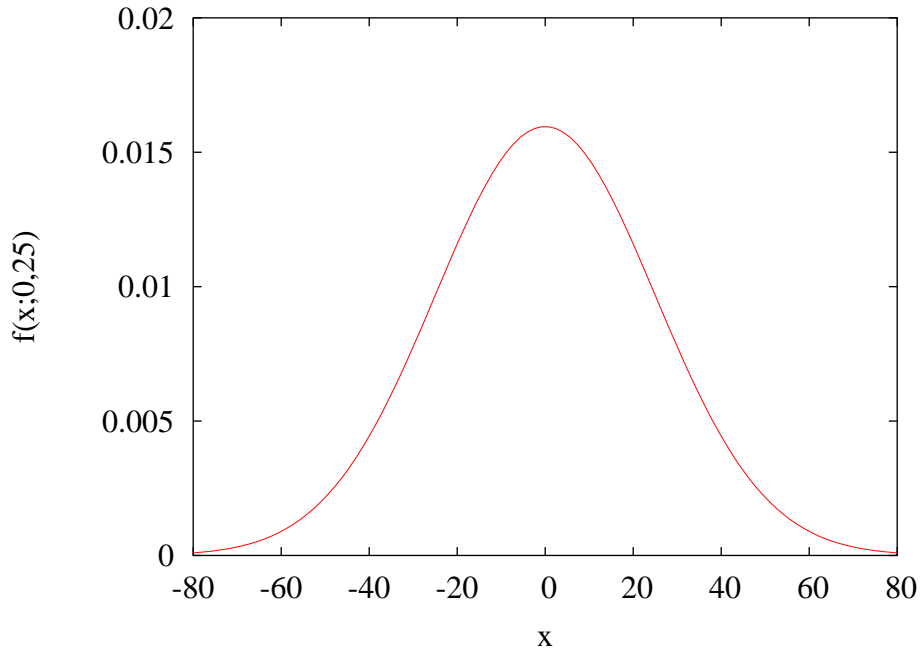
Figure A.2: *Normal probability density function*

A.4 Normal Probability Distribution

A continuous random variable X, assuming all real values in the range $(-\infty, \infty)$ is said to have a *normal distribution* with parameters μ and σ if it has the probability density function

$$f\left(x; \mu, \sigma\right) = \frac{1}{\sqrt{2\pi}\sigma} e^{-\frac{(x-\mu)^2}{2\sigma^2}}, -\infty < x < \infty, \tag{A.4}$$

where μ is the mean, and σ is the standard deviation of the distribution. The standard deviation σ is the distance from the mean to the inflection points of the curve. Figure A.2 shows the graph of a normal probability distribution with $\mu = 0$ and $\sigma = 25$. The

normal probability distribution function has a symmetric, bell shaped curve centred at the mean. For a normally distributed random variable

$$P(a \leq x \leq b) = \int_a^b \frac{1}{\sqrt{2\pi}\sigma} e^{-\frac{(x-\mu)^2}{2\sigma^2}} dx. \tag{A.5}$$

A.5 Standard Normal Distribution

A *standard normal distribution* is a normal distribution with parameters $\mu = 0$ and $\sigma = 1$. The random variable Z which has a standard normal distribution is called a standard normal random variable. The probability density function for the standard normal random variable is

$$f(z; 0, 1) = \frac{1}{\sqrt{2\pi}\sigma} e^{-\frac{z^2}{2}}, \quad -\infty < z < \infty. \tag{A.6}$$

Equation A.6 is obtained by substituting $\mu = 0$ and $\sigma = 1$ in Equation A.5. The cumulative distribution function for the standard normal random variable is

$$P(Z \leq z) = \phi(z) = \int_{-\infty}^z f(y; 0, 1) dy. \tag{A.7}$$

It is the area under the graph of the standard normal curve to the left of z on the abscissa.

A.6   Computing Probabilities

Equation A.5 cannot be evaluated using standard integration methods. It is evaluated numerically for $\mu = 0$ and $\sigma = 1$ for a number of values of a and b. Devore [30] gives a table of standard normal curve areas. If a random variable X is normally distributed with mean μ and standard deviation σ, then

$$Z = \frac{X - \mu}{\sigma} \tag{A.8}$$

is a standard normal random variable. A normal random variable can be standardised and the probabilities computed using standard normal curve area tables.

A.7   Random Sample

A collection of n random variables $X_1, X_2, \ldots X_n$ is a *random sample* if the X_i's are independently and identically distributed. That is, the X_i's are independent random variables and every X_i has the same probability distribution. When sampling with replacement, or when sampling from an infinite conceptual population, these conditions are exactly satisfied. When sampling from a finite population without replacement the conditions are approximately satisfied.

A.8 Sample Mean

Let $X_1, X_2, \ldots X_n$ be a random sample. The random variable

$$\bar{X} = \frac{1}{n} \sum_{i=1}^{n} X_i \qquad (A.9)$$

is called the sample mean. Since the X_i's are random variables $\bar{X}$ is also a random variable.

A.9 Linear Combinations

The random variable

$$Y = a_1 X_1 + \cdots + a_n X_n = \sum_{i=1}^{n} a_i X_i \qquad (A.10)$$

is called a linear combination of the n random variables $X_1, X_2, ..., X_n$. The a_i are numerical constants. The expected value of a linear combination of random variables is a linear combination of the expected values, irrespective of whether the X_i's are independent or not.

$$E\left(a_1 X_1 + \cdots + a_n X_n\right) = a_1 E\left(X_1\right) + a_2 E\left(X_2\right) + \cdots a_n E\left(X_n\right). \qquad (A.11)$$

When the X_i's are independent, the variance of the linear combination of random variables is

$$V(a_1 X_1 + \cdots + a_n X_n) = a_1^2 \sigma_1^2 + a_2^2 \sigma_2^2 + \cdots a_n^2 \sigma_n^2 = \sum_{i=1}^{n} a_i^2 . V(X_i) \qquad \text{(A.12)}$$

where $V(X_i) = \sigma_i^2$ is the variance of X_i. If $X_1, X_2, ..., X_n$ are independent normal random variables, any linear combination

$$Y = a_1 X_1 + a_2 X_2 \cdots a_n X_n \qquad \text{(A.13)}$$

has a normal distribution with mean

$$\mu_Y = \sum_{i=1}^{n} a_i \mu_i$$

and variance

$$\sigma_Y^2 = \sum_{i=1}^{n} a_i^2 \sigma_i^2 .$$

Additionally if $X_1, X_2 \ldots X_n$ is a random sample from a normal distribution (each X_i has the **same** normal distribution with mean μ and variance σ^2), then $\bar{X}$ is normally distributed with mean μ and variance σ^2/n.

A.10 Central Limit Theorem

Theorem A.10.1 (Central Limit) *If the sample size n is sufficiently large, the sample mean $\bar{X}$ of a random sample $X_1, X_2, \ldots X_n$ from a distribution with mean μ and variance σ^2 has an approximately normal distribution with mean $\mu_{\bar{X}} = \mu$ and variance $\sigma^2_{\bar{X}} = \sigma^2/n$.*

As the sample size gets larger, the approximation gets better. The Central Limit Theorem requires only the assumption of a random sample. The distribution need not be normal. It can be used with confidence for $n > 30$.

A.11 Parameter and Statistic

Parameter A parameter is a numerical characteristic of a population, for example, the population mean μ or the population variance σ^2. A parameter has a fixed value characteristic of the probability distribution modelling the population.

Statistic A statistic is any function of the random variables constituting one or more samples, which does not depend on the values of any unknown parameter of the population. It is a numerical characteristic of a sample, for example, the sample mean $\bar{X}$ or the sample variance S^2. The calculated value of a statistic varies from sample to sample, a process termed statistical variation or statistical fluctuation.

A.12   Parameter Estimation

Parameter estimation is the procedure of inferring the value of a parameter by a value calculated from sample data. *Point estimation* and *interval estimation* are two parameter estimation procedures. The estimates are called, respectively, the *point estimate* and the *interval estimate.*

A.12.1   Point Estimation

Point Estimator The point estimate of a parameter is the single number that can be regarded as its most likely value. A point estimate is obtained by selecting a suitable statistic called the *point estimator* and computing its value from the sample data. For example, the sample mean $\bar{X}$ is a point estimator of the population mean μ.

Point Estimate A point estimate is the value of a point estimator calculated from the sample data. In the example above the calculated value of the sample mean $\bar{x}$ is the point estimate of μ.

The point estimator of a parameter is a random variable until its value is calculated from the sample data. Upper-case letters with a circumflex are used to denote point estimators, for example, $\hat{\Theta}$. Point estimates, which are the calculated values, are denoted by the corresponding lower case letters with a circumflex, for example, $\hat{\theta}$.

A.12.2   Interval Estimation

A point estimate generally approximates the value of the parameter being estimated. There is no indication of the precision of the point estimate. An *interval estimate* gives an indication of the precision of a point estimate by specifying a range of values within which the parameter is expected to lie. An interval estimate is specified by reporting the *standard error* or by specifying a *confidence interval*.

A.13   Standard Error

The standard error of a point estimator is its standard deviation. The ISO *Guide to the Expression of Uncertainty in Measurement* (GUM)[21] uses the term **standard uncertainty** instead of standard error.

A.14   Confidence Interval

A confidence interval is an interval estimate with an associated probability level. The probability level, the *confidence level*, is usually specified as a percentage (for example, a 95% confidence level). A confidence interval specifies a set of plausible values of the estimated parameter. Consider the case where random samples are repeatedly taken from a given population. Let $\hat{\Theta}$ be the point estimator of a parameter Θ. If the 95% confidence interval about the point estimate $\hat{\theta}$ is calculated for each sample, 95% of the confidence intervals will contain Θ. The upper and lower bounds of a confidence interval are called *confidence limits*. In the next three sections 95%

confidence intervals are developed for the population mean μ for three different cases.

A.15 95% **Confidence Intervals for** μ

Let $X_1, X_2, \ldots X_n$ be a random sample drawn from a population with mean μ and standard deviation σ. Consider the case where μ is estimated by the sample mean $\bar{X}$. A confidence interval about $\bar{x}$ specifies a set of values which is expected to include μ. Situations where the sample mean $\bar{x}$ is the point estimator of the population mean μ are often encountered. The determination of the value of a measurand by repeated measurements is an example. The overall measurement uncertainty $U_{\bar{X}}$ is, by definition, the absolute value of the 95% confidence limits. The 95% confidence interval centred at $\bar{x}$ is $(\bar{x} - U_{\bar{x}}, \bar{x} + U_{\bar{x}})$.

A.15.1   **Normal Population with Known** σ

Let Z be a standard normal random variable. Then

$$P\left(-1.96 \leq Z \leq 1.96\right) = \phi\left(1.96\right) - \phi\left(-1.96\right) = 0.95 \qquad \text{(A.14)}$$

This result is calculated using standard normal curve area tables (see Devore [30]). Let $X_1, X_2 \ldots X_n$ be a random sample from a normal distribution with mean μ and standard deviation σ. Then the sample mean $\bar{X}$ is normally distributed with mean

μ and standard deviation σ/n (See Section A.9). Therefore

$$Z = \frac{(\bar{X} - \mu)}{\sigma/\sqrt{n}} \tag{A.15}$$

is a standard normal random variable and

$$P\left(-1.96 \leq \frac{(\bar{X} - \mu)}{\sigma/\sqrt{n}} \leq 1.96\right) = 0.95. \tag{A.16}$$

This can be expressed as

$$P\left(\bar{X} - 1.96\frac{\sigma}{\sqrt{n}} \leq \mu \leq \bar{X} + 1.96\frac{\sigma}{\sqrt{n}}\right) = 0.95. \tag{A.17}$$

According to Equation A.17, the probability that the random interval

$$\left(\bar{X} - 1.96\frac{\sigma}{\sqrt{n}}, \bar{X} + 1.96\frac{\sigma}{\sqrt{n}}\right)$$

includes the true value of μ is 0.95. By convention, $\bar{X}$ refers to the sample mean prior to observation of the X_i's. The observed value of the sample mean is $\bar{x}$. If $\bar{X}$ is replaced in Equation A.17 by the calculated value of the sample mean $\bar{x}$, then

$$P\left(\bar{x} - 1.96\frac{\sigma}{\sqrt{n}} \leq \mu \leq \bar{x} + 1.96\frac{\sigma}{\sqrt{n}}\right) = 0.95 \tag{A.18}$$

is a confidence interval for μ.

Interpreting a Confidence Interval

Consider that the population mean μ of a normally distributed population is being estimated by the sample mean $\bar{X}$. If a sample is drawn from the population and the sample mean is calculated, 95 times out of 100, the confidence interval, Equation A.18, will include the population mean μ.

A.15.2   Large Sample Confidence Interval

In the development of the confidence interval Equation A.18 it is assumed that the population distribution is normal and that the population standard deviation σ is known. If these assumptions are not valid, the *large sample confidence interval* can be used to specify a confidence interval, if the sample size n is large enough to use the Central Limit Theorem. According to the Central Limit Theorem, if $X_1, X_2 \ldots X_n$ is a random sample drawn from a population with mean μ and standard deviation σ, the sample mean $\bar{X}$ has approximately a normal distribution, provided that the sample size n is large. The sample need not be drawn from a population which is normally distributed. The random variable

$$Z = \frac{(\bar{X} - \mu)}{\sigma/\sqrt{n}} \tag{A.19}$$

has approximately a standard normal distribution. Therfore

$$P\left(-1.96 \leq \frac{(\bar{X} - \mu)}{\sigma/\sqrt{n}} \leq 1.96\right) = 0.95. \tag{A.20}$$

From Equation A.20, the large sample confidence interval about the sample mean at approximately 95% is

$$P\left(\bar{X} - 1.96\frac{\sigma}{\sqrt{n}} \leq \mu \leq \bar{X} + 1.96\frac{\sigma}{\sqrt{n}}\right) = 0.95 \qquad \text{(A.21)}$$

The second assumption in developing Equation A.18, that the population standard deviation σ is known, is often not valid. This is because the population mean μ is usually known before the population standard deviation. Instead of σ, if the sample standard deviation

$$S = \left(\frac{\sum\limits_{i=1}^{n}\left(x_i - \bar{x}\right)^2}{n-1}\right)^{\frac{1}{2}} \qquad \text{(A.22)}$$

is used, not much variability is added to the standardized normal random variable

$$Z = \frac{\left(\bar{X} - \mu\right)}{S/\sqrt{n}} \qquad \text{(A.23)}$$

if n is large. This is because the computed value s will approximate σ closely. The new Z also has approximately a normal distribution. The large sample confidence interval about the sample mean at the 95% level is then

$$P\left(\bar{X} - 1.96\frac{s}{\sqrt{n}} \leq \mu \leq \bar{X} + 1.96\frac{s}{\sqrt{n}}\right) = 0.95. \qquad \text{(A.24)}$$

A.15.3 Small Sample Size

In developing the large sample confidence interval it is assumed that the sample size n is large enough to apply the Central Limit Theorem. The confidence interval given by Equation A.24 can then be used irrespective of the distribution from which the sample is obtained. When n is not large enough to use the Central Limit Theorem, an assumption is made about the population distribution and a confidence interval suited for the assumed population distribution is developed. For example, a Gamma distribution or a Weibull distribution may be assumed for the population to develop a confidence interval for the population mean μ. The normal distribution frequently models a population. So it is common to develop a confidence interval for the population mean assuming a normal population distribution.

Let $X_1, X_2 \ldots X_n$ be a random sample from a normal distribution. The sample size n is not large enough to use the Central Limit Theorem. The mean μ and standard deviation σ are not known. For the large sample case, the standardised variable

$$Z = \frac{\bar{X} - \mu}{S/\sqrt{n}}$$

was taken to have an approximately normal distribution. When n is not large enough, the sample standard deviation S, which is a randomly varying quantity from sample to sample, is no longer likely to be close to σ. The randomness in Z arises both from the numerator and the denominator. Z will therefore have a probability distribution more spread out than a standard normal distribution, called a Student's t distribution. For a random sample of size n, taken from a normal distribution with mean μ, the

126

random variable

$$T = \frac{\left(\bar{X} - \mu\right)}{S/\sqrt{n}} \tag{A.25}$$

has a Student's t distribution with $n - 1$ degrees of freedom. The notation T for the standardised variable denotes the t distribution.

A.16   The t Distribution

A parameter called the number of degrees of freedom ν which takes positive integer values characterises the t distribution. Each value of ν gives a different t distribution. The probability density function curve for ν degrees of freedom is denoted by t_ν. The probabililty density function of the t distribution with ν degrees of freedom is

$$f\left(t, \nu\right) = \frac{\Gamma\left(\frac{\nu+1}{2}\right)}{\sqrt{\nu\pi}.\Gamma\left(\frac{\nu}{2}\right)} \left(\frac{1}{1 + \frac{t^2}{\nu}}\right)^{\frac{\nu+1}{2}} \tag{A.26}$$

where $\Gamma\left(x\right)$ is the Gamma function. The Gamma function is defined as

$$\Gamma\left(z\right) = \int_0^\infty t^{z-1}e^{-t}dt. \tag{A.27}$$

Figure A.3 shows a t distribution with six degrees of freedom. The t_ν curve is bell shaped, centred at 0, and more spread out than the standard normal curve. The spread decreases as ν increases, and as $\nu \to \infty$, the sequence of curves approaches the standard normal curve. If n is the sample size, the number of degrees of freedom for the random variable T in Equation A.25 is $n - 1$, because though S is based on
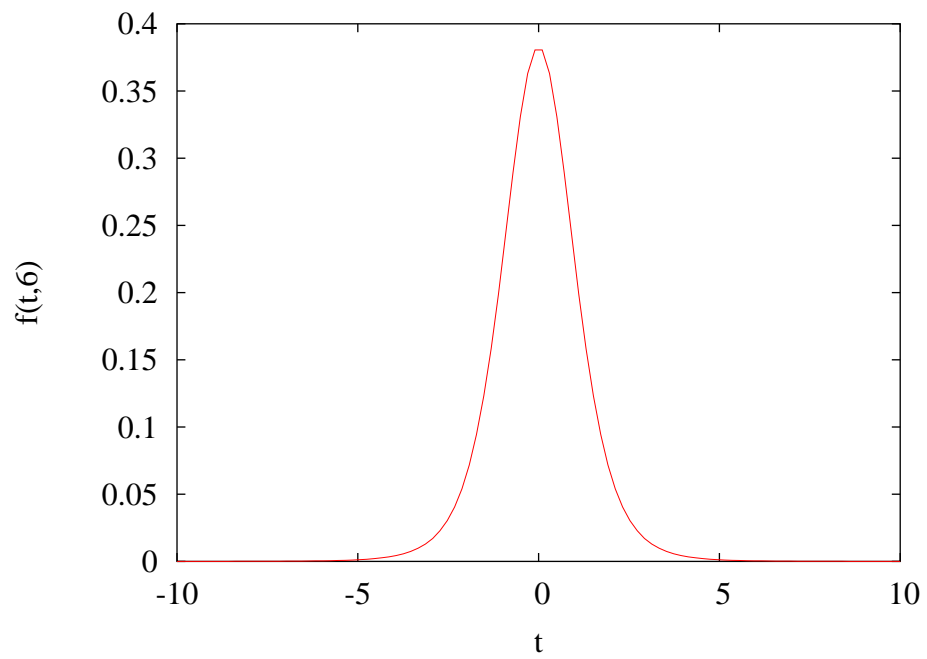
Figure A.3: *Student's t distribution* t_6
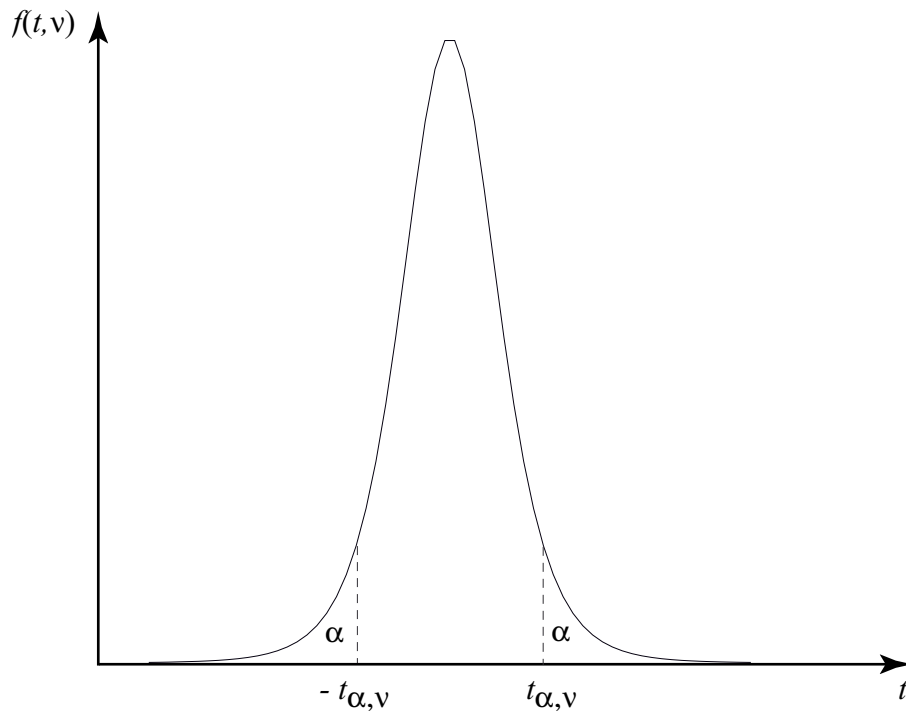
Figure A.4: *Critical value $t_{\alpha,\nu}$ of the Student's t distribution. The critical value $t_{\alpha,\nu}$ is the number on the t axis for which the area under the t_ν curve to the right of $t_{\alpha,\nu}$ is α. By symmetry, the area under the t_ν curve to the left of $-t_{\alpha,\nu}$ is also α.*

n deviations, only $n - 1$ are freely determined.

A.16.1 t Critical Value

The t critical value $t_{\alpha,\nu}$ is the number on the t axis for which the area under the t_ν curve to the right of $t_{\alpha,\nu}$ is α. See Figure A.4. By symmetry, the area under the t_ν curve to the left of $-t_{\alpha,\nu}$ is also α. Appendix Table A.5, Devore [30], gives $t_{\alpha,\nu}$ for certain values of α and ν.

A.17   Confidence Interval for Mean

For the t distribution with ν degrees of freedom, the area under the t_ν curve between $-t_{\alpha,\nu}$ and $t_{\alpha,\nu}$ is $1 - 2\alpha$. See Figure A.4. Therefore

$$P\left(-t_{\alpha,\nu} \le T \le t_{\alpha,\nu}\right) = 1 - 2\alpha \tag{A.28}$$

Substituting for T from Equation A.25,

$$P\left(-t_{\alpha,\nu} \le \frac{(\bar{X} - \mu)}{S/\sqrt{n}} \le t_{\alpha,\nu}\right) = 1 - 2\alpha \tag{A.29}$$

For the 95% confidence interval $1 - 2\alpha = 0.95$, $\alpha = 0.025$, and

$$P\left(-t_{0.025,\nu} \le \frac{(\bar{X} - \mu)}{S/\sqrt{n}} \le t_{0.025,\nu}\right) = 0.95. \tag{A.30}$$

The 95% confidence interval for the population mean μ is

$$P\left(\bar{X} - t_{0.025,\nu} \cdot \frac{S}{\sqrt{n}} \le \mu \le \bar{X} + t_{0.025,\nu} \cdot \frac{S}{\sqrt{n}}\right) = 0.95. \tag{A.31}$$

Appendix B

Streamlines of the Shear Flow

B.1 Vector Fields

Let E be a set in $\mathbb{R}^3$. A function $\mathbf{F}$ which assigns a three dimensional vector $\mathbf{F}(x, y, z)$ to each point (x, y, z) is called a *vector field* on $\mathbb{R}^3$. The three dimensional vector $\mathbf{F}(x, y, z)$ can be written in terms of its component functions P, Q, R.

$$\begin{aligned}
\mathbf{F}(x, y, z) &= P(x, y, z)\mathbf{i} + Q(x, y, z)\mathbf{j} + R(x, y, z)\mathbf{k} \\
&= \langle P(x, y, z), Q(x, y, z), R(x, y, z)\rangle
\end{aligned}$$

(B.1)

where P, Q and R are scalar functions of three variables.

B.1.1 Curl of a Vector Field on $\mathbb{R}^3$

The *curl* of a vector field $\mathbf{F}$ on $\mathbb{R}^3$ is defined to be

$$
\begin{aligned}
\nabla \times \mathbf{F} &= \begin{vmatrix} \mathbf{i} & \mathbf{j} & \mathbf{k} \\ \frac{\partial}{\partial x} & \frac{\partial}{\partial y} & \frac{\partial}{\partial z} \\ P & Q & R \end{vmatrix} \\
&= \left(\frac{\partial R}{\partial y} - \frac{\partial Q}{\partial z} \right) \mathbf{i} + \left(\frac{\partial P}{\partial z} - \frac{\partial R}{\partial x} \right) \mathbf{j} + \left(\frac{\partial Q}{\partial x} - \frac{\partial P}{\partial y} \right) \mathbf{k} \\
&= \operatorname{curl} \mathbf{F}
\end{aligned}
\tag{B.2}
$$

B.1.2 Fluid Flow Velocity Vector Field on $\mathbb{R}^3$

For steady motion of a fluid in Cartesian three dimensional space $\mathbb{R}^3$,

$$
\mathbf{V}(x,y,z) = u(x,y,z)\mathbf{i} + v(x,y,z)\mathbf{j} + w(x,y,z)\mathbf{k}
\tag{B.3}
$$

is called a flow velocity vector field if $\mathbf{V}$ assigns a velocity vector to each point (x, y, z). At a location x, y, z in the flow field, fluid particles tend to rotate about the axis that points in the direction of the vector curl $\mathbf{V}$. The flow velocity field is said to be *irrotational* when the *vorticity*

$$
\zeta = \operatorname{curl} \mathbf{V} = \left(\frac{\partial w}{\partial y} - \frac{\partial v}{\partial z} \right) \mathbf{i} + \left(\frac{\partial u}{\partial z} - \frac{\partial w}{\partial x} \right) \mathbf{j} + \left(\frac{\partial v}{\partial x} - \frac{\partial u}{\partial y} \right) \mathbf{k} = \mathbf{0}
\tag{B.4}
$$

B.2 Two Dimensional Flow Field

When one of the component functions of the velocity field Equation B.3 is small in comparison to the other two, it can be neglected. The flow is then *two-dimensional*. When w is small compared to the other two component functions u and v, and the flow is in the xy plane Equation B.3 becomes

$$\mathbf{V}(x, y) = u(x, y)\mathbf{i} + v(x, y)\mathbf{j} \tag{B.5}$$

For a two-dimensional flow u and v are not functions of z. Therefore in Equation B.4, $\partial u/\partial z$ and $\partial v/\partial z$ are zero. By definition, w is zero for a two-dimensional flow. Thus the condition for irrotationality of the two-dimensional flow is

$$\left(\frac{\partial v}{\partial x} - \frac{\partial u}{\partial y}\right) = 0 \tag{B.6}$$

B.3 Stream Function, Streamlines

For steady, incompressible, plane, two-dimensional flow, the continuity equation is

$$\frac{\partial u}{\partial x} + \frac{\partial v}{\partial y} = 0 \tag{B.7}$$

133

The velocity components u and v can be specified in terms of a function $\psi(x, y)$ of two variables such that

$$u = \frac{\partial \psi}{\partial y} \tag{B.8a}$$

$$v = -\frac{\partial \psi}{\partial x} \tag{B.8b}$$

The function $\psi(x, y)$ of two variables is called the *stream function* [31].

Lines of constant ψ are called *streamlines*. They are everywhere tangent to the velocity vectors in a flow field. If the stream function $\psi(x, y)$ is known, then the flow may be visualised by plotting the streamlines.

B.4   Pathlines

Pathlines are lines traced out by a given particles as they flow from one point to another. For a steady flow, streamlines and pathlines are the same.

B.5   Streamlines for the Simple Shear Flow

Consider the steady, simple shear flow given by Equations 3.16a and 3.16b. They are reproduced below:

$$u = \frac{\partial \psi}{\partial y} = a + by \qquad (B.9)$$

$$v = -\frac{\partial \psi}{\partial x} = c + dx \qquad (B.10)$$

The streamfunction for this flow can derived making use of Equations B.8a and B.8b as follows. Integrating Equation B.9 with respect to y gives

$$\psi = ay + \frac{by^2}{2} + g(x) \qquad (B.11)$$

where $g(x)$ is a function of x. Differentiating Equation B.11 with respect to x gives

$$\frac{\partial \psi}{\partial x} = g'(x) \qquad (B.12)$$

or,

$$-\frac{\partial \psi}{\partial x} = -g'(x) \qquad (B.13)$$

Comparing Equations B.13 and B.10,

$$g'(x) = -c - dx \qquad (B.14)$$

Integrating Equation B.14 with respect to x gives

$$g(x) = -cx - \frac{dx^2}{2} + K \qquad (B.15)$$

where K can be any constant. Setting K to zero and substituting this value of $g(x)$ in Equation B.11 will give the stream function for the simple shear flow as

$$\psi(x, y) = ay + \frac{by^2}{2} - cx - \frac{dx^2}{2} \tag{B.16}$$

Every constant value of $\psi(x, y)$ gives a streamline in the flow velocity field. Imposing condition B.6 on the simple shear flow equations 3.16a and 3.16b gives

$$d - c = 0 \tag{B.17}$$

or

$$d = c \tag{B.18}$$

The flow is irrotational when the velocity gradients in the x and y directions are either both zero or both equal.

Appendix C

Calculating Pixel Intensity

C.1 Fubini's Theorem

Fubini's theorem states:

Theorem C.1.1 *Let $f(x, y)$ be continous on the rectangle* $\mathbf{R} = [\mathbf{a}, \mathbf{b}] \times [\mathbf{c}, \mathbf{d}] = \{(x, y) \in \mathbb{R}^2 | \mathbf{a} \le x \le \mathbf{b}, \mathbf{c} \le y \le \mathbf{d}\}$. *Then,*

$$\iint_{\mathbf{R}} f(x, y) \, dA = \int_a^b \int_c^d f(x, y) \, dy dx. \tag{C.1}$$

When $f(x, y)$ can be factored as the product of a function only of x and only of y, then [32]

$$\iint_{\mathbf{R}} f(x, y) \, dA = \int_c^d \int_a^b g(x) h(y) dx dy = \int_a^b g(x) dx \int_c^d h(y) dy. \tag{C.2}$$

C.2   Average Pixel Intensity

The average intensity over pixel $\mathbf{P} = [e, f] \times [g, h]$ of Figure 3.11 is given by (see page 66)

$$I_{ave} = \frac{1}{A(\mathbf{P})} \iint_{\mathbf{P}} I(x, y)\, dA = \frac{1}{A(\mathbf{P})} \int_i^j \int_k^l I_0 e^{-\left(\frac{x^2 + y^2}{R^2}\right)}. \tag{C.3}$$

The sides of the pixel are of unit length. Therefore

$$A(\mathbf{P}) = 1. \tag{C.4}$$

Substitute $A(\mathbf{P}) = 1$ into Equation C.3. $I(x, y)$ can be split into a function of x only and y only. Therefore

$$I_{ave} = I_0 \int_i^j e^{-\left(\frac{x^2}{R^2}\right)} dx. \int_k^l e^{-\left(\frac{y^2}{R^2}\right)} dy. \tag{C.5}$$

Equation C.5 is evaluated using the following result from Appendix D:

$$\int_s^t e^{-x^2} dx = \frac{\sqrt{\pi}}{2} \left(\operatorname{erf} t - \operatorname{erf} s\right). \tag{C.6}$$

Multiplying and dividiing Equation C.5 by R^2,

$$I_{ave} = I_0 R^2 \int_i^j e^{-\left(\frac{x^2}{R^2}\right)} \frac{dx}{R}. \int_k^l e^{-\left(\frac{y^2}{R^2}\right)} \frac{dy}{R}. \tag{C.7}$$

Let

$$x/R = \xi \tag{C.8a}$$

$$\text{and} \quad y/R = \zeta \tag{C.8b}$$

Then

$$dx/R = d\xi \tag{C.8c}$$

$$\text{and} \quad dy/R = d\zeta. \tag{C.8d}$$

When $x = i$, $\xi = i/R$ and when $x = j$, $\xi = j/R$. When $y = k$, $\zeta = k/R$ and when $y = l$, $\zeta = l/R$. The new limits of integration are $m = i/R$, $n = j/R$, $o = k/R$ and $p = l/R$. Substitute Equations C.8a to C.8d into Equation C.7. Then

$$I_{ave} = I_0 R^2 \int_m^n e^{-\xi^2} d\xi . \int_o^p e^{-\zeta^2} d\zeta . \tag{C.9}$$

Now using Result C.6, the average intensity over the area of the pixel **P** is

$$I_{ave} = \frac{I_0 R^2 \pi}{4} \left(\text{erf } m - \text{erf } n \right) \left(\text{erf } o - \text{erf } p \right). \tag{C.10}$$

Appendix D

Derivation of Result C.6

The following result is demonstrated in this appendix.

Result D.0.1

$$\int_s^t e^{-x^2} dx = \frac{\sqrt{\pi}}{2} \left(erf\, t - erf\, s \right).$$

(D.1)

where erf w is defined as

$$erf\, w = \frac{2}{\sqrt{\pi}} \int_0^w e^{-x^2} dx.$$

(D.2)

To show that the right side and left side of Result D.0.1 evaluates to the same expression, the Maclaurin series expansion of e^{-x^2} is needed.

Result D.0.2 *The Maclaurin series of a function $f(x)$ is given by*

$$f(x) = \sum_{n=0}^{\infty} \frac{f^n(0)}{n!} x^n = f(0) + \frac{f'(0)}{1!} x + \frac{f''(0)}{2!} x^2 + \dots$$

(D.3)

The Maclaurin series of $f(x) = e^{-x^2}$ is

$$e^{-x^2} = 1 - \frac{x^2}{1!} + \frac{x^4}{2!} - \frac{x^6}{3!} + \ldots = \sum_{n=0}^{\infty} (-1)^n \frac{x^{2n}}{n!} \tag{D.4}$$

Equation D.4 converges for all x. Replace e^{-x^2} by its Maclaurin series in Equation D.2 and carry out term by term integration to evaluate erf w.

$$\begin{aligned}
\text{erf } w &= \frac{2}{\sqrt{\pi}} \int_0^w e^{-x^2} dx \\
&= \frac{2}{\sqrt{\pi}} \int_0^w \left(1 - \frac{x^2}{1!} + \frac{x^4}{2!} - \frac{x^6}{3!} + \ldots + (-1)^n \frac{x^{2n}}{n!} + \ldots \right) dx \tag{D.5}
\end{aligned}$$

$$= \frac{2}{\sqrt{\pi}} \left[C + x - \frac{x^3}{3.1!} + \frac{x^5}{5.2!} - \frac{x^7}{7.3!} + \ldots + (-1)^n \frac{x^{2n+1}}{(2n+1)n!} + \ldots \right]_0^w \tag{D.6}$$

$$= \frac{2}{\sqrt{\pi}} \left[w - \frac{w^3}{3.1!} + \frac{w^5}{5.2!} - \frac{w^7}{7.3!} + \ldots + (-1)^n \frac{w^{2n+1}}{(2n+1)n!} + \ldots \right] \tag{D.7}$$

In Equation D.6, C is a constant of integration. From Equation D.7,

$$\frac{\sqrt{\pi}}{2} \text{erf } w = \left[w - \frac{w^3}{3.1!} + \frac{w^5}{5.2!} - \frac{w^7}{7.3!} + \ldots + (-1)^n \frac{w^{2n+1}}{(2n+1)n!} + \ldots \right] \tag{D.8}$$

141

The right side of Equation D.1 evaluates to

$$\frac{\sqrt{\pi}}{2}(\text{erf } t - \text{erf } s) = \left[t - \frac{t^3}{3.1!} + \frac{t^5}{5.2!} - \frac{t^7}{7.3!} + \ldots + (-1)^n \frac{w^{2n+1}}{(2n+1)n!} + \ldots\right]$$
$$- \left[s - \frac{s^3}{3.1!} + \frac{s^5}{5.2!} - \frac{s^7}{7.3!} + \ldots + (-1)^n \frac{s^{2n+1}}{(2n+1)n!} + \ldots\right] \quad \text{(D.9)}$$

The left side of Equation D.1, $\int_s^t e^{-x^2} dx$, is evaluated by replacing e^{-x^2} by its Maclaurin series and carrying out term by term integration.

$$\int_s^t e^{-x^2} dx = \int_s^t \left(1 - \frac{x^2}{1!} + \frac{x^4}{2!} - \frac{x^6}{3!} + \ldots + (-1)^n \frac{x^{2n}}{n!} + \ldots\right) dx \quad \text{(D.10)}$$

$$= \left[C + x - \frac{x^3}{3.1!} + \frac{x^5}{5.2!} - \frac{x^7}{7.3!} + \ldots + (-1)^n \frac{x^{2n+1}}{(2n+1)n!} + \ldots\right]_s^t \quad \text{(D.11)}$$

$$= \left[t - \frac{t^3}{3.1!} + \frac{t^5}{5.2!} - \frac{t^7}{7.3!} + \ldots + (-1)^n \frac{t^{2n+1}}{(2n+1)n!} + \ldots\right]$$
$$- \left[s - \frac{s^3}{3.1!} + \frac{s^5}{5.2!} - \frac{s^7}{7.3!} + \ldots + (-1)^n \frac{s^{2n+1}}{(2n+1)n!} + \ldots\right] \quad \text{(D.12)}$$

Equation D.9 equals Equation D.12. Equation D.1 is proved.

Appendix E

Interpolation Coefficients

The interpolation coefficients α, β, γ, δ (Equations 3.4 – 3.5) are obtained by solving the system of Equations 3.8a – 3.8d :

$$u_A = \alpha + \beta x_A + \gamma y_A + \delta x_A y_A$$

$$u_B = \alpha + \beta x_B + \gamma y_B + \delta x_B y_B$$

$$u_C = \alpha + \beta x_C + \gamma y_C + \delta x_C y_C$$

$$u_D = \alpha + \beta x_D + \gamma y_D + \delta x_D y_D$$

From Figure 3.5,

$$x_A = x_C \tag{E.1}$$

$$y_A = y_B \tag{E.2}$$

$$x_B = x_D = (x_A + \Delta x) \quad \text{and} \tag{E.3}$$

$$y_C = y_D = (y_A + \Delta y) \tag{E.4}$$

$$\tag{E.5}$$

Substituting these values into the Equations 3.8a – 3.8d gives

$$u_A = \alpha + \beta x_A + \gamma y_A + \delta x_A y_A \tag{E.6}$$

$$u_B = \alpha + \beta(x_A + \Delta x) + \gamma y_A + \delta(x_A + \Delta x)y_A \tag{E.7}$$

$$u_C = \alpha + \beta x_A + \gamma(y_A + \Delta y) + \delta x_A(y_A + \Delta y) \tag{E.8}$$

$$u_D = \alpha + \beta(x_A + \Delta x) + \gamma(y_A + \Delta y) + \delta(x_A + \Delta x)(y_A + \Delta y) \tag{E.9}$$

The system of equations E.6 – E.9 was solved using the Mupad computer algebra

system. The solutions are:

$$\alpha = (u_A(x_A + \Delta x)(y_A + \Delta y) - u_B x_A(y_A + \Delta y) - u_C(x_A + \Delta x)y_A$$

$$+ u_D x_A y_A)/(\Delta x \Delta y) \tag{E.10}$$

$$\beta = (-u_A(y_A + \Delta y) + u_B(y_A + \Delta y) + u_C y_A - u_D y_A)/(\Delta x \Delta y) \tag{E.11}$$

$$\gamma = (-u_A(x_A + \Delta x) + u_B x_A + u_C(x_A + \Delta x) - u_D x_A)/(\Delta x \Delta y) \tag{E.12}$$

$$\delta = (u_A - u_B - u_C + u_D)/(\Delta x \Delta y). \tag{E.13}$$

Substituting $(x_A + \Delta x) = x_B$ and $(y_A + \Delta y) = x_C$ into Equations E.10 – E.12 gives the interpolation coefficients.

$$\alpha = \frac{u_A x_B y_C - u_B x_A y_C - u_C x_B y_A + u_D x_A y_A}{\Delta x \Delta y} \tag{E.14}$$

$$\beta = \frac{-u_A y_C + u_B y_C + u_C y_A - u_D y_A}{\Delta x \Delta y} \tag{E.15}$$

$$\gamma = \frac{-u_A x_B + u_B x_A + u_C x_B - u_D x_A}{\Delta x \Delta y} \tag{E.16}$$

$$\delta = \frac{u_A - u_B - u_C + u_D}{\Delta x \Delta y}. \tag{E.17}$$